Forschungszentrum Karlsruhe
in der Helmholtz-Gemeinschaft

Wissenschaftliche Berichte
FZKA 7100

Status of He-cooled Divertor Development (PPCS Subtask TW4-TRP-001-D2)

P. Norajitra (Editor)

T. Chehtov, A. Gervash, R. Giniyatulin, T. Ihli, R. Kruessmann, V. Kuznetsov, A.Makhankov, I. Mazul, P. Norajitra, I. Ovchinnikov, J. Weggen, B. Zeep

Institut für Materialforschung
Institut für Reaktorsicherheit
Programm Kernfusion

Februar 2005

Forschungszentrum Karlsruhe

in der Helmholtz-Gemeinschaft

Wissenschaftliche Berichte

FZKA 7100

Status of He-cooled divertor development
(PPCS Subtask TW4-TRP-001-D2)

Compiled and edited by
P. Norajitra

Contributors

T. Chehtov, A. Gervash[1], R. Giniyatulin[1], T. Ihli,
R. Kruessmann, V. Kuznetsov[1], A.Makhankov[1],
I. Mazul[1], P. Norajitra, I. Ovchinnikov[1],
J. Weggen, B. Zeep

Institut für Materialforschung
Institut für Reaktorsicherheit

Programm Kernfusion

[1]D. V. EFREMOV Institute, Scientific Technical Centre „Sintez“,
St. Petersburg

Forschungszentrum Karlsruhe GmbH, Karlsruhe

2005

Impressum der Print-Ausgabe:

Als Manuskript gedruckt

Forschungszentrum Karlsruhe GmbH
Postfach 3640, 76021 Karlsruhe

Mitglied der Hermann von Helmholtz-Gemeinschaft
Deutscher Forschungszentren (HGF)

ISSN 0947-8620

urn:nbn:de:0005-071008

Abstract

Within the framework of the EU power plant conceptual study (PPCS), helium-cooled modular divertor concepts have been investigated in detail at the Forschungszentrum Karlsruhe during the past few years. The first conceptual design proposed was based on convective cooling with the use of flow promoters in the form of pin and/or slot arrays (HEMP/HEMS) to increase the cooling surface and, hence, enhance the heat transfer capacity. While continuing the design optimisation, an advanced multiple-jet design (HEMJ) was introduced, which is based on direct jet-to-wall impinging cooling and offers advantages in terms of simple construction and manufacturing. Main emphasis of the 2004 work program (TW4-TRP-001) lay on experiments for the concepts HEMJ and HEMS, which were mainly performed at the Efremov Institute in St. Petersburg, Russia. For experiment preparation, detailed test programs were worked out and accompanying CFD analyses were accomplished. The outcomes of experimental investigations and status of design development shall be the subject of this report.

Status der Entwicklung von He-gekühlten Divertoren (PPCS Subtask TW4-TRP-001-D2)

Zusammenfassung

Im Rahmen der EU-Reaktorstudie (PPCS) wurden in den letzten Jahren am Forschungszentrum Karlsruhe heliumgekühlte modulare Divertorkonzepte im Detail untersucht. Das erste vorgeschlagene konzeptionelle Design HEMP/HEMS basierte auf einer Konvektivkühlung mit Hilfe einer Strömungs- bzw. Wärmeübertragungsverstärkung in Form von Pin- bzw. Slot-Reihen zur Vergrößerung der Kühlungsoberfläche und somit zur Erhöhung der Wärmeübertragungkapazität. Im Verlauf der Designoptimierung wurde das fortschrittliche Multi-Jet-Design (HEMJ) eingeführt, welches auf einer direkten Jet-to-Wall Prallkühlung basiert und Vorteile in der einfachen Konstruktion und Fertigung bietet. Schwerpunkte des Arbeitsprogramms 2004 (TW4-TRP-001) bilden die Experimente für die Konzepte HEMJ und HEMS, die hauptsächlich am Institut Efremov in St. Petersburg, Russland durchgeführt werden. Für die Experimentvorbereitung wurden umfangreiche Versuchsprogramme ausgearbeitet und begleitende CFD-Analysen durchgeführt. Gegenstand dieses Berichts sind die Ergebnisse der experimentellen Untersuchungen und der Status der Designentwicklung.

Table of contents

Abstract I

Zusammenfassung I

Table of contents II

1 Introduction *(P. Norajitra)* 1

2 Progress of the conceptual design *(T. Ihli)* 1

  2.1 Advanced design HEMJ 1

  2.2 HEMS design optimisation 4

  2.3 GPF experiment plan for HEMJ and HEMS 4

3 Mock-up manufacturing for thermohydraulic experiments 5

  3.1 Cu-alloy and brass mock-ups for GPF experiments *(R. Giniyatulin)* 5

  3.2 Steel mock-ups for HEBLO experiments *(R. Kruessmann, J. Weggen)* 6

  3.3 Tungsten material selection for the thimble of the real mock-up *(R. Giniyatulin, I. Mazul)* 7

4 Technological study of the manufacturing of W components 7

  4.1 Progress of the EDM development *(R. Giniyatulin)* 7

  4.2 Issues of ECM development *(R. Giniyatulin)* 9

  4.3 Status and progress of the process development for tungsten-MIM *(B. Zeep)* 10

  4.4 W/W brazing (tile/thimble) with curved shape *(A. Makhankov)* 11

  4.5 W/steel joining development *(I. Mazul, A. Gervash, T. Ihli)* 14

5 GPF2 experimental campaigns and results *(I. Ovchinnikov, V. Kuznetsov)* 16

6 Design-related analyses 18

  6.1 CFD analyses *(R. Kruessmann)* 18

  6.2 Stress analyses 19

    6.2.1 W/W joints (tile/thimble) *(T. Ihli)* 19

    6.2.2 W/steel joints (thimble/ODS structure) *(T. Chehtov)* 20

7 Conclusions and outlook *(P. Norajitra)* 22

Acknowledgement 22

Abbreviations 23

Symbols 24

Subscripts 24

References 25

List of tables 26

List of figures 26

1 Introduction

P. Norajitra

Within the framework of the power plant conceptual study (PPCS), He-cooled divertor concepts have been investigated intensively at the Forschungszentrum Karlsruhe. The first conceptual design 'HE-cooled modular divertor concept with integrated pin array and/or slot array' (HEMP/HEMS) [1-1, 1-2] was investigated in detail during the past years. In continuation of the PPCS work in 2004, an advanced modular divertor concept with multiple jet cooling (HEMJ) [1-3, 1-4] was introduced. The design variants HEMP/HEMS and HEMJ essentially differ in the heat transfer mechanism. The first variant (HEMP/HEMS) is based on convective cooling with the help of flow promoters in the form of pin and/or slot arrays which increase the cooling surface and, hence, enhance the heat transfer capacity, whilst the HEMJ design variant is based on direct jet-to-wall impinging cooling (i.e. abrupt change of momentum of the fluid) without flow promoter. This cooling technology offers the advantages of a relatively high potential performance and easier design with more easily producible parts. Having evaluated the first concept with respect to feasibility and simplicity of manufacturing, the HEMJ design proves to be suitable for the reference concept due to its relatively simple construction, followed by HEMS as a back-up solution. The emphasis of the 2004 work program (TW4-TRP-001) lies on the design optimisation, including analyses, preparation (i.e. design, layout, and fabrication of the mock-ups), and execution of the experiments, which shall be the subject of this report.

2 Progress of the conceptual design

T. Ihli

2.1 Advanced design HEMJ

Cooling and heat transfer mechanisms

Impingement cooling is an effective way to generate a high cooling rate in many engineering applications. In steel or glass industry impinging jets are used to cool down the products after rolling. In gas turbine engines impinging jets are applied to cool turbine blades or vanes. In laser or plasma cutting processes, application of jet impingement cooling can reduce the thermal deformation of products. Besides the above applications and as part of the current subtask, impinging jets have now been applied to enhance heat transfer in a He-cooled divertor for a nuclear fusion power plant.

The ability of controlling heat transfer from the surface by varying flow parameters, such as jet exit velocity and flow temperature, as well as geometrical parameters, such as jet exit opening, nozzle-to-surface spacing, and nozzle-to-nozzle spacing in arrays, is the key factor that has led to the sustained and widespread use of jet impingement technologies. The most commonly used geometries are axisymmetric (circular orifice or pipe) and slot (two-dimensional) nozzles.

The flow field of an impinging jet (Fig. 2-1) can be divided into three zones: (1) the free jet prior to impingement, (2) the impingement region, and (3) the wall jet region.

Using different low Reynolds number turbulence models, the distribution of the htc around the impingement region was analysed (Fig. 2-2). The maximum heat transfer coefficient occurs near the centre axis of the jet hole. The htc decays relatively strongly with increasing distance from the jet centre. At a small jet-to-jet distance, sidewise heat conductivity within the cooled wall is sufficient to yield an almost uniform wall temperature inside the cap, as was demonstrated by the results of CFD studies at FZK and the Efremov institute (see CFD chapter). To avoid non-uniform temperature distributions inside the cap, a large number of small jets are therefore preferred.

To cool hot spots, single jets are used. To cool larger surfaces, arrays of cooling jets are necessary. Around the several impingement regions, wall jet flows are produced, which interact. The coolant leaves the hot wall in fountains (Fig. 2-3) along the interaction lines between the jets. Fig. 2-4 shows a typical distribution of the htc inside the cap.

Florschuetz et al. [2-1–2-5] conducted an extensive study for different arrays of jets. These authors extracted heat transfer correlations from their measurements. These correlations are nowadays widely used in the industry design process.

A very simple correlation for arrays of cooling jets is given in the German heat transfer manual “VDI Wäremeatlas” (based on results of Schlünder and Gnielinski, Krötzsch et al. and Martin [2-6–2-10]).

Following these correlations, the heat transfer coefficent htc and the Nusselt Number Nu can be calculated for a triangular multiple jet arrangement:

$htc = \frac{Nu \cdot \lambda}{D}$, where λ is the heat conductivity of the coolant and D is the jet hole diameter.

$Nu = G \cdot \mathrm{Re}^{2/3} \cdot \mathrm{Pr}^{0.42}$, where Re is the jet Reynolds number and G is a geometry function:

$$G = \frac{d^* \cdot \left(1 - 2.2 \cdot d^*\right)}{1 + 0.2\left(h^* - 6\right) \cdot d^*} \cdot \left[1 + \left(\frac{10 \cdot h^* \cdot d^*}{6}\right)^6\right]^{-0.05};$$

$f = \frac{\pi}{2 \cdot \sqrt{3}} \cdot \frac{D_h^2}{L_T^2}$, $d^* = \sqrt{f}$, $h^* = \frac{H}{D}$ (see Fig. 2.3).

The jet Reynolds number can be calculated as follows:

$\mathrm{Re} = \frac{wD_h}{\nu}$, $\nu = \frac{\eta}{\rho}$; where v is the kinematic viscosity, η the dynamic viscosity, and ρ the density of the coolant. The mean jet velocity w can be calculated, when the jet mass flow is known.

$w = \frac{\dot{m}_j}{A_h}$; The jet mass flow is a function of the coolant parameter, discharge coefficient of the holes, and the pressure ratio between the total coolant plenum pressure (p_c) (no internal cross-flow in the plenum) and static pressure outside the holes p_m (cross-flow in the gap between cartridge and cap):

$$\dot{m}_j = C_D \cdot \dot{m}_{j\_ideal}; \qquad \dot{m}_{j\_ideal} = \frac{\pi \cdot D^2}{4} \cdot p_c^t \cdot \left(\frac{p_m}{p_c^t}\right)^{\frac{\kappa+1}{2\cdot\kappa}} \cdot \sqrt{\frac{2 \cdot \kappa}{(\kappa - 1) \cdot R \cdot T_c^t}\left(\left(\frac{p_c^t}{p_m}\right)^{\frac{\kappa-1}{\kappa}} - 1\right)};$$

The heat flux and inner temperature of the cap Tw can be determined iteratively:

$$T_w = T_{Th,\max} - \dot{q}_{Tile} \frac{A_{Tile}}{A_c} \cdot \frac{s_{Th}}{\lambda_{Th}}; \qquad \dot{q}_{Tile} = htc \cdot \frac{A_c}{A_{Tile}} \cdot \left(T_w - T_c\right)$$

where s_{Th} is the wall thickness of the cap (thimble) and λ_{Th} is the heat conductivity of the cap material. A_{Tile} is the surface area of the armour (tile) and A_c is the jet cooled inside of the cap. For a more detailed investigation, heat conductivity along the vertical section of the cap (to the steel body) and the convective heat transfer inside the vertical cap section have to be taken into account in addition to the jet impingement heat transfer.

To demonstrate the influence of the jet hole diameter in an example, all other parameters (dp, mass flow, and G) were kept constant, while D was varied. (Parameter dp = 0.14 MPa, sharp edges; mass flow = 6.8 g/s per cap; h* = 2; d* = 0.2). As shown in Fig. 2-5, the heat transfer coefficient increases drastically for jet hole diameters below 0.5 mm. Nevertheless, jet holes with a diameter of 0.6 mm and larger were used for the current study to reduce the potential danger of blockage.

Design and thermohydraulics features

The ring divertor is divided into cassettes, which allows for comfortable handling and maintenance. The main components of the divertor cassettes are the thermally highly loaded target plates, the dome with the opening for removing plasma impurities by vacuum pumps, and the main structure or bulk with the manifolds for the coolant.

The surfaces of the target plates have to be made of an armour material with a high melting point, high thermal conductivity, and a low sputtering rate. Tungsten seems to meet these requirements very well and is therefore used. For acceptable thermal stress levels in the armour layer and the cooling system below, the W-armour layer has to be castellated. Thermal stress calculations have indicated that the width of the cooling segments should be below 20 mm (see chapter on stress). For close packaging of the armour segments and the cap-like sub-structure below, hexagonal armour parts (tiles) are used in the vertical section of the target plate. In the curved section of the targets (baffle), square tiles are employed.

The tiles represent the thermal shield of the divertor, which is not cooled directly due to the risk of cracks in the brittle tungsten structure. The directly cooled structure below the tiles has to withstand a high internal loading of about 10 MPa and high temperature gradients leading to high stress levels without any defects occurring, e.g. cracks or creep fatigue. This structure (cap or thimble) is made of tungsten alloy W-1%La_2O_3 (WL10) which possesses a high plasticity up to a temperature of about 1300 °C. The tiles are connected to the caps by a brazing joint. The caps are of cylindrical shape (lateral) and domed at the top (Fig. 2-6). A cartridge with an array of impingement holes is inserted into the caps to implement multiple jet cooling inside the cap.

For the first basic layout of the vertical high-heat-flux section of the targets, an array of 24 impingement holes of 0.6 mm diameter each on top of the cartridge and a centre hole with a diameter of 1 mm is chosen (Fig. 2-7). The cap (or thimble) has an outer diameter of 15 mm (wall thickness of about 1 mm).

The supporting structures are made of the oxide dispersion-strengthened reduced-activation ferritic steel ODS-EUROFER. The design concept allows for an assembly in several steps with intermediate testing (Fig. 2-8) to increase the reliability of the divertor cassette and avoid waste during fabrication. First, the armour is brazed to the thimble. Then, the thimble and an intermediate steel piece are joined by brazing using cast copper and tungsten pins for mechanical interlock. In this way, brazing can be carried out before the parts are mounted to the extended divertor steel structure. The intermediate steel pieces with the thimbles and tiles are welded to the top part of a small multi-finger module (e.g. 9 fingers in one module)

(Fig. 2-9). Finally, the middle and bottom parts of the module casing are welded to the inside of the top part. This results in a pressure-resistant housing that can be tested before mounting it to stripe modules. The stripe modules are tested and mounted to the target plates which again are tested and mounted to the divertor cassette.

A well-distributed mass flow is obtained by the relatively high pressure drop in the jet cartridge and the low pressure drop in the module housing and support channels. The mass flow is controlled by drillings in the cartridge as the pressure drops dramatically in the holes. The drillings are made with low tolerances using laser machining. Hence, the jet holes may be considered valves that control the mass flow rate for each cooling finger.

Another important advantage of this design is its flexibility. It can be adapted to all kinds of gas-cooled reactors by adjusting the jet hole configuration and the numbers of parallel and series connections of the small multiple finger units.

2.2 HEMS design optimisation

In the report of the past year [1-1], a modular He-cooled divertor concept with integrated pin array and/or slot array (HEMP/HEMS) was proposed and described in detail. The principle of the HEMP concept is illustrated again in Fig. 2-12 together with a sketch of the cross-section of a cooling finger (left). It consists of armour, cap, cartridge, and pin array shown by the 3D CAD drawing on the right. The pin array itself is located on a flat plate which is brazed onto the cap. The cooling principle is convective heat transfer with enlarged cooling surface by means of the pin array which is made of tungsten or tungsten alloy.

To reduce the difficulties in fabrication of the W pin array, a similar concept HEMS with an alternative slot structure as flow promoter was analysed in 2003. It was found that the cooling performance of HEMS was at least as good as that of HEMP. In 2004, the HEMS concept was further optimised to increase its cooling performance and reduce its pressure losses. In Fig. 2-13, the principle of the HEMS design is shown by a CAD-generated isometric view. The helium coolant is directed through the inside of the steel cartridge and forced through an array of slots arranged on a base plate. The flow turn from the radial to the vertical direction is now reached in a rounded section of the slots. As an optimisation idea, a diffuser section was designed at the slot outlet, but its fabrication seems to be difficult, as obvious from mock-up fabrication by the EDM technique.

2.3 GPF experiment plan for HEMJ and HEMS

The HEMJ geometry shown in Fig. 2-7 was chosen as a reference option and named J1-a. To test the influence of different parameters of the cooling system, an experimental matrix was drawn up. Options J1-b and J1c have different jet-to-wall distances, all other parameters are the same compared to option J1-a. Options J1-d and J1-e have different hole diameters, all other parameters are the same compared to option J1-c. Options J1-f to J1-h have other hole diameters and numbers of holes than option J1c, but the same overall jet hole surface and the same jet-to-wall spacing. Option J2 has another cap diameter as the J1 options, but all other parameters are the same as for option J1c. For all J1 options (J1-a to J1-h), the cap geometry is unchanged, only the cartridge has to be changed for the experiments. The parameters of the HEMJ options described are shown in Table 2-1.

To test the optimised HEMS concept, three different geometry options were designed. The slot width for all options is 0.2 mm, the slot number is 32. The slot array plate is flat in the middle section and well-rounded in the edge region. S1-b and S1-c do not have any outlet diffuser; they differ in terms of slot height which was chosen to be 1.2 mm for the S1-b option and 1.7 mm for the S1-c option. Option S1-a is similar to option S1-b, but provided with an outlet diffuser with an opening angle of 20°, which was assumed to be a good compromise between feasibility and dynamic pressure regain. The parameters of the HEMS options described are shown in Table 2-2.

3 Mock-up manufacturing for thermohydraulic experiments

3.1 Cu-alloy and brass mock-ups for GPF experiments

R. Giniyatulin

To compare different cooling structures, the thimbles were manufactured from a material with a thermal conductivity (λ) near 150 W/mK. These materials have to have a stable λ in the temperature range of 500 - 700°C and reasonable strength. In this way, costs of manufacturing of the mock-ups are reduced in this stage of the work.

Cu-alloy mock-up for the "Efremov design" with 36 slots

The mock-up was produced from CuCrZr alloy with the following results:

- Roughness Ra~0.4 µm
- Measuring results:
    - Slot width (0.24 ± 0.005) mm
    - Slot height (1.82÷1.87 ± 0.005) mm

EDM duration ~ 40 hours (see also chapter 4.1).

HEMS mock-ups

In principle, mock-ups are manufactured from CuCrZr alloy with the following sequence of steps:

- Machining of the thimble with cone bottom
- EDM fabrication of the profiled electrodes
- EDM of the slots in the thimbles using profiled electrodes
- EDM of cylindrical slots by tubular electrodes

The electrodes were manufactured from pure copper by means of wire-cut EDM.

At present, it is considered to combine the tile, thimble, and slot array in one unit for the experiments at the GPF facility. The first prototype of such mock-up is presented in Fig. 3.1-1. The remaining mock-ups for the improved HEMS design with different parameter variants are being manufactured in accordance with Table 2-2. The measurements of the slots were performed using an optical microscope and knife-shaped probe. The measurement results show that the real slot width is larger than given in the design. The reason is the technique of electrode manufacturing. It is difficult to produce the required plate thickness of 0.1 mm taking into account a sparking gap of 0.05 mm.

To simplify the manufacturing process, electrode tungsten plates (from rolled foil) with a thickness of 0.2 mm were manufactured. These electrodes produce slots with a width of 0.3 mm that is suitable for e.g. the mock-up S1-c-0.3. This mock-up was manufactured from brass L-63 (Russian grade) which was selected as its thermal conductivity was closer to that of tungsten in comparison with CuCrZr in the temperature range of RT-600°C as applied for the GPF experiments (Table 3.1-1).

HEMJ mock-ups

HEMJ mock-ups for GPF experiments are prepared in the same way as HEMS mock-ups, i.e. the cup-element possesses the functions of tile and thimble combined. The cups are produced from copper alloy CuCrZr for a first test campaign and from brass L-63 for the second test campaign. The HEMJ cartridges were made of steel.

In the June campaign, conventional drilling was applied to produce the jet holes. Five cartridges were produced in accordance with the test plan listed in Table 2-1. The hole diameters of these cartridges were measured by means of an optical microscope. The relative error of the drilled holes was in the range of 3-6%.

For the second test campaign in November, shortened cartridges and spacers (Fig. 3.1-2**)** were manufactured with a very high accuracy of the hole diameters (less than ±1%) in a watch factory. The reduced height of cartridges allowed for a changing of the hole profile inside. One of the cartridges (J1-a) was designed with twice as large a wall thickness at the top in order to study the effect of the jet channel length. The diameter of the holes was measured with special calibrated rods. The tolerance of the drilled holes for these cartridges was in the range of 1-5 microns. To obtain a proper jet-to-wall spacing within the mock-up, special spacers were used. The assembly of cartridge, tube, and spacers is presented at the bottom of the figure.

3.2 Steel mock-ups for HEBLO experiments

R. Kruessmann, J. Weggen

The major goal of this year's research programme is to demonstrate the performance of the different concepts and, at the same time, their comparison. Data for this purpose are available from correlations, CFD simulations, and experiments. Only the comparison of all sources available will provide a general impression of the performance of the concepts.

To draw conclusions, a validation of the CFD programs is necessary in particular. Results from simulations and experiments will be compared, so that the numerical tools can be adjusted to give accurate results and to allow extrapolations. For this purpose, the Helium Blanket & Divertor Test Loop (HEBLO) (Fig. 3.2-1) will be used. FZK possesses this facility which was used for experiments related to blanket development. In 2004, it was modified to allow for divertor tests. Mock-ups represent one cooling finger in a 10:1 geometry. Heating of the mock-up is achieved by an electric heater, temperatures of up to 500 °C on the upper surface can be reached. The loop can be operated at a helium temperature of up to 450 °C, 80 bar, and a max. mass flow of about 120 g/s, a condition that does not quite match the divertor operating conditions. Nevertheless, the experimental results can be used for comparison with results simulated under the same boundary conditions and allow for an adjustment of the code. For this purpose, the mock-up is instrumented with a number of thermocouples and pressure sensors to measure the local distribution of flow parameters. Pressure is measured at 18 locations in the test section, temperature at 50 locations in the test section. Other instrumentation serves to control the loop. Fig. 3.2-2 shows the distribution of the measurement devices in the test section. All instruments were calibrated.

The test section (Fig. 3.2-3) is made of steel 15Mo3 and composed of a long inlet tube to ensure fully developed flow conditions. Mock-ups to be tested (e.g. HEMS, HEMJ) are mounted at its top and can be exchanged easily. An electrical heating plate is placed on top of the test section for a moderate heat flux simulation of up to 0.3 MW/m². In the case of HEMS, flow is directed from outside to the inside of the mock-up. For testing the HEMJ mock-ups, the flow direction will be reversed. The HEMS mock-up was turned from 300 mm rod material. The tile, thimble, and slot array of HEMS were combined in one unit and produced by EDM using copper electrodes. The process took 32 h. Tolerance was ± 0.1 mm. A roughness of Ra = 2.5 µm was obtained. All drillings for instrumentation were produced by a CNC machine. The pressure connection lines are of stainless steel and sealed with conical surfaces. The thermocouples are first brazed into a 2 mm diam. sleeve and then into a 2 mm diam. drilling to ensure a good heat conductivity. The inlet tube was turned from rod material with an accuracy of 0.1 mm. The mock-up was fixed to the inlet tube by EB welding. As these two parts carry the pressure, they were licensed by German authorities. The inner parts were also produced from 15Mo3 and partly welded using a laser. They are gas-tight, but also easily exchangeable. The inner tube has a roughness of Ra = 1.8 µm. The interior pipe with in-flow body is located inside the test insert and equipped with an axial compensator. The length of the compensator was selected such that the in-flow body is pressed onto the internal structure of the head (webs/slots) with a certain force and, in addition, the different thermal expansions of the pressure-carrying parts and installation components are compensated well.

The pins for the HEMP mock-up were produced by cutting from a rod and brazing into a plate. The quality of brazing was controlled by X-ray. Thermal properties of the brazing material are estimated to be lower than those of the mock-up material. This has to be taken into account when comparing the results with CFD calculations. First HEBLO experiments will presumably start in the beginning of 2005 for a HEMS mock-up with straight slots, followed by the HEMJ experiments. The design of the HEMJ mock-ups is under way.

3.3 Tungsten material selection for the thimble of the real mock-up

R. Giniyatulin, I. Mazul

For the fabrication of real mock-ups, four different tungsten grades are currently under consideration. Their features are listed in Table 3.3-1 in comparison with conventional PM pure tungsten. All four materials were taken for single finger manufacturing trials and consistent testing.

The following experience was gained:

- WL-10 and W-Cu showed satisfactory suitability for machining in comparison with conventional tungsten that requires additional measures (polishing and electrochemical etching to remove surface damages)
- Similar to conventional W, SC tungsten shows the tendency to cracking especially at the sharp corners during machining; additional means to obtain the required thimble shape are under investigation (see Fig. 3.3-1)

Further investigation may proceed in three directions:

- Collection/generation of a database (mainly thermomechanical properties)
- Neutron irradiation resistance studies
- Manufacturing and thermomechanical testing

4 Technological study of the manufacturing of W components

4.1 Progress of the EDM development

R. Giniyatulin

The W-thimble with a shaped cooling surface for helium-cooled mock-ups can be manufactured in two ways: fabrication of the W-thimble from a tungsten block (rod or plate) with a shaped surface inside; fabrication of the W-thimble and separately shaped plate with subsequent joining (brazing or diffusion bonding). In the present stage of the work, the first variant was used. Two design options of the W-thimble were considered for these manufacturing studies:

- FZK pin array design;
- Efremov slot design.

The FZK pin array design is presented in the Fig. 4.1-1.

The W-thimble was designed such that it could be installed in the experimental facility for measuring the pressure drop and heat transfer coefficient (see chapter on GPF experiments). It was decided to fabricate this mock-up from tungsten by means of electric discharge machining (EDM). The attempts of using EDM on tungsten samples made one year ago (under a previous contract) had been promising.

For mock-up fabrication, powdered tungsten of the grade WL10 was used. The semi-finished product was a cylinder of 22 mm in diameter.

The shaped electrodes were made of copper alloy (brass). Due to electrode burning during machining, five identical electrodes were fabricated, together with special tool for their exchange (pins and holder), Fig. 4.1-2. The holes were drilled in the design dimensions plus a gap for the “spark” (0.05 mm on each side). Hence, each diameter was increased by ~ 0.1 mm to obtain the design dimensions after EDM.

Brass was selected for the electrodes, as it could be machined best. Pure copper is better, but this plastic material is deformed during drilling. Use of pure copper is possible, if the diameter of the holes will be increased.

The EDM of the tungsten thimble with pins inside was performed in four steps:

- Shaping of the outer perimeter by grinding for 15 hours;
- EDM of the inner cylindrical body for 22 hours;
- EDM of pins using brass electrodes for 5 hours, 1 hour per electrode (all five electrodes were used);
- EDM of the inner surface by a copper cone-shaped electrode for 4 hours, 2 hours per electrode (two electrodes were used, Fig. 4.1-3).

Each electrode was used up to burn-out of the walls between the holes. This means that the electrode cannot be used any further. Due to the limited number of identical electrodes, the required geometry of the pins was not obtained. The view of the mock-up after the steps mentioned is presented in Figs. 4.1-4 and 4.1-5. The Efremov slot design is presented in Fig. 4.1-6. For this mock-up, a conventionally powder-sintered tungsten rod was used. The outer mock-up contour was designed such that it could be installed in the experimental facility.

For EDM of the slots, tungsten “plate-shaped” electrodes were used (Fig. 4.1-7). The electrodes were wire-cut from a solid block. Fabrication of the electrodes from copper failed, because they were deformed by cutting. The width of the slots is 0.2 mm. That is why the thickness of the electrode is 0.1 mm. First EDM tests were performed on the sample.

These tests showed that it is possible to use tungsten electrodes, but the wear of the electrode is very high (about 100%). Such tool wear is acceptable only for investigation purposes, when the geometry of the cooling surface has to be investigated.

Fabrication of the tungsten thimble (Fig. 4.1-8) was performed in the following sequence:

- Shaping of outer perimeter (grinding, 15 hours);
- EDM of inner cylindrical body for 20 hours;
- Fabrication of 40 W-electrodes – 40 hours, 1 hour per electrode;
- EDM of slots using W-electrodes for 72 hours, 2 hours per slot.

During installation in the experimental facility, the mock-up cracked (Fig. 4.1-9). It was decided to repair it using the casting technique. Pure copper was cast on outer thimble surface, but unfortunately molten copper penetrated the gaps and filled them up (Fig. 4.1-10). The copper of the gaps was subjected to chemical etching to repair the mock-up.

Summary

Further investigation in the direction of using EDM for tungsten surface profiling requires an optimisation of the geometry for different structures. For the “pin geometry”, decrease in the pin diameter could give positive results. For the “slot geometry”, increase in the slot width could simplify the EDM process. The other way consists in optimising the EDM parameters together with the selection of proper electrode materials.

From our point of view, EDM could be used only for “cooling structure” examination, selection, comparison, etc., when the costs and duration of the processes are not so important. For mass production or fabrication of large-scale mock-ups, this technique is too time-consuming and expensive, and alternative approaches are necessary, such as electrochemical machining (ECM) or/and laser machining.

4.2 Issues of ECM development

R. Giniyatulin

The cooling surface with different structures (pins, slots, etc.) can be produced by different technological methods depending on the materials used. Electrochemical machining (ECM) is one of the attractive approaches. ECM is a well-known technique in industry, but use depends on the type of materials and is mostly limited to steels and its alloys.

ECM has the following advantages:

- Absolute absence of tool wear.
- Absence of burrs on the machined surface.
- Technological output parameters practically do not depend on the toughness and strength of the processed materials.
- Compared to electric erosion machining, there is no thermal impact on the machined surface layer structure.
- Complete absence of mechanical contact between the tool and the object enables machining of non-rigid and open-worked pieces with high productivity.
- Possibility of decreasing roughness of the surface machined with a simultaneous increase in productivity. No existing mechanical and electrochemical method of machining has such advantage. The output of machining with the required surface roughness Ra < 0.4 μm by ECM is 10-100 times greater than that of electric erosion machining with good quality parameters.
- Compared to mechanical methods of machining (milling, grinding), electrode tools are made of easy-to-process metals and may have a stability and strength substantially lower than the machined material.

Machining is carried out at low (below 12 V) voltage, employing electrolytes (aqueous solutions of neutral mineral salts of small concentration). This increases electric safety of the operators and excludes the possibility of fire in the machining zone.

At the moment, Russian industry has no experience in the ECM of tungsten and its alloys. Specialists from the Scientific Research Institute for Problem Theories and Technologies of Electrochemical Machining (Ufa, Russia) checked tungsten samples for their suitability for machining by ECM on request. First simplified tests demonstrated that ECM of tungsten is feasible in principle (Fig. 4.2-1). Machining of slots or pin structures on tungsten samples remains to be investigated. The related R&D will show the technological possibilities, roughness, tolerance, etc. for the geometry required.

4.3 Status and progress of the process development for tungsten-MIM

B. Zeep

The goal of the project is the development of the microMIM process as a mass production method for producing microstructured heat transfer promoters made of tungsten or tungsten alloys. To establish the manufacturing process, feedstock development, the injection moulding process itself as well as debinding and sintering have to be taken into consideration. For developing a suitable feedstock, blending experiments of commercial tungsten powders and different binders in combination with additives, such as e.g. stearic acid or beeswax, were carried out using a kneader and an extruder. In the beginning, an unusually long mixing time (3 hours) and high speed (60 RPM) resulting in a very high torque and thermal as well as mechanical degradation of the binder had to be used for compounding a feedstock in the kneader. In feedstock development, the first step is the choice of a suitable powder. An ideal powder for feedstock production should be spherical and not agglomerated. Unfortunately, tungsten powders are always strongly agglomerated due to the production method.

For this reason, major efforts were undertaken in purchasing tungsten powders with an average grain size of about 1 µm from different suppliers all over the world in order to find a compoundable powder quality. The powder samples were tested with respect to their grain size distribution, BET, agglomeration state, grain properties and resulting compoundability. Furthermore, efforts were taken to find and optimise a suitable binder system for compounding an injection-mouldable feedstock. Following an evaluation of powder and binder combinations, the recipe of a feedstock could be developed, which is compoundable within one hour, as a result of which thermal stress of the binder is reduced.

Feedstocks with solid loads of 40 vol.%, 42 vol.%, 45 vol.%, 47 vol.%, and 50 vol.%, respectively, were produced and tested in injection moulding experiments using a round shaped test cavity with a diameter of 10 mm and a thickness of 1 mm. The feedstocks of up to 45 vol.% solid load could be moulded without any difficulties in terms of cavity filling or processing in the injection unit. First parameter changes had to be made at a solid load of 47 vol.%, whereas in the case of feedstocks with 50 vol.% solid load, an automatic process could no longer be established.

On the basis of these results, the next step in the near future will be the execution of injection moulding experiments of tensile test bars for testing the feedstock with a more difficult-to-fill cavity on the one hand and for producing samples for mechanical properties tests on the other hand. Moreover, first injection moulding tests on a “slot array” cavity will be performed using a feedstock with a solid load of 47 vol.%.

As 47 vol.% solid load might be a problem as regards the design accuracy of the final sintered component, an approach to increasing the maximum solid content has to be developed. A de-agglomeration step might be a good alternative to improve the compounding properties of the processed powders.

De-agglomeration experiments were performed using different kinds of milling methods. A rolling PE bottle equipped with tungsten bars, a cryo-mill, a horizontal ball mill, a rotation mill, and a jet mill were tested. In the course of these experiments, the jet mill was found to be most suitable, as it showed a clear shift of the grain size distribution to lower grain sizes without any changes of the BET surface.

However, the shear forces needed for compounding the feedstock after de-agglomeration increased drastically. A reason might be the relatively high amount of particles between 200 nm and 50 nm after de-agglomeration. To solve this problem, classification experiments are presently being prepared. They will be carried out at the University of Freiberg, Germany.

Another option is to use powders with a bigger grain size. Corresponding experiments are currently being carried out using a powder with a grain size of about 3 µm. A problem associated with the bigger grain size will be the sintering activity. As bigger grain sizes cause the sintering activity to decrease, problems with respect to the final density and mechanical stability of the sintered components might occur.

Up to now, a relatively high final density above 90% and a quite low final carbon content of less than 0.003 mass% could be achieved by applying a two-step debinding procedure, followed by a final sintering step at temperatures of 2100°C which is far below the melting point (3420°C). Traditionally, 75% (~2565°C) of the melting temperature should be used for sintering polycrystalline samples. The relatively high final density of the sintered samples is only possible due to the small particle size of the processed powder.

To provide for a higher final density, sintering equipment other than the induction-heated oven used up to now will be tested. In this context, microwave sintering has already been tried without any success. Future sintering experiments will be performed using an electric field oven and HIP.

4.4 W/W brazing (tile/thimble) with curved shape

A. Makhankov

Brazing alloys tested for the production of the W/W joint

The filler metal tested for the production of the W/W joint is listed in Table 4.4-1.

The best HHF test results in previous tests were reached by the joint produced with 71KHCP and STEMET 1311 filler metal. Hence, present efforts are aimed at further developing the joint produced with these brazing alloys. Besides these two brazing alloys, STEMET 9 was used as an alloy specially developed for the W/W joint.

In the absence of the He cooling loop, it was proposed to develop the W/W joint by HHF testing of water-cooled mock-ups of the geometry shown in Fig. 4.4-1.

Modelling of temperature fields in the mock-up (Fig. 4.4-2, Fig. 4.4-3) shows that the temperature at the bonding line is close to 1200°C, i.e. the value anticipated for the DEMO W/W joint.

Mock-up parts prepared for mock-up manufacturing are shown in Fig. 4.4-4.

Three filling metals are considered for the W/W joint:
- 71KHCP (Co-base, 5.8Fe, 12.4Ni, 6.7Si, 3.8B, 0.1Mn, P≤0.015, S≤0.015, C≤0.08), T_{br}=1100°C
- STEMET 1311 (Ni-base, 16.0Co, 5.0Fe, 4.0Si, 4.0B, 0.4Cr), T_{br}=1050°C
- STEMET 9 (Ni-base, 4Mo, 4Fe,15Cr, 7.5Si, 1.5B)

The first two alloys produced the best results during previous tests: mock-ups brazed with 71KHCP survived up to 22 MW/m^2; mock-ups brazed with STEMET 1311 survived up to 16.5 MW/m^2. The last alloy was specially developed for the W/W joint.

For these tests, several mock-ups were manufactured: one brazed with 71KHCP filler metal, three brazed with STEMET 1311, and the last brazed with STEMET 9 filler metal.

Mock-up brazed with 71KHCP filler metal

Mock-up manufacturing

The temperature in the mock-up during brazing versus time is shown in Fig. 4.4-5. The mock-up before testing is shown in Fig. 4.4-6.

Mock-up testing

This mock-up was subjected to a screening test:

10 MW/m^2	100 cycles	OK
12 MW/m^2	100 cycles	OK
14 MW/m^2	100 cycles	OK
16 MW/m^2	10 cycles	Failed

The surface temperature of the mock-up during the test is shown in Fig. 4.4-7. It can be seen that surface temperature during the test is close to the calculated temperature (compare Fig. 4.4-3 and Fig. 4.4-7).

The mock-up after the failure is presented in Fig. 4.4-8. It can be seen that failure occurred in the W/W joint.

Mock-up brazed with STEMET 9 filler metal

Mock-up manufacturing

The temperature in the mock-up during brazing versus time is shown in Fig. 4.4-9. The mock-up before testing is shown in Fig. 4.4-10.

Mock-up testing

This mock-up was subjected to a screening test:

10 MW/m^2	100 cycles	OK
12 MW/m^2	100 cycles	OK
14 MW/m^2	100 cycles	OK
15 MW/m^2	1 cycle	Failed (overheated surface due to joint failure)

The surface temperature of the mock-up during the test is shown in Fig. 4.4-11. It can be seen that surface temperature during the test is close to the calculated temperature (compare Fig. 4.4-3 and Fig. 4.4-11).

The mock-up after the failure is presented in Fig. 4.4-12. It can be seen that failure occurred in the W/W joint and due to this, the tile surface was molten.

Mock-up No. 1 brazed with STEMET 1311 filler metal

Mock-up manufacturing

The temperature in the mock-up during brazing versus time is shown in Fig. 4.4-13. The mock-up before testing is shown in Fig. 4.4-14.

Mock-up testing

This mock-up was subjected to a screening test:

10 MW/m^2	100 cycles	OK
12 MW/m^2	100 cycles	OK
14 MW/m^2	100 cycles	OK

15 MW/m^2	100 cycles	OK
16 MW/m^2	100 cycles	OK
17 MW/m^2	29 cycles	Failed (overheated surface)

The surface temperature of the mock-up during the test is shown in Fig. 4.4-15. It can be seen that surface temperature during the test is close to the calculated temperature (compare Fig. 4.4-3 and Fig. 4.4-15).

The mock-up after the failure is presented in Fig. 4.4-16. It can be seen that cracks in tungsten have developed, but the joint survived. The cracks are caused by rather large tile dimensions.

Mock-up No. 2 brazed with STEMET 1311 filler metal

Mock-up manufacturing

The temperature in the mock-up during brazing versus time is shown in Fig. 4.4-17. In order to increase re-melting temperature, the joint was kept at a temperature of 1000°C for 1 hour to activate diffusive processes. The mock-up before testing is shown in Fig. 4.4-18.

Mock-up testing

This mock-up was subjected to a screening test:

13 MW/m^2	100 cycles	OK
14 MW/m^2	100 cycles	OK
15 MW/m^2	378 cycles	Failed (overheated surface)

The surface temperature of the mock-up during the test is shown in Fig. 4.4-19. It can be seen that surface temperature during the test is close to the calculated temperature (compare Fig. 4.4-3 and Fig. 4.4-19).

The mock-up after the failure is presented in Fig. 4.4-20. It can be seen that cracks in tungsten have developed, but the joint survived. These cracks are caused by rather large tile dimensions.

Mock-up No. 3 brazed with STEMET 1311 filler metal

The third mock-up brazed with 1311 filler metal is provided with a castellated upper tile of 10x10x4 mm^3. The mock-up is shown in Fig. 4.4-21. The brazing conditions were the same as for mock-up No. 2.

Mock-up testing

This mock-up was subjected to a screening test:

15 MW/m^2	700 cycles	OK
15 MW/m^2	50 cycles	Failed (overheated surface)

The mock-up after the failure is presented in Fig. 4.4-22. It can be seen that cracks in tungsten have developed, but the joint survived.

The screening tests of the mock-ups with W/W joints have shown that the joints produced with STEMET 1311 filler metal are sufficiently reliable at a temperature in the joint of about 1200°C up to a heat flux of 15 MW/m^2. However, optimisation of tile geometry is required in order to meet the requirements of the DEMO divertor.

Brazing of a real-geometry tile to the thimble

In this first attempt, STEMET 1311 was used in the form of strips of 5 mm width and 40 μm thickness. The strip was cut into pieces of about 30 mm length and placed into the gap between joined parts in the form of a star (see Fig. 4.4-23). The brazing gap between the joined parts was about 40 μm. Spacers were not used. The jig shown at the bottom of the figure was used for brazing. Some pressure was applied during brazing.

The temperature in the mock-up during brazing is shown in Fig. 4.4-24. The cross-section of the joint is shown in Fig. 4.4-25. It can be seen that areas without a joint exist in the curved parts. This may be due to lacking brazing alloy or unsatisfactory accuracy of manufacturing. A breakthrough was achieved by the second attempt in November under improved conditions. Fig. 4.4-26 shows the mock-up used for HHF testing with a curved bonding line after the successful brazing attempt. The calculated temperature fields in the mock-up are illustrated in Fig. 4.4-27.

HHF thermal cycling tests yielded the following results:

13 MW/m^2	100 cycles	OK
14 MW/m^2	100 cycles	OK
15 MW/m^2	70 cycles	*failure in joint and W (overheated surface, Fig. 4.4-28*)

Brazing of the W-slot array to a W-thimble

To check possibility of brazing for joining the slot array with the thimble, both slot array and thimble were designed and manufactured from tungsten. In this development stage, it was decided to produce these parts in accordance with the drawings shown in Fig. 4.4-29 and the brazing scheme presented in the right lower corner. Brazing is planned to be performed in the following sequence:

- Filling the slots with a mixture of ceramic powder and glue (to prevent the brazing alloy from penetrating into the slots);
- Brazing;
- Removing of filling mixture;
- Wire cutting and metallographic investigation.

This work is under way.

4.5 W/steel joining development *(I. Mazul, A. Gervash, T. Ihli)*

I. Mazul, A. Gervash, T. Ihli

Introduction

The large mismatch in thermal expansion coefficients of W alloys as thimble material and the ODS Eurofer steel structure, which are about 4-6x10^{-6} [1/K] and 10-14x10^{-6} [1/K], respectively, will locally cause very high plastic strains at edges and corners in the transition zone under temperature cyclic loadings. To avoid thermocyclic plastification at the joints, a design of transition pieces is shown in Fig. 6.2.1-1 and Fig. 6.2.1-2**,** applying Cu casting in the gap between W and steel and an additional mechanical interlock like small W pins in this example.

Technical investigation of Cu casting with various options of interlock applied to different thimble materials (WL10, SCW, W-15Cu) is going on at Efremov. The possibility of applying CVD tungsten material for the production of the W-steel joint was also studied. First results of thermocyclic tests (RT-600°C) and the leak test for transition joints under the impact of internal He pressure (10 MPa) have already been obtained.

Outcomes before spring 2004

- Diffusion bonding and e-beam welding were excluded after failures of the mock-ups following isothermal (up to 650°C) thermal cycling
- Brazing using a Co-brazing alloy (alloy 71KHCP, Mo thimble without lock) was tested successfully (several thermal cycles of 200-700-200°C at inner He pressure of 15 MPa)

- several mock-ups with a Cu interlayer were manufactured and tested (isothermal heating up to 600-700°C and cooling to 200°C under internal He pressure of 15 MPa):
  - Mo thimble without lock (failed after 1 thermal cycle)
  - W (conventional) thimble without lock (failed after 1 thermal cycle)
  - Mo thimble with thread (successfully survived 15 thermal cycles of 200-650-200°C at an inner He pressure of 15 MPa
- Conclusion:
  - Cu casting was selected as a basic joining technology
  - the steel tube is located externally relative to the thimble
  - strengthening lock is required
  - lanthanated W is required for thimble machining

Outcomes in spring 2004

- Three mock-ups with a strengthening lock were manufactured from WL10
- 2 mock-ups with bayonet-type locks failed in different stages of manufacturing before testing
- the third mock-up with a pin-type lock (see Fig. 4.5-1) failed (W cracking) after the first thermal cycling
- Conclusion:
  - more accurate W machining is strongly required
  - the lock configuration has to be simplified

***Latest results** (October-November 2004)*

- This campaign was aimed at finding a reliable (reference) joining option in order to guarantee the execution of the mock-up testing programme in 2005
- in addition to joint thermocycling tests, comparative thermomechanical and tightness tests of candidate W grades for the thimble were carried out (non-isothermal heating). The special test procedure allowed for a thermal gradient in the range of 600°C (for joint) – 1000°C (for thimble top) (see Fig. 4.5-2)
- one mock-up made of WL10 and equipped with a pin-type lock was thermocycled. After the second thermal cycle, a leak was detected in the area of the pin lock
- several mock-ups with a new conic lock (Figs. 4.5-3, 4.5-4) and different thimble materials (WL10, W-Cu, SC-W, TZM) were manufactured and tested
- the first mock-up with a conic lock and WL10 thimble failed after the first thermocycle due to a number of defects (arc-induced surface microcracking (Fig. 4.5-5), extremely high (~2000°C calculated) thermal gradient)
- second mockup successfully survived 10 thermocycles (p_{in}=10 MPa)
- the mock-up with the W-Cu thimble (Fig. 4.5-6) also successfully survived 5 thermocycles (600-900°C), then a He leak was detected in the thimble top (no cracks)
- testing of the mock-up with a SC-W thimble is under preparation
- the mock-up with the CVD-W thimble is being manufactured at the moment (Fig. 4.5-7)
- Conclusion: for the time being, a W-steel joining technology has been found for performing the 2005-2006 R&D programme of thermohydraulic and thermomechanical design testing/optimisation.

5 GPF2 experimental campaigns and results

I. Ovchinnikov, V. Kuznetsov

Prior to the He loop experiments with HHF tests, first thermohydraulics tests are carried out in a gas puffing facility (GPF). These tests are based on a reversed heat flux method, i.e. hot helium (inlet/outlet temp. of 700/600 °C) is pumped through the built-in CuCrZr divertor mock-ups to estimate their thermohydraulic efficiency (pressure loss and HTC) when cooled by a 100 °C water coolant at the top of the thimble. The layout of the facility and the experiments were accompanied by simulation calculations. The major goal of these tests is to prove the performance of the concepts investigated and to validate the results obtained with commercial CFD codes.

Pre-test phase with 'empty' mockups (January – March)

The GPF2, as a modification of GPF1, now consists of a closed helium loop and a longer helium pulse length (10 s at least) compared to GPF1 (within the range of ms). The GPF2 mock-up assembly is shown in Fig. 5.1-1. The heat power used amounts to about 80 kW. The water cooling unit on top of the mock-up was modified significantly by a flat water flow (typical velocity ~50 m/s) instead of a radial water flow. This allows for an easy adjusting of the water film thickness, and a rather homogeneous heat transfer coefficient (HTC) of at least 200 kW/m^{2}K is achieved as predicted by CFD simulation calculations. Double thermocouples are used in the area with high temperature gradients, since mixing of heated and cold water still is problematic and additional space is required. In GPF2, a 40-litre pressurised balloon fed by compressed air is used instead of a water pump. This technique provides for a higher flexibility with a stable heat transfer and larger pressure drop. 11 channels are provided in the data acquisition system for the registration of the inlet/outlet temperatures of He and water, water mass flow rate, as well as the mock-up inlet pressure and pressure drop. In the absence of mock-ups, GPF2 started work with so-called "empty" experiments. Here, CuCrZr billets for the slot-type mock-ups were used instead of the mock-ups. 2 experiments with different billets were carried out (referred to as "empty4" and "empty5").

The first so-called 'empty experiments' were carried out using simplified and/or dummy mock-ups, i.e. in the absence of real mock-ups: among them are two 'empty' experiments with CuCrZr billets for the slot option, two experiments with a CuCrZr pin array mock-up fabricated by EDM, and one "Ers36" experiment with Efremov's slot mock-up fabricated by EDM. All mock-ups were tested under a 'reversed' heat flux of up to 20 MW/m^2 and qualitatively fulfilled their functions as expected.

The results of these experiments revealed a rather serious problem concerning the accuracy (tolerance) of mock-up manufacturing, since the uncertainty of the cross-section geometry for helium flow has a strong influence on both the HTC and pressure drop, as was confirmed by the respective CFD simulations.

First testing campaign with fabricated mock-ups from CuCrZr (April – October)

The helium compressor of membrane type delivered by FZK was repaired and re-assembled for helium recirculation in the following experimental campaigns. A He mass flow rate of ~ 5 g/s without inlet pressure overloading could be reached. Longer helium pulses through the mock-ups were achieved by increasing the number of balloon feeders and receivers to 6 and 8, respectively. Thus, the influence of transient regimes on the experimental results was reduced. The following additional improvements were implemented: instant helium relative mass flow meter (orifice pressure drop type) for better normalising the feeder and receiver signals, extension of data acquisition system to 16 channels to cover additional needs (He flow meter, balloon receiver diagnostics, etc.), fine filter for the water sub-system.

The following experiments were carried out for the following variants: a) 4 HEMJ options (Tab. 2-1), 2x J1-a, 2x J1-b, 4x J1-d, and 3x J1-e; b) 2 HEMS options (Tab. 2-2), 3x S1-b, 2x S1-c. The mock-ups for this campaign are produced from CuCrZr (see chapter 3.1).

The measuring results show low scattering and an acceptable accuracy for the pressure drop of all mock-ups, but a significant scattering of power removal, which requires further improvement.

Second testing campaign with fabricated mock-ups (starting November)

Further improvements have been made: among them are a fine filter for the He sub-system, a new control device ensuring an increased stabilisation of the inlet He pressure versus mass flow rate, extension of the data acquisition system to 22 channels, a new electromechanically driven main helium flow controller that allows for MFR scanning within the required range of 5-15 g/s and helps avoiding the transient regimes.

Mock-ups for this campaign were mostly produced from brass with thermal conductivity values close to those of tungsten (see chapter 3.1). The mock-up cap thickness was reduced to 2 mm. Inserts were used to reduce the unwanted blind heat flux from the mock-up through its flange.

Pressure losses measured in the second GPF2 testing campaign under improved experimental conditions are shown in Fig. 5.2 as a function of the helium mass flow rate for the HEMJ variants J1-a and J1-e (Table 2-1) with varying jet hole diameters (mm) / jet-to-wall distances (mm) of 0.6/1.2 and 0.85/0.9, respectively, and the HEMS option S1-c24 with 24 slots of 0.3 mm width. The latter is a modification of the nominal S1-c version with 32 slots and 0.2 mm width (Table 2-2). It was found that at a nominal mass flow rate of 6.8 g/s, the pressure loss for HEMJ lies between approx. 0.1 MPa for J1-a and 0.045 MPa for J1-e. The respective value for the HEMS S1-c24 amounts to about 0.15 MPa.

The divertor performances determined by the GPF2 heat transfer measurements for the same design variants are illustrated in Fig. 5-3. For nominal design with a 6.8 g/s mass flow rate, the maximum performance reached for HEMJ was about 12.5 MW/m^2 for J1-a and 10.5 MW/m^2 for J-1e, respectively. For the HEMS design S1-c24, a value of about 11 MW/m^2 could be obtained.

Conclusions

The GPF2 facility started work in the end of 2003 and showed a promising behaviour. The GPF2 parameters were achieved by means of CFD pre-simulations as part of the experiment campaign. The capability of heating the helium gas in long pulses is sufficient and lies significantly above the values required. First GPF results revealed problems of mixing the inlet and outlet flow, thus leading to an inaccurate measurement of the inlet and outlet temperatures and, hence, to a complicated check of the heat balance of the mock-up. The problem of measuring the helium mass flow rate was solved, now a sufficient measuring accuracy is reached. Sealing of the mock-up surface by copper rings is not reliable. Therefore, brazed and welded joints may be required. First CFD simulation calculations by Ansys Flotran for the real experiments revealed too pessimistic predictions compared to the experimental results. Nevertheless, they could serve as a basis for code validation.

In spite of some existing problems, the DEMO divertor mock-ups can now be examined with a wide range of inlet parameters in GPF2 prior to the start of the helium loop operation at “TSEFEY”.

6 Design-related analyses

6.1 CFD analyses

R. Kruessmann

Thermohydraulic investigations

During this year, thermohydraulic investigations were undertaken to assess the different design options properly. Investigations in particular focused on a study to optimise the new HEMJ design. To learn more about its performance, the mass flow, inlet pressure, and inlet temperature of the coolant were varied.

Results of this programme shall be presented below. They were obtained with the commercial fluid dynamics (CFD) program FLUENT. A second goal was the validation of the programs in use. Therefore, simulations were also undertaken with ANSYS FLOTRAN, COSMOS, and with STAR-CD by our co-workers. These results will be compared with each other.

Comparison of different CFD programs

Tab. 6.1-1 shows a comparison of the different CFD programs used. Additionally, some detailed information on the programs is given. Only results for the reference case (J1a, see Tab. 2-1, heat load 10 MW/m², mass flow 6.8 g/s) are included.

Generally speaking, the results are quite close to each other. This gives us the confidence that the numerical results are in the right range. A more detailed comparison of the different CFD programs is being prepared.

Parameter study for different flow and heat load conditions [1-4]

The above-mentioned reference geometry was used to perform a parameter study. Mass flow, heat load, and inlet pressure were varied to predict the heat transfer coefficient, pressure loss, and the maximum temperature of the thimble. Heat load values of 8, 10, 12, and 15 MW/m² were chosen. The mass flow varied between 5.3 and 15.5 g/s, the inlet pressure for 6.8 g/s was varied between 10 and 14 MPa.

A variation of the inlet pressure hardly has any effect on the htc and pressure loss.

Fig. 6.1-1 a-b shows contour plots of temperature and total pressure in the geometry. Fig. 6.1-2 presents the htc and pressure loss over mass flow for different heat loads.

Fig. 6.1-2 also includes the results obtained by analytical correlations (see chapter 2.1) for the pressure loss. They correspond rather well with the numerical results for all cases investigated, in particular for lower mass flow ranges.

As expected, the htc shows a linear dependence on the mass flow, while the pressure loss exhibits a parabolic one. Both are independent of heat load.

The maximum temperature of the thimble is one of the hardest design criterions (see chapter about materials [1-1]). Fig. 6.1-3 shows the values of max. temperature calculated by Fluent. With the nominal mass flow rate of 6.8 g/s, the maximum thimble temperature could even be kept below the temperature limit for the W thimble of 1300°C under a heat flux of up to 12 MW/m^2. A smaller mass flow rate of 5.3 g/s would also fulfil this boundary condition at 10 MW/m^2 with a lower pressure loss, if the operation temperature window of the steel structure material could be enhanced. Geometries adapted to a higher heat flux of up to 15 MW/m^2 are under investigation.

Other parameters, e.g. design-related parameters, such as the gap width between cartridge and thimble and the diameter of the jet holes, were also addressed. Results of the latter are still under discussion and will not be presented here in detail. Generally, they show a strong dependence of the pressure loss on the hole diameter, but not on the gap width. The variant with the biggest holes also shows the lowest pressure loss and the lowest cooling performance (the highest thimble temperature). On the other hand, the htc depends on both parameters. There seems to be an ideal gap width.

It is difficult to draw a conclusion in this stage of the investigations. Results obtained with different CFD programs generally are in satisfactory agreement. A more detailed validation of the programs will only be possible when results from the HEBLO tests will be available.

6.2 Stress analyses

6.2.1 W/W joints (tile/thimble)

T. Ihli

Small rounded caps are favourable to reduce the stress levels within the cap and armour under high heat flux conditions. Further improvements were achieved by some changes in the armour and cap design. The hexagonal armour section is reduced to flat part at the top of the finger. Between this hexagonal plate and the domed thimble, a cylindrical intermediate section is used to smooth the circumferential stress levels and to avoid stress peaks in armour and cap. This intermediate section could be produced as one piece with the hexagonal plate or it could be a separate part which is bonded to the hexagonal plate by means of the HIP process. The intermediate section and cap are connected by means of a brazing joint, where the embrittlement of the brazing zone under irradiation has to be as low as possible. Nevertheless, all components should survive an ideal bonding between intermediate section and cap. Therefore, bonding between all parts was used as a boundary condition of the current stress analyses. The thermal boundary conditions of stress analysis were taken from CFD results for the heat transfer coefficient at the He-cooled surfaces. Some further details of the optimised finger are the rounding of the intermediate section in the direction to the vertical cap section and the slight groove in the cap, which ends at the same location where the rounded part of the intermediate section ends, too. The wall thickness of the cap was reduced from 1.03 mm to 0.8 mm.

The principles of the optimised HEMJ finger were also adapted to the current slot option S1c.

Yield strength at 886°C:	495 MPa;
3Sm at 886°C:	564 MPa;

Max. stress values at 886°C:	HEMJ:	390 MPa
	HEMS:	496 MPa

Safety factors:

Related to yield strength:	HEMJ:	1.27
	HEMS:	1.00
Related to 3Sm:	HEMJ:	1.45
	HEMS:	1.14

The stress-related safety margin for HEMJ apparently is larger due to slot stiffening and less rounding of the cap inside. The HEMS S1c geometry shows a slightly lower max. cap temperature (1142°C) (without heat flux through a bonded cartridge) than the tested HEMJ option (1175°C). The Re number of the slot flow is about 6x10^3 which is below the critical limit of 10^4, but due to the inflow effect, the flow seems to be fully turbulent in the present case, anyhow.

As a possible conclusion, it could be pointed out that two different cooling concepts exist, which are both within the allowed stress limits, if plastic effects are taken into account (3Sm rule).

6.2.2 W/steel joints (thimble/ODS structure)

T. Chehtov

Introduction

In the project scope of development of the He-cooled divertor, it is proposed to characterise a joint of refractory materials (tungsten-based alloys) and oxide dispersion-strengthened ferritic steels (EUROFER). The joint is located in the upper part of the divertor body, the so-called 'transition zone' (Fig. 6.2.2-1). One possible joining technique is brazing at 1120-1150°C with amorphous foils or brazing pastes. In order to investigate the material behaviour under thermal and mechanical loading, a set of finite element (FE) computations has been made.

The calculations were performed using an optimised geometry concept, including a cylindrical tube brazed to a cylindrical solid block as a modular approach to achieving better cooling rates. Axial symmetry relative to the y-direction allows for a discretisation to a 2D model, as shown in Fig. 6.2.2-2. The stress distribution in the joint due to the combined load can help determine the weakest points in the geometry and serve as an input of further CAD optimisation.

Previous calculations of the model were based on a linear-elastic behaviour of the materials without considering the influence of the temperature. The regions with the highest stress intensity were identified, and it was shown that pure mechanical loading does not lead to plastic deformation [1-1].

The model was improved by taking into account the brazing process with heating to the brazing temperature of 1120°C and cooling to room temperature, followed by heating to a work temperature of 700°C in order to determine the residual stresses. A detailed elastic-plastic FE analysis was used to plot the actual stress distribution for the desired geometry and to study the role of the mismatch of the thermal expansion coefficients of the materials.

Material properties and boundary conditions

The model consists of a 1 mm thick tube made of W-1%La_2O_3 (WL10) joined to a body of EUROFER steel. Compared to pure tungsten, WL10 has a higher thermal expansion coefficient and therefore allows better joining to steel.

The 2D model shows an axially symmetric view of the two tubes bonded with brazing material. The bottom nodes are fixed in y-direction and an inner hydrostatic pressure of $P=10$ *MPa* is applied in radial direction as a distributed load to all nodes of the inner side of the tubes. This inner pressure induces an equivalent stress of $\sigma=28$ *MPa* in the wall of the upper part of the structure, which can be assumed to be a hemisphere. The relatively small size of the actual structure allows to apply a uniform temperature distribution throughout the joint region. The displacement and rotation effects were considered using the small displacement theory.

Assumptions

In order to investigate the role of the changing temperature, a full thermoplastic analysis was performed in several temperature steps. For both tungsten and steel alloys, a user-defined plasticity law was implemented. As an initial stress-free condition, a uniform nodal brazing temperature field of 1120°C was applied.

The analysis is divided into several steps. The first two steps include the residual stresses in the materials – the brazing process to a temperature of 1120°C and cooling to room temperature (RT) of 20°C. Since the joint interface consists of materials with different thermal and mechanical properties, such as their coefficients of thermal expansion, the residual stresses were calculated in this step. A plot of the stress distribution field is depicted in Fig. 6.2.2-3. Furthermore, the heating process to the work temperature (WT) of 700°C was divided into seven sub-steps to sustainably trace the change in the stress distribution with increasing temperature.

Results

The following figures show a comparison of the stress distributions of both elastic and combined elastic-plastic analysis. The stress distribution along the A-B and C-D curves gives an overview of the regions with the highest stresses and shows a non-uniform stress distribution. Selected sets of stress plots – the von Mises stresses, the x-, y-, and z-component stresses, and the principal stresses – are depicted in Figs. 6.2.2-4 to Fig. 6.2.2-11. Each curve tallies a different temperature level. Load case one (L1) corresponds to temperature one (brazing stress-free condition at 1120°C). L2 characterises the process of cooling to room temperature. In this step, maximum initial stresses are encountered that decrease with the temperature increasing to work temperature (L9). Steps L3 to L8 give the stress values at equal intervals of 100°C by heating the specimen to working temperature.

As it can be seen from the curves below, the average stresses are lower when considering the plastic behavior of the components. Hence, investigation of the lifetime under cyclic loading is required. However, the joint behavior after 11 cycles of combined thermal and mechanical loading was simulated. The results are not sufficient to give evidence of material failure caused by ratcheting and this is why they have to be considered preliminary.

Summary and outlook

Brazing as a possible technique of joining W-alloy (W-1%La_2O_3) to Eurofer was observed and evaluated with respect to a divertor application under cyclic operation between RT and 700°C. Therefore, a set of finite-element computations has been performed in order to collect sufficient knowledge about the failure behaviour of the joints at different temperature levels. The FE analysis may be extended by simulating the material behaviour under cyclic thermal loading after a number of cycles in a certain temperature range in order to determine the role of ratcheting. However, an FE analysis with more loading cycles is needed and a criterion for material failure of the joint should be formulated.

Furthermore, mechanical characterisation experiments, including tensile, shear, and isothermal fatigue, in the temperature range of RT-650°C should be carried out to verify the calculated data. Such experiments with brazed W-alloy (W-1%La_2O_3) / Eurofer – joints are being planned at the moment, and in the next stage thermal cycling between 350 and 650°C shall be accomplished. This will verify the calculation data and provide a deeper understanding of the failure modes observed.

7 Conclusions and outlook

P. Norajitra

Results and progress of work on the design-related issues, comprising design improvement, analyses, fabrication, and experiments are reported. Different conceptual designs of a He-cooled divertor with different heat transfer mechanisms are described. The advanced HEMJ has been chosen as reference design due to its easy construction and manufacturing, followed by the HEMS as backup solution. CFD calculations confirmed the predicted performance of both HEMJ and HEMS by correlations in terms of maximum acceptable temperatures and total pressure losses under a heat flux of 10 MW/m^2, which satisfied the requirements. Stress analyses based on the ASME code for the W parts also confirmed the integrity of the structures under the specified heat flux. First technological and thermohydraulic experiments were performed at Efremov with the main emphasis lying on the (W/W, W/steel) joining technology and thermohydraulics tests by means of a gas puffing facility (GPF) with reversed heat flux to estimate thermohydraulic efficiency (pressure loss and HTC). W/W high-temperature brazing was demonstrated successfully. When using STEMET as a filler material, mock-ups survived heat fluxes of up to 16 MW/m^2. Investigation on W/steel joining is going on, the tightness of the joint still remains to be demonstrated. The first GPF experiments with CuCrZr mock-ups of different designs confirmed the tendency of validity of the design and simulation.

Concerning the divertor material, the development of a suitable W alloy as structural material today is the main feasibility issue. Development of the manufacturing technologies for tungsten divertor components will be continued. Experimental studies are planned to further verify the results. At EFREMOV, a helium loop is presently under construction for high-heat-flux integral tests of divertor mock-ups and determination of the pressure loss and HTC of the cooling unit for the HEMJ and HEMS design variants. The loop is scheduled to be in operation and yield first test results in 2005. An electron beam facility is available there, which allows for the simulation of a high heat load of 10 MW/m^2 at least.

Acknowledgement

This work has been performed within the framework of the Nuclear Fusion Programme of Forschungszentrum Karlsruhe and is supported by the European Union within the European Fusion Technology Programme. The contents of the publication lie in the sole responsibility of the publishers and do not necessarily represent the views of the Commission or its services.

The authors are grateful to L. Boccaccini, S. Gordeev, V. Heinzel, N. Holstein, G. Janeschitz, P. Karditsas, W. Krauss, R. Lindau, A. Möslang, V. Piotter, M. Rieth and R. Ruprecht for their valuable discussions.

Abbreviations

B	Boron
BET	Brunauer-Emmett-Teller
C	Carbon
CFD	Computational fluid dynamics
Co	Cobalt
Cr	Chromium
CNC	Computerised numerical control
CTE	Coefficient of thermal expansion
CVD	Chemical vapour deposition
Cu	Copper
DEMO	Demonstration reactor
EB	Electron beam
ECM	Electrochemical machining
EDM	Electrical discharge machining
EFDA	European Fusion Development Agreement
EU	European Union
EUROFER	Reduced-activation ferritic steel
Fe	Iron
FE	Finite element
FZK	Forschungszentrum Karlsruhe
GPF	Gas puffing facility
He	Helium
HEMJ	Helium-cooled divertor concept with multiple jet cooling
HEMP	Helium-cooled modular divertor concept with integrated pin array
HEMS	Helium-cooled modular divertor concept with integrated slot array
HHF	High heat flux
Htc, HTC	Heat transfer coefficient
IR	Infrared
IRTV	Infrared television
La	Lanthanum
MFR, mfr	Mass flow rate
MIM	Metal injection molding
Mn	Manganese
Mo	Molybdenum
Nb	Niobium
Ni	Nickel
Nu	Nusselt number
O, O_2, O_3	Oxide
ODS	Oxide dispersion-strengthened
P	Phosphorus
PE	Polyethylene
PIM	Powder injection moulding
PM	Powder metallurgy
PPCS	Power plant conceptual study
Pr	Prandtl number
Re	Reynolds number
RT	Room temperature
RPM	Revolutions per minute
S	Sulphur
SC	Single crystal
Si	Silicon
Sm [MPa]	Strength
Ti	Titanium

TZM	Molybdenum alloy with 0.5% Ti, 0.08% Zr, and 0.04% C
UKAEA	United Kingdom Atomic Energy Authority
V	Vanadium
wt	Weight
W	Tungsten
WT	Work temperature
WL10	Tungsten lanthanum oxide
Y	Yttrium
Zr	Zirconium

Symbols

H [m]	Jet-to-wall distance
L_T, L_t [m]	Pitch between two jet holes
D [m]	Jet hole diameter
D_h [m]	Hydraulic diameter
$\dot{m}$ [kg/s]	Mass flow rate
p [MPa]	Pressure
Δp [MPa]	Differential pressure, pressure loss
R	Gas constant
Ra [µm]	Roughness
S_m [Mpa]	Strength
s [m]	Thickness
T [K]	Temperature
w [m/s]	Velocity
η [kg/ms]	Dynamic viscosity
κ [-]	Adiabatic index
λ [W/mk]	Thermal conductivity
v [m^2/s]	Kinematic viscosity
ρ [kg/m^3]	Density

Subscripts

br	brazing
c	coolant
h	hole
i, in	inlet
j	jet
m	mean
t	total
Th	thimble
w	wall

References

[1-1] R. Kruessmann, P. Norajitra, L. V. Boccaccini, T. Chehtov, R. Giniyatulin, S. Gordeev, T. Ihli, G. Janeschitz, A. O. Komarov, W. Krauss, V. Kuznetsov, R. Lindau, I. Ovchinnikov, V. Piotter, M. Rieth, R. Ruprecht, Conceptual design of a He-cooled divertor with integrated flow and heat transfer promoters (PPCS Subtask TW3-TRP-001-D2), Part I (Summary) and Part II (Detailed Version), FZKA 6974 & 6975, 2004.

[1-2] P. Norajitra, L.V. Boccaccini, E. Diegele, V. Filatov, S. Gordeev, V. Heinzel, G. Janeschitz, J. Konys, W. Krauss, R. Kruessmann, S. Malang, I. Mazul, G. Reimann, M. Rieth, G. Rizzi, R. Ruprecht, V. Slobodtchouk, "State of the art: Development of a helium-cooled divertor for DEMO", SOFE conference, San Diego, USA, October 2003.

[1-3] T. Ihli, P. Norajitra, G. Janeschitz, R. Kruessmann, R. Ruprecht, "Development of an advanced helium-jet-cooled divertor concept: cooling method and design", Jahrestagung der Kerntechnischen Gesellschaft Deutschland, Düsseldorf, 25th – 27th May 2004, Berlin: INFORUM GmbH, 2004 S. 385-388.

[1-4] T. Ihli, R. Kruessmann, I. Ovchinnikov, P. Norajitra, V. Kuznetsov, R. Giniyatulin, "An advanced He-cooled divertor concept", 23rd SOFT, Venice, Italy, 20.–24.9.2004.

[2-1] L.W. Florschuetz, C.R. Truman, D.E. Metzger, Streamwise flow and heat transfer distributions for jet array impingement with crossflow, Journal of Heat Transfer 103 (1981) 337–342.

[2-2] L.W. Florschuetz, R.A. Berry, D.E. Metzger, Periodic streamwise variations of heat transfer coefficients for inline and staggered arrays of circular jets with crossflow of spent air, Journal of Heat Transfer 102 (1980) 132–137.

[2-3] L.W. Florschuetz, Y. Isoda, Flow distribution and discharge coefficient effects for jet array impingement with initial crossflow, Journal of Engineering for Power 105 (1983) 296–304.

[2-4] L.W. Florschuetz, D.E. Metzger, C.C. Su, Heat transfer characteristics for jet array impingement with initial crossflow, Journal of Heat Transfer 106 (1984) 34–41.

[2-5] D.E. Metzger, L.W. Florschuetz, D.I. Takeuchi, R.D. Behee, R.A. Berry, Heat transfer characteristics for inline and staggered arrays of circular jets with crossflow of spent air, Journal of Heat Transfer 101 (1979) 526–531.

[2-6] Martin, H.: Advances in Heat Transfer, Vol. 13, S. 1/60. New York, San Francisco, London: Academic Press (1977).

[2-7] Schlünder, E.-U., u. V. Gnielinski: Chem.-Ing.-Techn. 39 (1967), pp. 578/84.

[2-8] Schlünder, E.-U., P. Krötzsch, u. F. W. Hennecke: Chem.-Ing.-Techn. 42 (1970), pp. 333/38.

[2-9] Krötzsch, P.: Chem.-Ing.-Techn. 40 (1968), pp. 339/44.

[2-10] Martin, H.: Stoffübergangsversuche und strömungstechnische Berechnungen zur Ermittlung einer optimalen Schlitzdüsenanordnung für Prallstrahltrockner. Diss. Univ. Karlsruhe 1973.

[6.1-1] Panos J Karditsas, Performance Analysis of the HETS and HEMJ He-cooled divertor concepts, PPCS/TW4-TRP-001, December 2004, unpublished.

List of tables

Table 2-1 HEMJ geometries for the 2004 GPF experiments.
Table 2-2 HEMS geometries for the 2004 GPF experiments.
Table 3.1-1 Thermal conductivity of the materials used for the mock-ups.
Table 3.2-1 Technical data of HEBLO.
Table 3.3-1 Different tungsten grades as a basis for thimble material selection.
Table 4.4-1 Filler metals tested for the production of the W/W joint.
Table 6.1-1 Comparison of the results obtained by different CFD programs.

List of figures

Fig. 2-1 Zones of an impingement jet.
Fig. 2-2 htc versus distance from jet axis for different low Re number turbulence models (as obtained from Chapter 6.1).
Fig. 2-3 Multiple impingement jet and geometrical parameter model.
Fig. 2-4 htc distribution of the multiple impingement jet (result obtained from Ch. 6.1).
Fig. 2-5 htc versus jet hole diameter D, (mass flow, G and pressure ratio constant).
Fig. 2-6 Principle of a jet impingement cooling finger for the gas-cooled divertor.
Fig. 2-7 Exemplary layout of a jet impingement cooling finger for the gas-cooled divertor.
Fig. 2-8 FZK design of a gas-cooled divertor cassette with a large number of cooling fingers.
Fig. 2-9 Multiple cooling finger housing, steel-tungsten joints.
Fig. 2.10 Cross section of the multiple cooling finger housing (left 2D, right 3D CAD).
Fig. 2.11 Dimensions of the multiple cooling finger housing.
Fig. 2-12 Principle of the pin array cooling finger for the gas-cooled divertor.
Fig. 2-13 Principle of a slot array cooling finger for the gas-cooled divertor.

Fig. 3.1-1 EDM of HEMS mock-ups from CuCrZr for GPF experiments.
Fig. 3.1-2 HEMJ cartridges and spacers for the second GPF test campaign.

Fig. 3.2-1 Helium blanket/divertor test loop (HEBLO).
Fig. 3.2-2 HEBLO mock-up instrumentation.
Fig. 3.2-3 HEBLO test section for various mock-ups.

Fig. 3.3-1 SC (left) and lanthanated (right) tungsten after machining.

Fig. 4.1-1 The thimble with the pin array structure inside.
Fig. 4.1-2 Electrodes for the EDM of the FZK pin array design.
Fig. 4.1-3 Cone-shaped electrodes after machining.
Fig. 4.1-4 Tungsten thimble with pin array structure, fabricated by EDM.
Fig. 4.1-5 The view of the electrodes after EDM.
Fig. 4.1-6 Drawing of the thimble with slots.
Fig. 4.1-7 EDM tests on tungsten using W electrodes (a – tungsten sample after EDM, b – W electrode after EDM).
Fig. 4.1-8 Tungsten thimble with slots (Efremov design) (a – thimble view, b – slots at the bottom).
Fig. 4.1-9 Cracks in the tungsten thimble.
Fig. 4.1-10 Tungsten gaps (a-filled by copper, b- after etching).

Fig. 4.2-1 W sample with 1-mm pin prepared by ECM at Ufa, Russia.

Fig. 4.4-1 Geometry of the mock-up used for the development of the W/W joint.
Fig. 4.4-2 Modelling of temperature fields in the mock-up at a heat flux of 15 MW/m^2.
Fig. 4.4-3 Temperature field in the mock-up as a function of the absorbed heat flux.
Fig. 4.4-4 Mock-up parts for the development of the W/W joint (water-cooled heat sink from TZM and W tiles from sintered rolled tungsten).
Fig. 4.4-5 Temperature in the mock-up during brazing with 71KHCP filler metal.
Fig. 4.4-6 Mock-up brazed with 71KHCP filler metal.
Fig. 4.4-7 Surface temperature of the mock-up at a heat flux of 14 MW/m^2.
Fig. 4.4-8 Mock-up after the test.
Fig. 4.4-9 Temperature in the mock-up during brazing with STEMET 9 filler metal.
Fig. 4.4-10 Mock-up brazed with STEMET 9 filler metal.
Fig. 4.4-11 Surface temperature of the mock-up at a heat flux of 14 MW/m^2.
Fig. 4.4-12 Mock-up after the test.
Fig. 4.4-13 Temperature in the mock-up during brazing with STEMET 1311 filler metal.
Fig. 4.4-14 Mock-up brazed with STEMET 1311 filler metal.
Fig. 4.4-15 Surface temperature of the mock-up at a heat flux of 16 MW/m^2.
Fig. 4.4-16 Mock-up after the test.
Fig. 4.4-17 Temperature in the mock-up during brazing with STEMET 1311 filler metal.
Fig. 4.4-18 Mock-up brazed with STEMET 1311 filler metal.
Fig. 4.4-19 Surface temperature of the mock-up at a heat flux of 15 MW/m^2.
Fig. 4.4-20 Mock-up after the test.
Fig. 4.4-21 Mock-up with castellation brazed with STEMET 1311 filler metal.
Fig. 4.4-22 Mock-up after the test.
Fig. 4.4-23 Brazing of the W real-geometry tile to the thimble.
Fig. 4.4-24 Temperature in the mock-up during brazing with STEMET 1311 filler metal.
Fig. 4.4-25 Cross-section of the W/W joint with real geometry.
Fig. 4.4-26 Mock-up for HHF testing with curved bonding line after a successful brazing attempt.
Fig. 4.4-27 FE analysis of temperature fields in the mock up with a curved bonding line.
Fig. 4.4-28 HHF testing of the mock-up with the curved bonding line.
Fig. 4.4-29 Brazing of the W slot array to the W thimble.

Fig. 4.5-1 W-steel joint with pin-type locking.
Fig. 4.5-2 Thermocycling experiment on a finger.
Fig. 4.5-3 Main elements for the W-steel joint with a new (conic) lock.
Fig. 4.5-4 Finger mock-up (without armour tile) after casting (left) and after post-testing examination (right).
Fig. 4.5-5 Cracking of the WL-10 thimble after thermocycling.
Fig. 4.5-6 Mock-up with a W-Cu thimble.
Fig. 4.5-7 Mock-up with CVD tungsten (Cu-steel structure before W-coating deposition).

Fig. 5-1 GPF2 mock-up assembly.
Fig. 5-2 Pressure losses measured in GPF2 for different HEMJ and one slot design variants.
Fig. 5-3 Divertor performance derived from GPF2 measurements for different HEMJ and one slot design variants.

Fig. 6.1-1 Temperature distribution and total pressure distribution in geometry J1a. Results obtained with FLUENT.
Fig. 6.1-2 htc and pressure loss versus mass flow for geometry J1a. Results obtained with FLUENT.
Fig. 6.1-3 Max. temperature of the thimble for different mass flows and heat loads. Results obtained with FLUENT.

Fig. 6.2.1-1 Parts and sections of the thermal stress-reduced cooling finger (HEMJ).
Fig. 6.2.1-2 Stress-reduced cooling finger (HEMJ).
Fig. 6.2.1-3 Temperature distribution of HEMJ, J1a, 6.8 g/s, 10 MW/m^2.
Fig. 6.2.1-4 Temperature distribution of HEMS, S1c, 6.8 g/s, 10 MW/m^2.
Fig. 6.2.1-5 Stress distribution of HEMJ, J1a, 6.8 g/s, 10 MW/m^2.
Fig. 6.2.1-6 Stress distribution of HEMS, S1c, 6.8 g/s, 10 MW/m^2.

Fig. 6.2.2-1 Transition zone.
Fig. 6.2.2-2 Model discretisation.
Fig. 6.2.2-3 Von Mises stress distribution.
Fig. 6.2.2-4 Von Mises stresses [MPa] along AB: a) consideration of the elastic materials behaviour only, b) externally defined elastic-plastic material.
Fig. 6.2.2-5 Principal σII stresses [MPa] along CD: a) consideration of the elastic materials behaviour only, b) externally defined elastic-plastic material.
Fig. 6.2.2-6 X-component stresses [MPa] along AB: a) consideration of the elastic materials behaviour only, b) externally defined elastic-plastic material.
Fig. 6.2.2-7 Y-component stresses [MPa] along AB: a) consideration of the elastic materials behaviour only, b) externally defined elastic-plastic material.
Fig. 6.2.2-8 Z-component stresses [MPa] along AB: a) consideration of the elastic materials behaviour only, b) externally defined elastic-plastic material.
Fig. 6.2.2-9 X-component stresses [MPa] along CD: a) consideration of the elastic materials behaviour only, b) externally defined elastic-plastic material.
Fig. 6.2.2-10 Y-component stresses [MPa] along CD: a) consideration of the elastic materials behaviour only, b) externally defined elastic-plastic material.
Fig. 6.2.2-11 Z-component stresses [MPa] along CD: a) consideration of the elastic materials behaviour only, b) externally defined elastic-plastic material.

Tab. 2-1: HEMJ geometries for the 2004 GPF experiments.

	Concept	
Option	HEMJ	Topic
J1-a	D=0.6 mm, d=15 mm, h=1.2 mm, 24 +1 holes*	Reference
J1-b	D=0.6 mm, d=15 mm, h=0.6 mm, 24 + 1 holes*	Jet-to-wall influence
J1-c	D=0.6 mm, d=15 mm, h=0.9 mm, 24 + 1 holes*	Jet-to-wall influence
J1-d	D=0.7 mm, d=15 mm, h=0.9 mm, 24 + 1 holes*	D influence (Lt = const)
J1-e	D=0.85 mm, d=15 mm, h=0.9 mm, 24 + 1 holes*	D influence (Lt = const)
J1-f	D=0.794 mm, d=15 mm, h=0.9 mm, 18 + 1 holes**	Lt influence (A = const)
J1-g	D=0.939 mm, d=15 mm, h=0.9 mm, 12 +1 holes***	Lt influence (A = const)
J1-h	D=1.212 mm, d=15 mm, h=0.9 mm, 6 +1 holes****	Lt influence (A = const)
J2	D=0.7 mm, ***d=20 mm***, h=0.9 mm, 42 + 1 holes*****	d influence (Lt = const (1d))

A = sum of hole cross-section
Lt = jet-to-jet spacing
h = jet-to-wall spacing
d = outer diameter of thimble
D = diameter of jet holes

* 24 holes with diameter D, 1 hole with diameter = 1.732 x D
** 18 holes with diameter D, 1 hole with diameter = 1.732 x D
*** 12 holes with diameter D, 1 hole with diameter = 1.732 x D
**** 6 holes with diameter D, 1 hole with diameter = 1.732 x D
***** 42 holes with diameter D, 1 hole with diameter = 1.732 x D

Tab. 2-2: HEMS geometries for the 2004 GPF experiments.

	Concept	
Option	HEMS	Topic
S1-a	Flat slot, s = 0.2 mm, n = 32, h = 1.2 mm, d=15 mm, Outlet Diffuser 20°	Outlet diffuser
S1-b	Flat slot, s = 0.2 mm, n = 32, h = 1.2 mm, d=15 mm, No Outlet Diffuser	Reference 1.
S1-c	Flat slot, s = 0.2 mm, n = 32, h = 1.7 mm, d=15 mm, No Outlet Diffuser	h influence

s = slot width
h = slot height
n = number of slots
d = outer diameter of thimble

Table 3.1-1: Thermal conductivity of the materials used for the mock-ups.

Type of material	Thermal conductivity, W/mK			
	200	300	600	800
W	140	126	120	110
L-63 (brass)	100	130	150	180
CuCrZr (bronze)	360-370			

Tab. 3.2-1: Technical data of HEBLO.

Main Circuit:	
Operation pressure	80 bar
Helium flow rate (max.)	330 g/s
Helium temp. (max.)	250 °C
Cooling capacity	115 kW
Compressor	
Pressure head	1.5 bar
Rate of delivery	100 m³/h
Temperature Cycle	
Operation pressure	80 bar
Helium flow rate	120 g/s
Helium temp. (max.)	450 °C
Heating power, new ceramic heater for mock-ups	About 10 kW

Table 3.3-1: Different tungsten grades as a basis for thimble material selection.

Grade	Advantages	Drawbacks
WL-10 (W-1La_2O_3)	Easy machining (lower DBTT), higher recrystallisation temperature;	No data on radiation resistance, doping additives (La, O) are not plasma-compatible;
W-Cu (W-15Cu)	Easy machining (lowest DBTT), less CTE ($8.1*10^{-6}$ estim.) mismatch with steel, highest thermal conductivity (223 est.);	Limited database, no data on radiation resistance, less resistance to accidents (lower melting temperature), higher activation;
SC W-1Ta (doped single crystal)	Lower DBTT, higher thermal conductivity (high purity);	Lower strength at elevated temperature, limited data-base, no data on radiation resistance, difficult to machine, expensive;
CVD W	Higher thermal conductivity (high purity), easy shaping and joining (TBD);	Limited database, no data on radiation resistance, expensive;

Table 4.4-1: Filler metals tested for the production of the W/W joint.

Grade	Composition element, wt%	Filler metal form	T_{braz}, °C
10HCP	Fe-base, 9.5Ni, 5.3Si, 3.2B, Mn≤0.1, P≤0.015, S≤0.015, C≤0.05	Foil of 30 μm	1100
71KHCP	Co-base, 5.8Fe, 12.4Ni, 6.7Si, 3.8B, 0.1Mn, P≤0.015, S≤0.015, C≤0.08	Foil of 40 μm	1100
STEMET 1306	Ni-base, 27.4V, 27.5Nb, 4.9Ti	Powder	1300
STEMET 1307	Ni-base, 8.6Si, 5.1Nb, 0.2Y	Foil of 30 μm	1200
STEMET 1201	Ti-base, 12.4Ni, 23.5Cu, 12.1Zr	Foil of 40 μm	1000
STEMET 1311	Ni-base, 16.0Co, 5.0Fe, 4.0Si, 4.0B, 0.4Cr	Foil of 40 μm	1050
STEMET 9	Ni-base, 4.0Mo, 4.0Fe, 15.0Cr, 7.5Si, 1.5B	Foil of 30 μm	1150

Tab. 6.1-1: Comparison of the results obtained by different CFD programs.

Test case: HEMJ1a with the following boundary conditions: heat load 10 MW/m², pressure inlet 10 MPa, mass flow inlet 6.8 g/s, temperature inlet 630 °C.

	Star-CD	Star-CD	Ansys Flotran	Fluent	Cosmos
	Gordeev, FZK	Gordeev, FZK	Ovchinnikov, EFREMOV	Kruessmann, FZK	Karditsas, UKAEA
Turbulence model	SST HRM	RNG HRM	RNG	RNG	
Max. temp. tile, °C	1722	1750		1675	1650
Max. temp. thimble °C	1191	1223	1176	1152	1060
Htc, W/m²K	20000 – 40000	20000 – 35000		Up to 57600, mean 31594.9	Mean 34000
Total pressure drop, MPa	0.196	0.193	0.17	0.14	0.05 – 0.06 (only static pressure)

Star-CD:
HRM = High Reynolds number model
Total cell number: 100,000, fluid properties: ideal gas, compressible, conductivity and viscosity are functions of the temperature, heat capacity constant; solid properties: conductivity and capacity depend on the temperature, density is constant; properties as published in [1-1]

FLUENT:
Total cell number about 1,800,000, fluid and solid properties: as published in [1-1], except for a constant fluid density of 4.7 kg/m³.

Cosmos:
More information will be included in the report by Panos Karditsas [6.1-1].

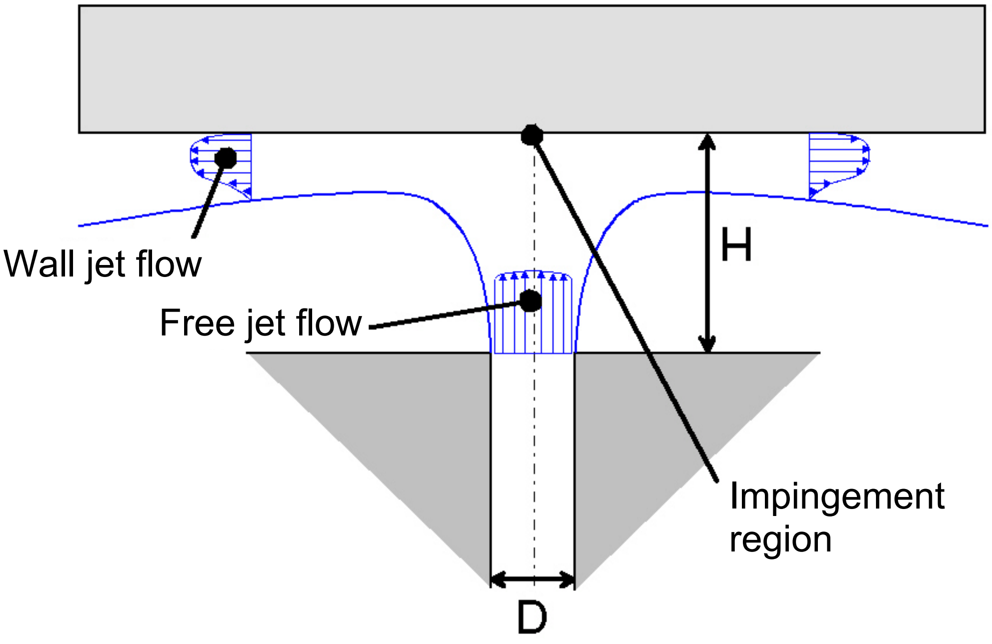

Fig. 2-1: Zones of an impingement jet.

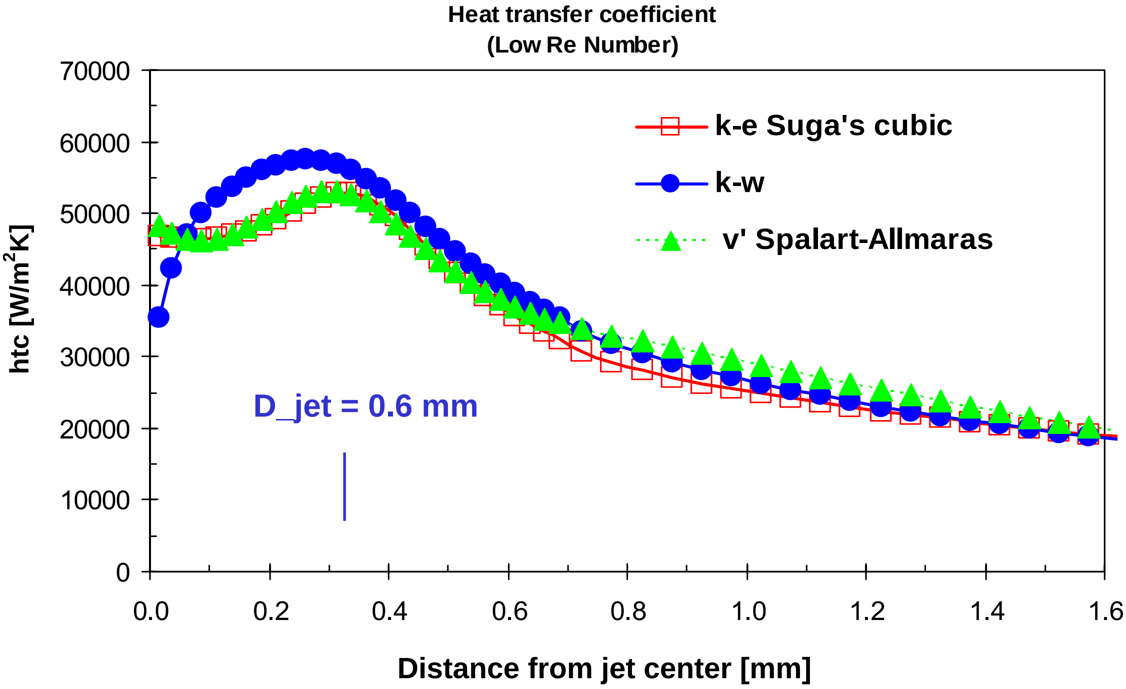

Fig. 2-2: htc versus distance from jet axis for different low Re number turbulence models (as obtained from Chapter 6.1).

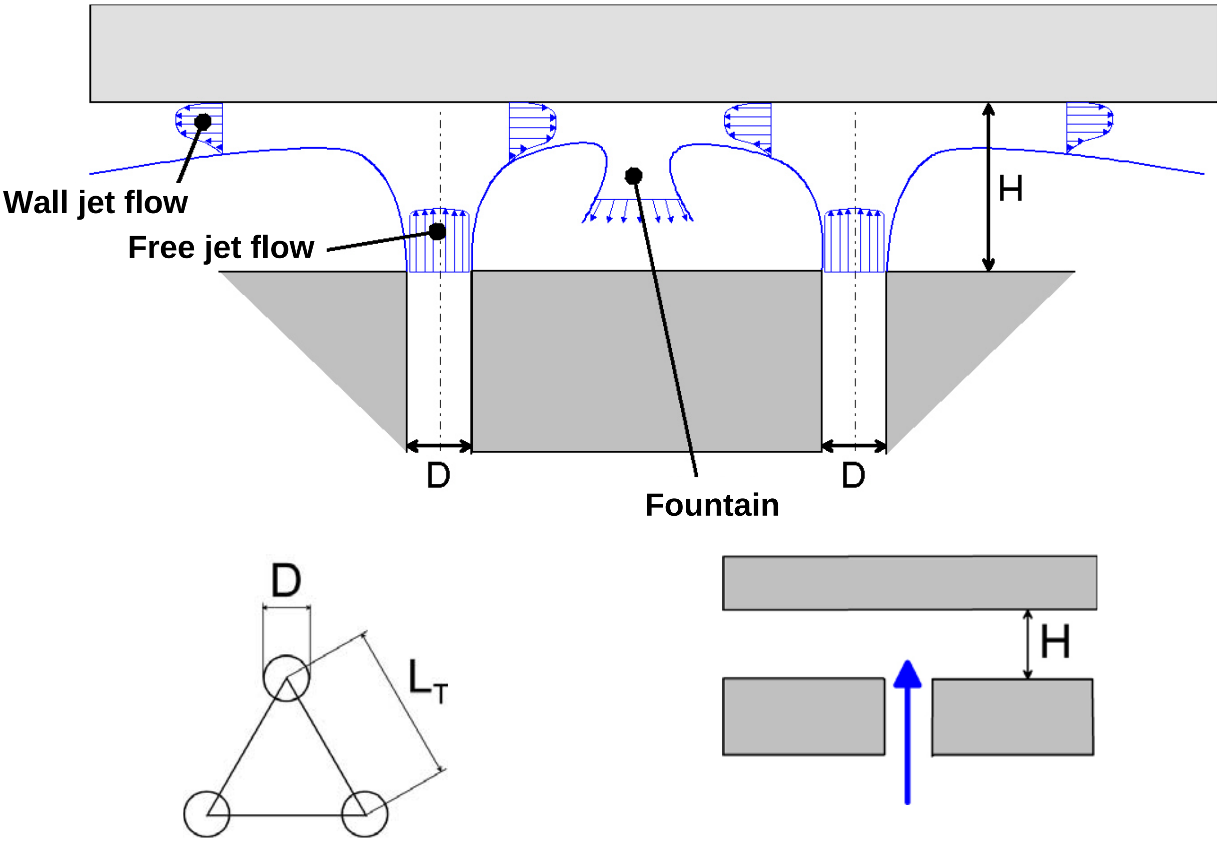

Fig. 2-3: Multiple impingement jet and geometrical parameter model.

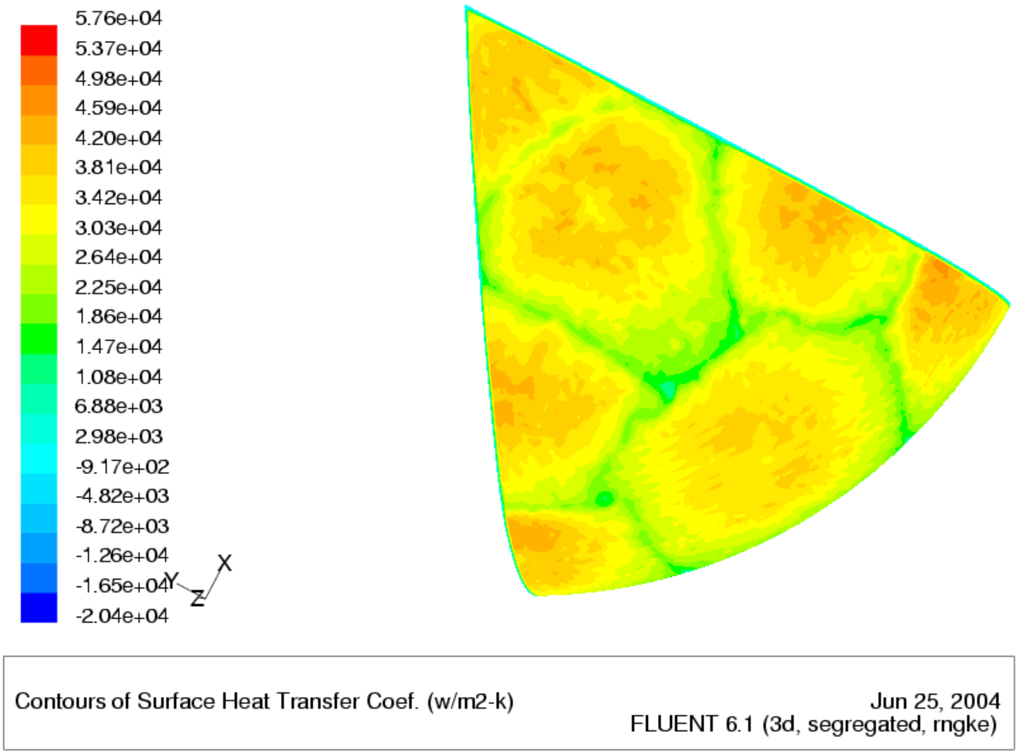

Fig. 2-4: htc distribution of the multiple impingement jet (result obtained from Ch. 6.1).

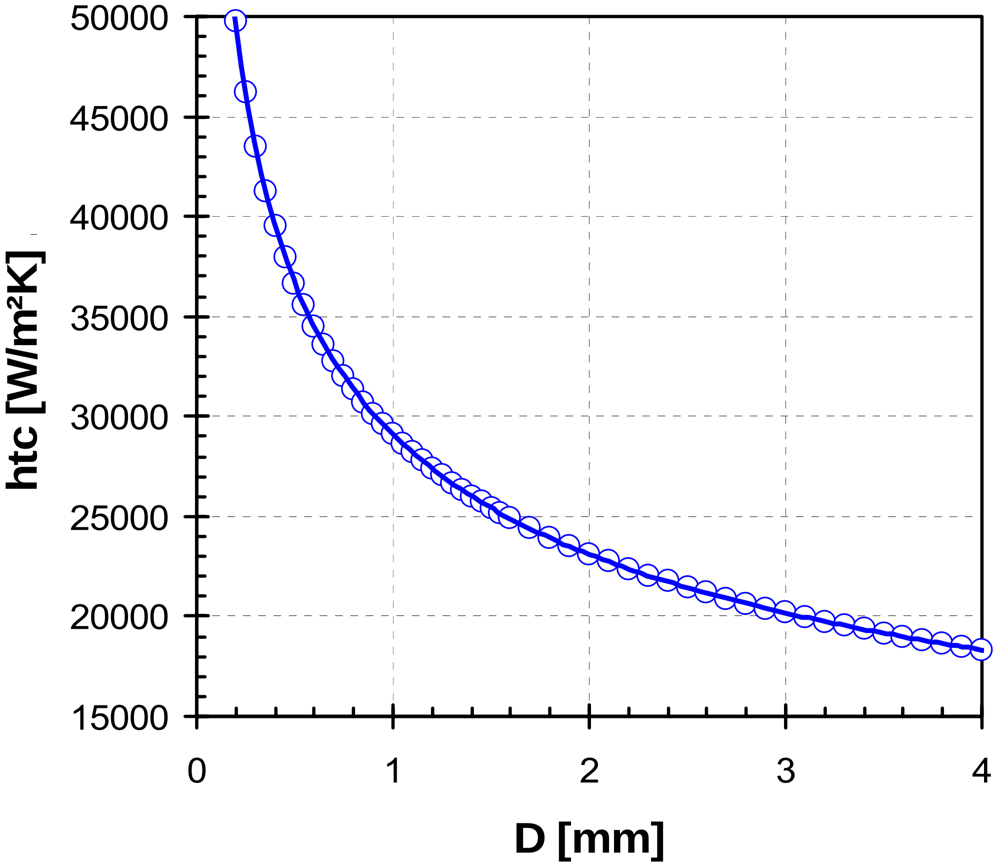

Fig. 2-5: htc versus jet hole diameter D, (mass flow, G and pressure ratio constant).

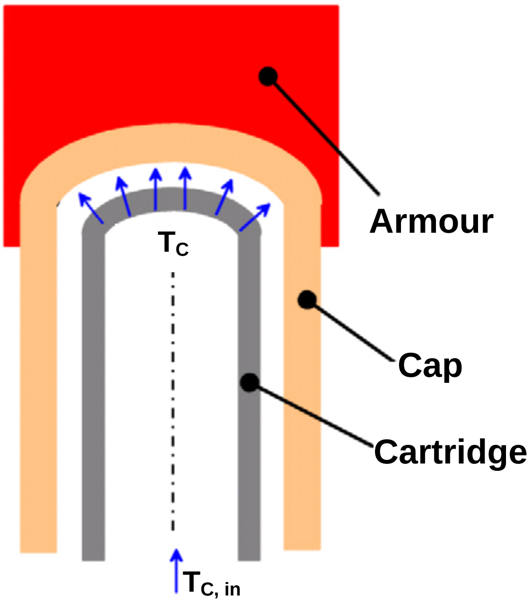

Fig. 2-6: Principle of a jet impingement cooling finger for the gas-cooled divertor.

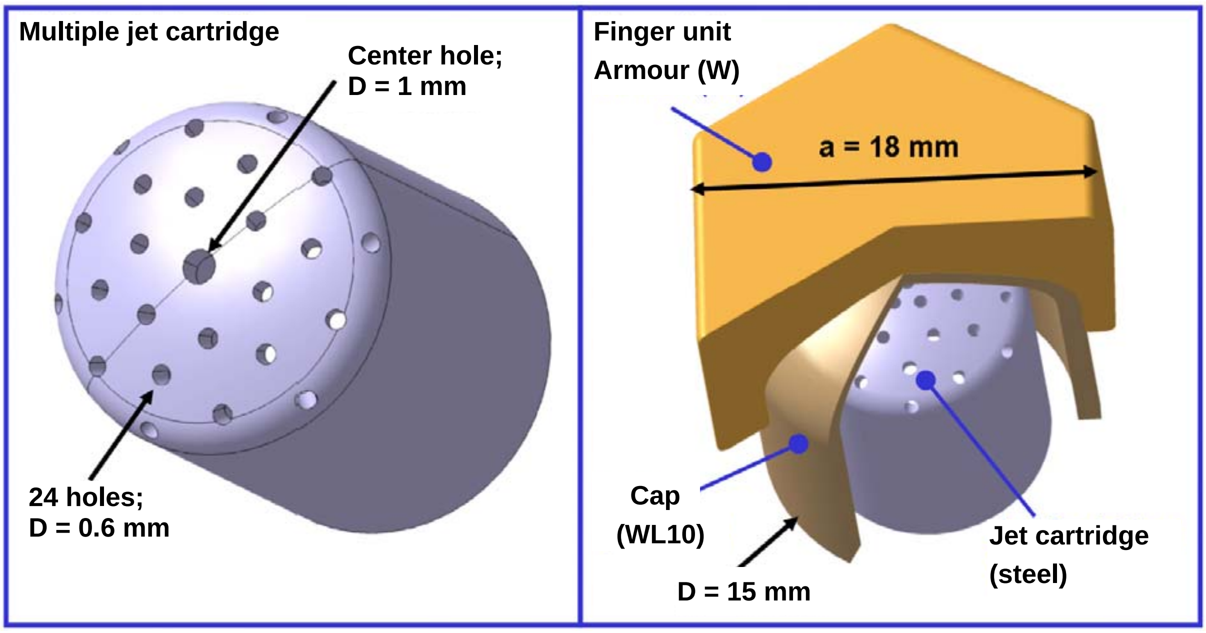

Fig. 2-7: Exemplary layout of a jet impingement cooling finger for the gas-cooled divertor.

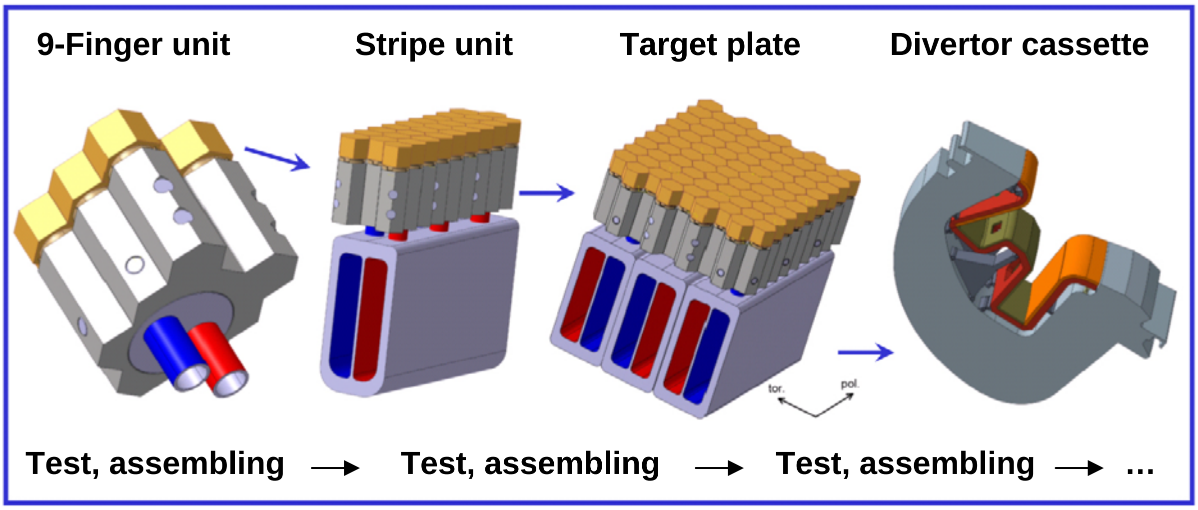

Fig. 2-8: FZK design of a gas-cooled divertor cassette with a large number of cooling fingers.

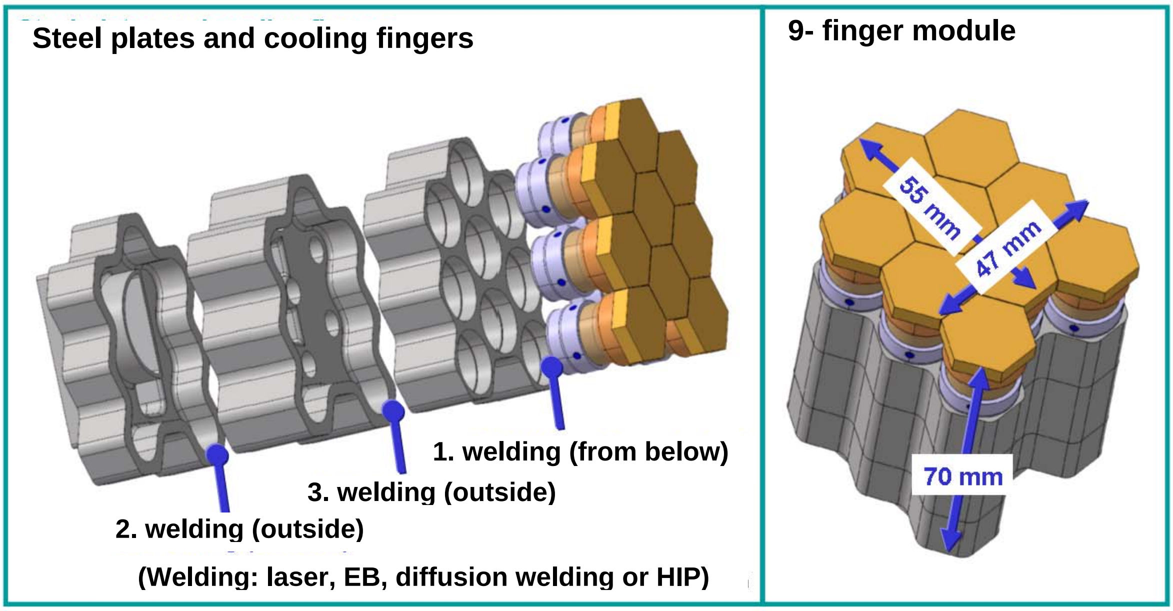

Fig. 2-9: Multiple cooling finger housing, steel-tungsten joints.

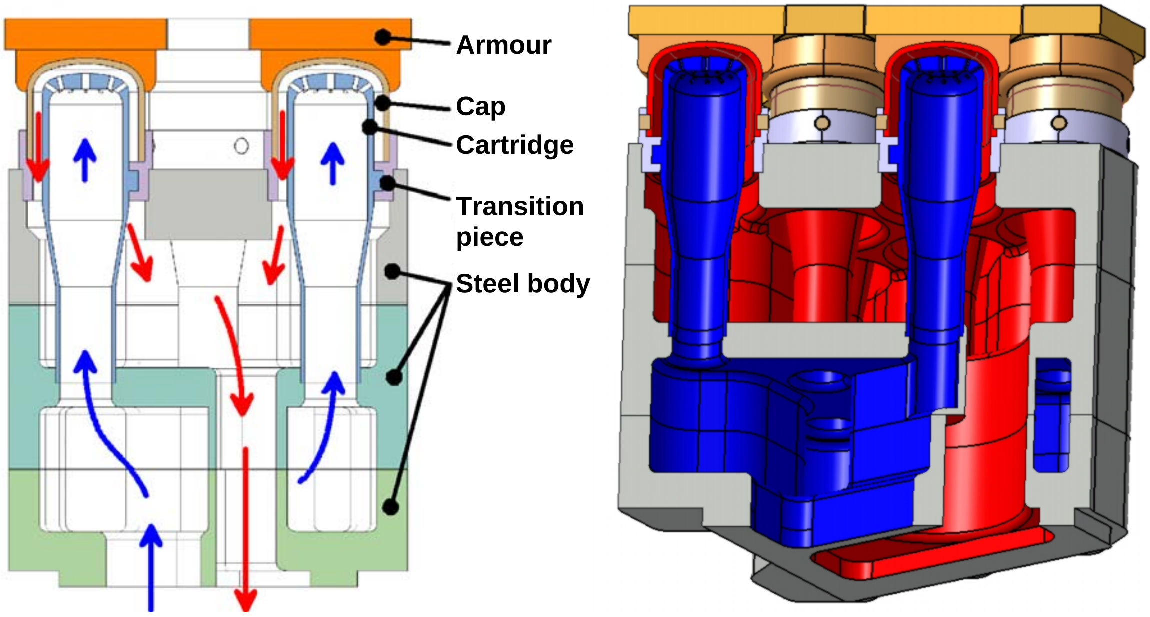

Fig. 2.10: Cross section of the multiple cooling finger housing (left 2D, right 3D CAD).

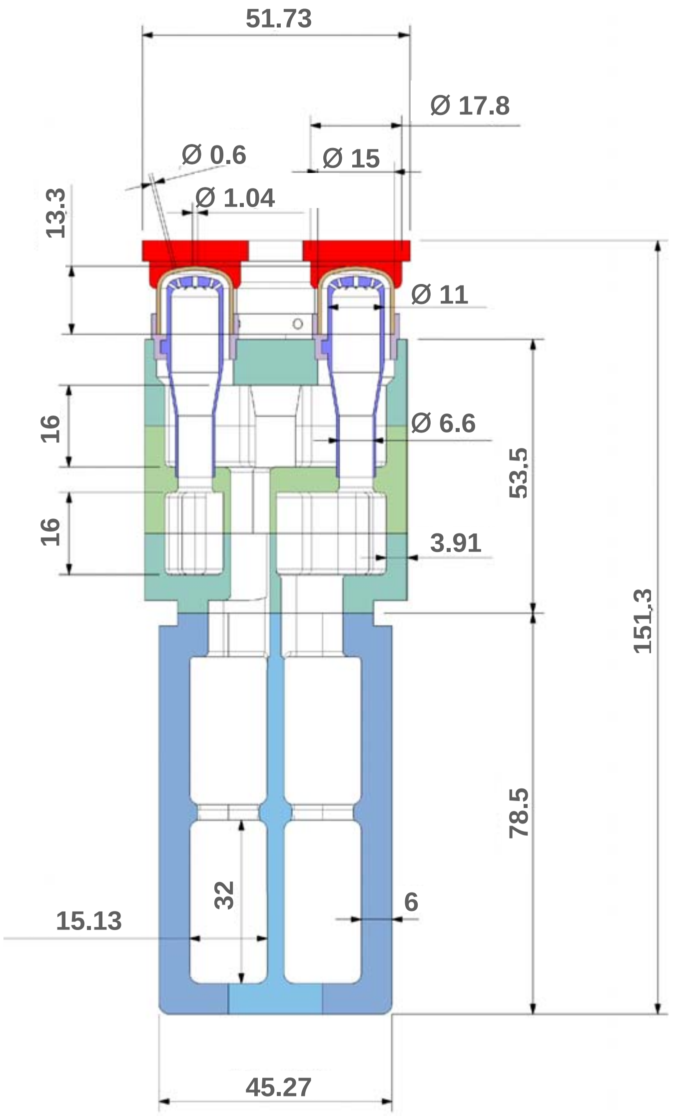

Fig. 2.11: Dimensions of the multiple cooling finger housing.

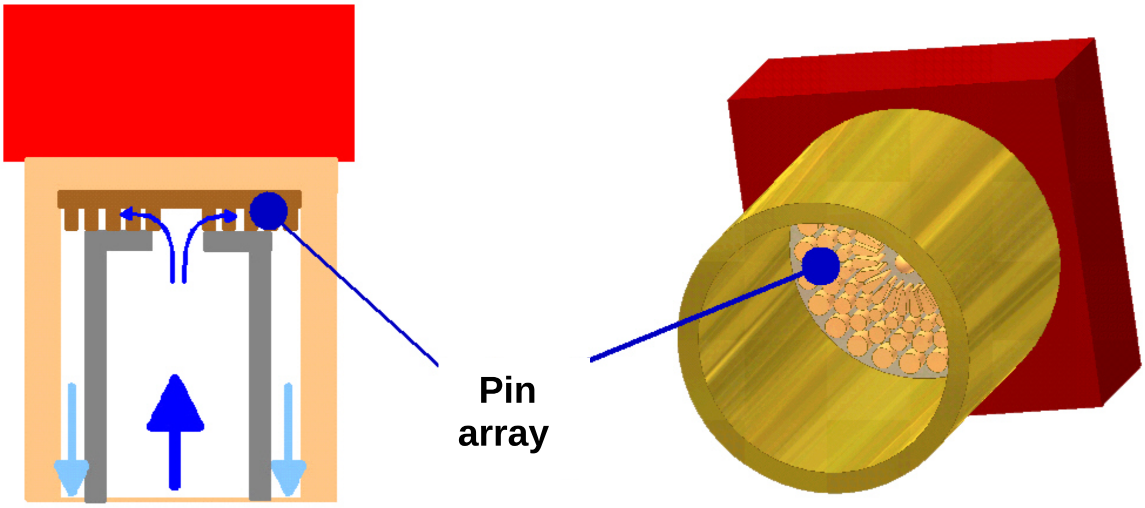

Fig. 2-12: Principle of the pin array cooling finger for the gas-cooled divertor.

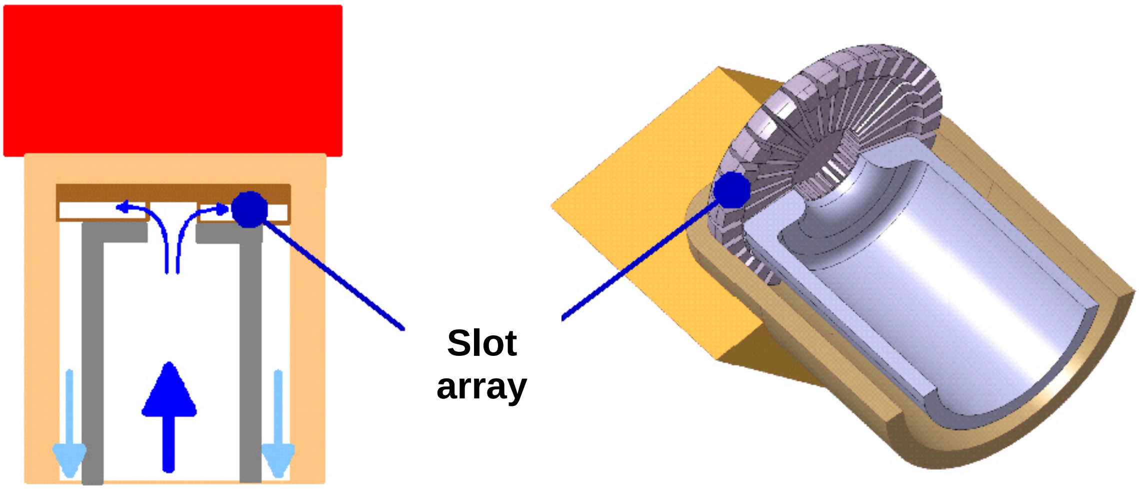

Fig. 2-13: Principle of a slot array cooling finger for the gas-cooled divertor.

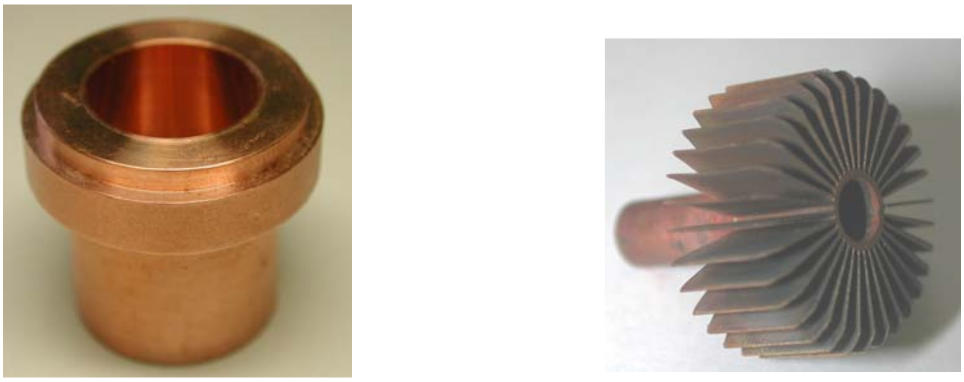

Cup unit

Copper electrodes for EDM (Ø12.8 mm, 32 blades)

HEMS S1-b (h=1.2 mm)

Fig. 3.1-1: EDM of HEMS mock-ups from CuCrZr for GPF experiments.

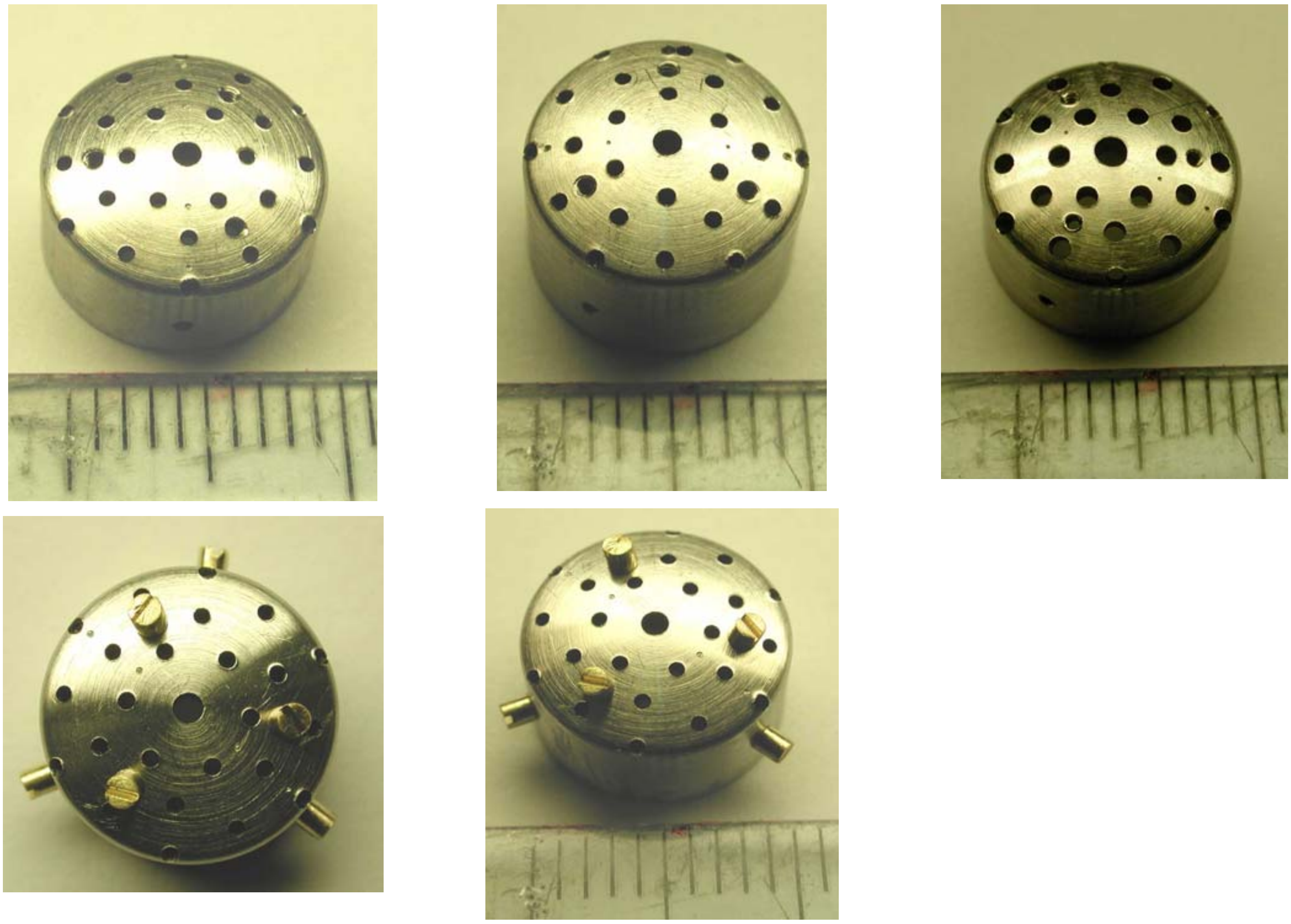

Cartridge J1-a-m

Cartridge J1-a-mx2

Cartridge J1-e-m

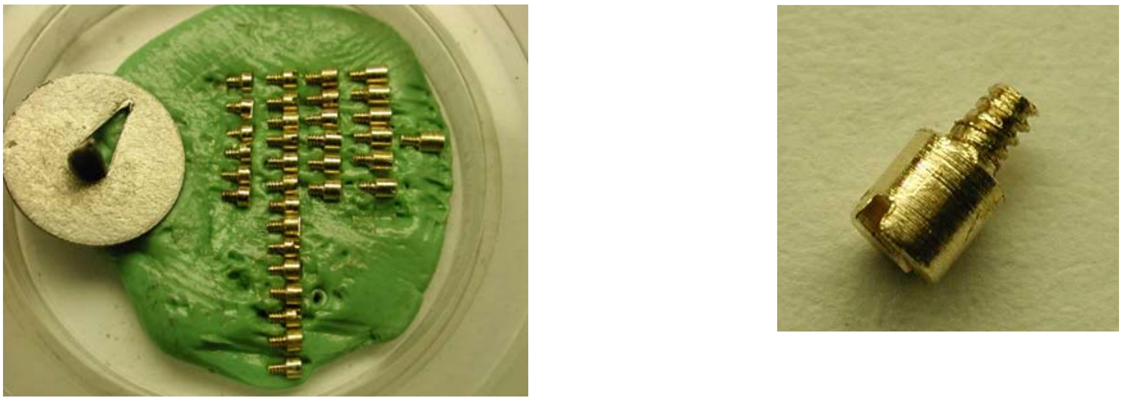

Spacers (screw diameter is 0.7 mm)

Cartridge with tube and thimble

Fig. 3.1-2: HEMJ cartridges and spacers for the second GPF test campaign.

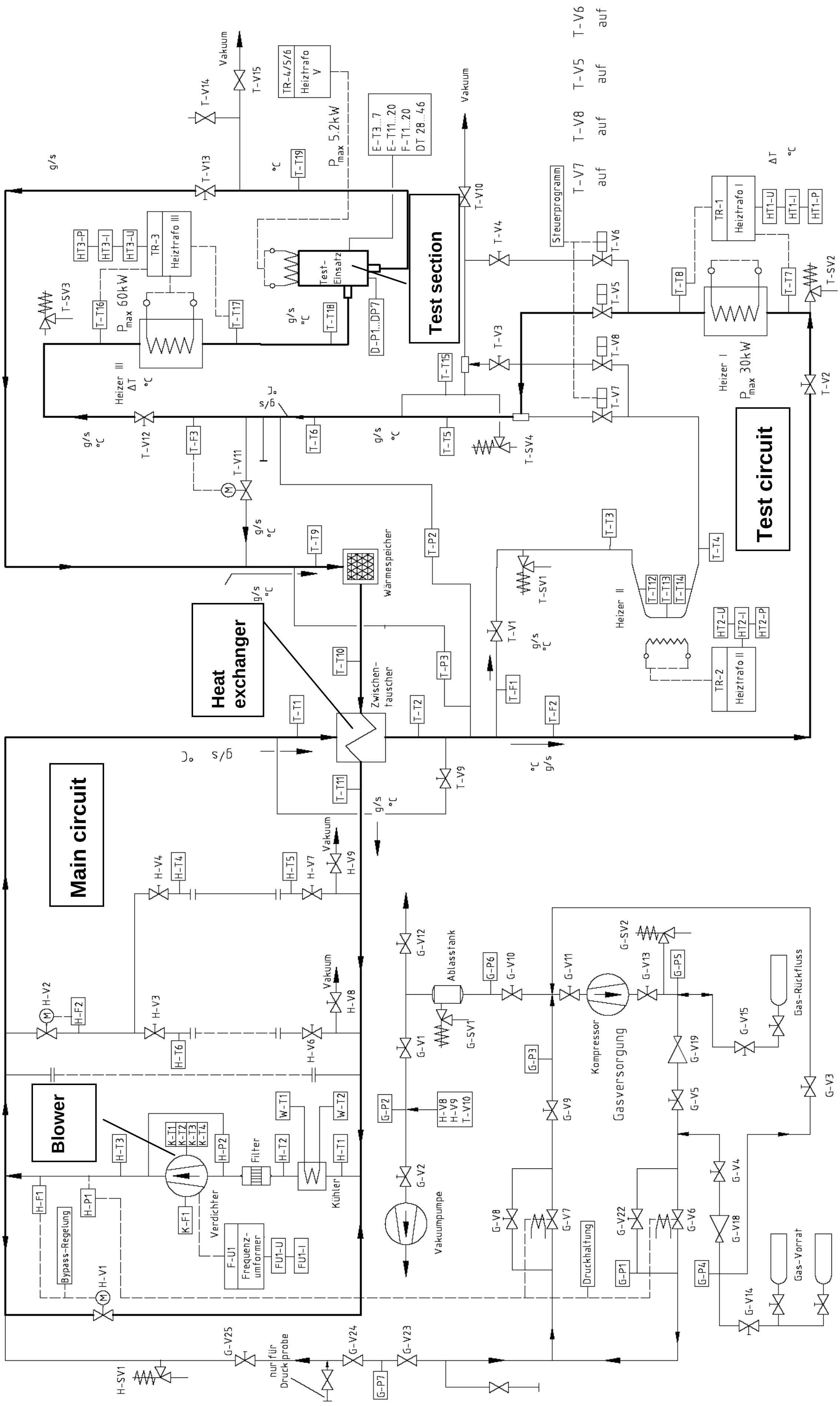

Fig. 3.2-1: Helium blanket/divertor test loop (HEBLO).

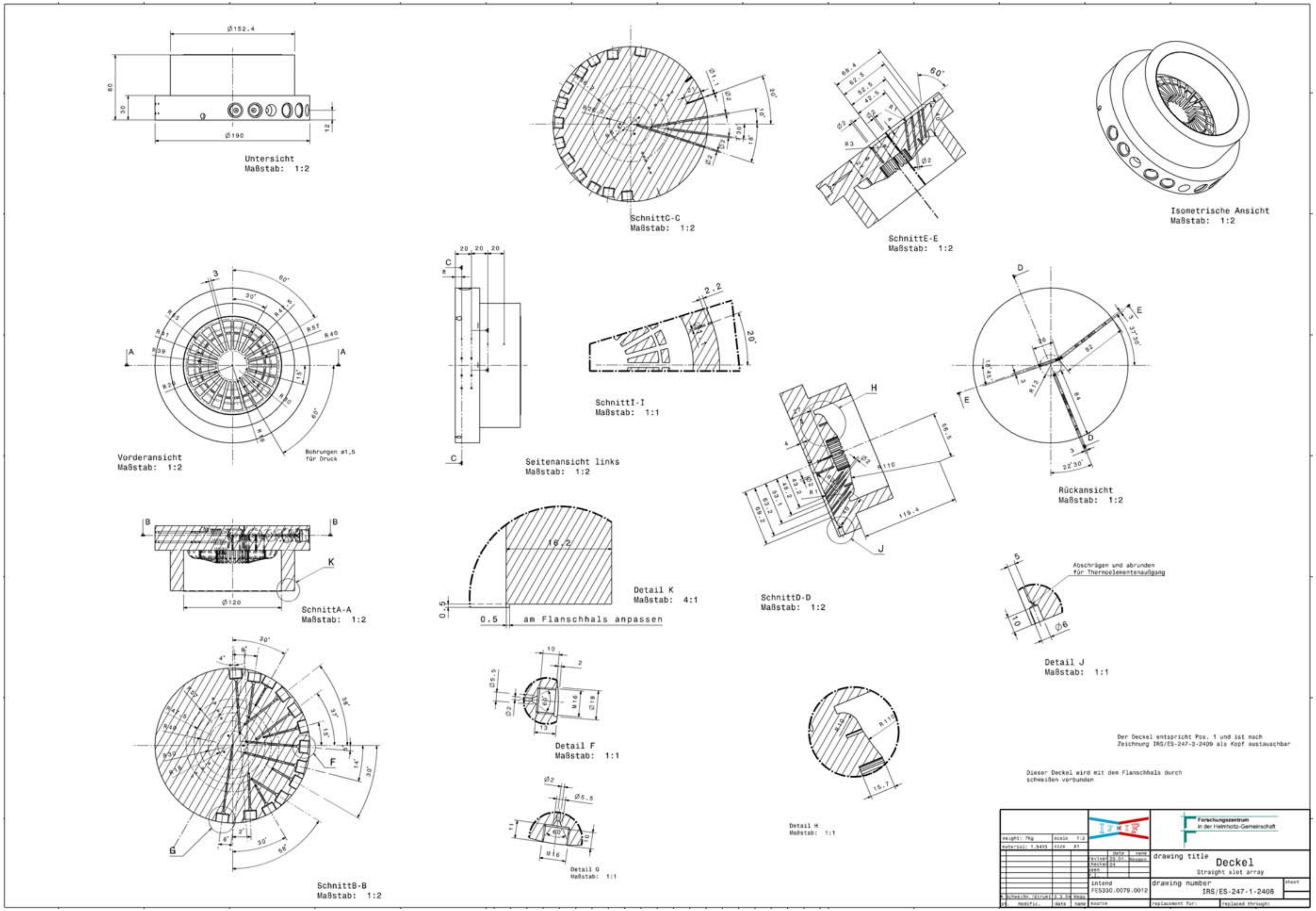

Fig. 3.2-2: HEBLO mock-up instrumentation.

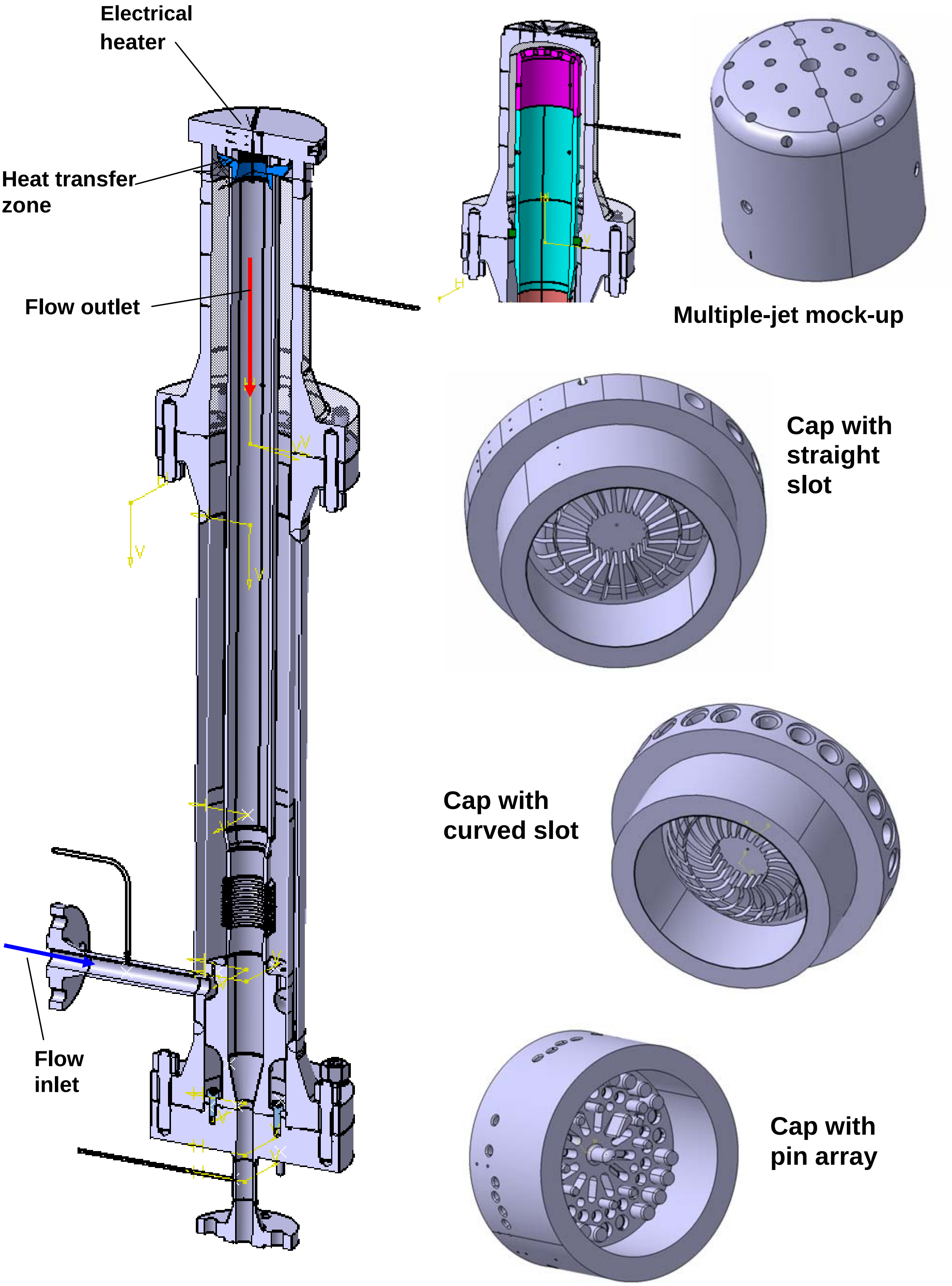

Fig. 3.2-3: HEBLO test section for various mock-ups.

Fig. 3.3-1: SC (left) and lanthanated (right) tungsten after machining.

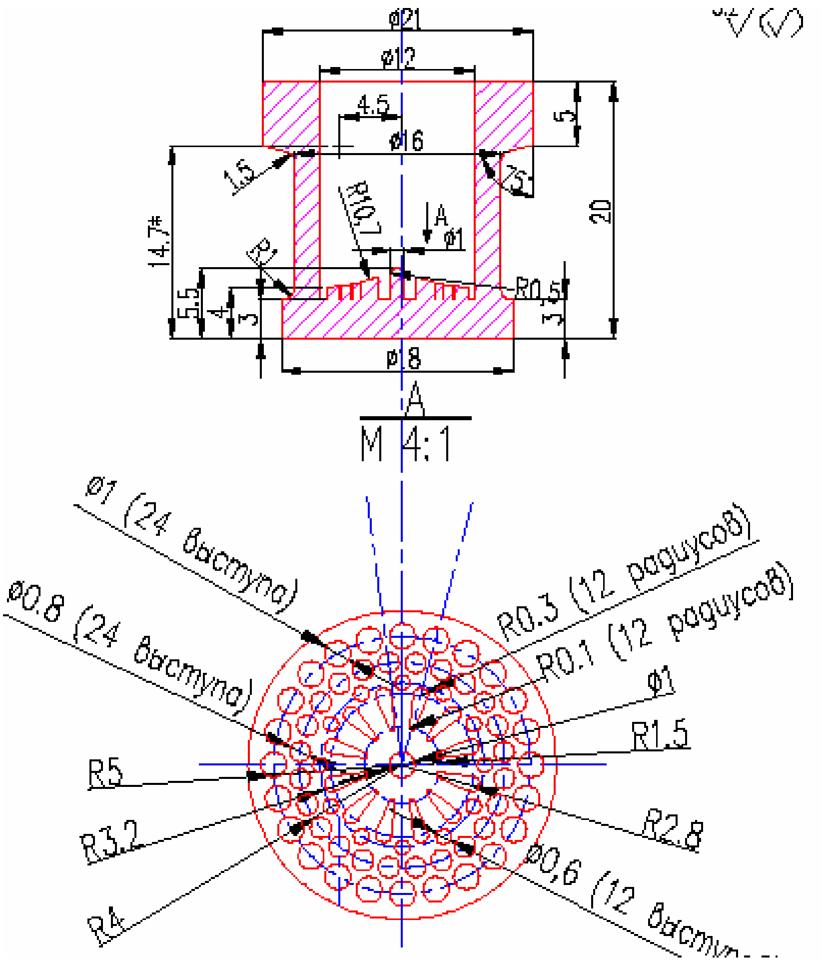

Fig. 4.1-1: The thimble with the pin array structure inside.

Fig. 4.1-2: Electrodes for the EDM of the FZK pin array design.

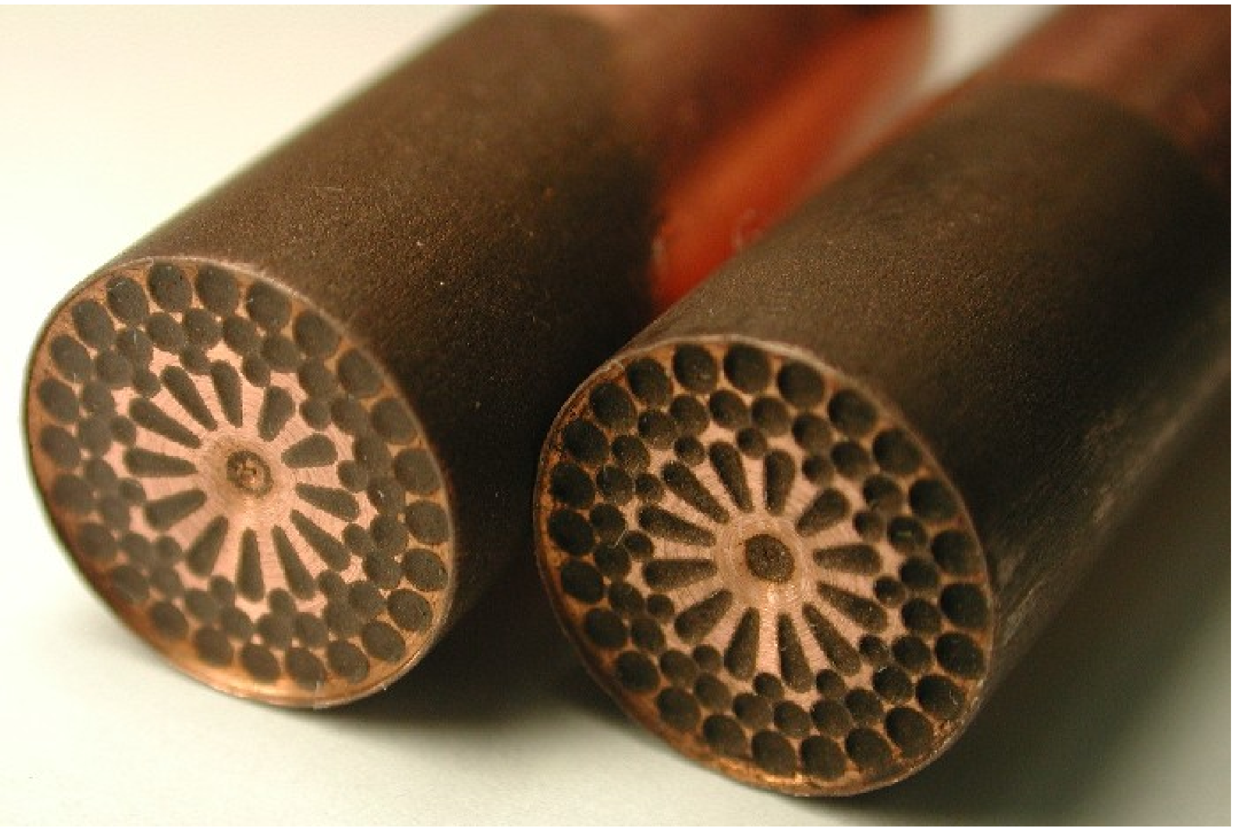

Fig. 4.1-3: Cone-shaped electrodes after machining.

Fig. 4.1-4: Tungsten thimble with pin array structure, fabricated by EDM.

Fig. 4.1-5: The view of the electrodes after EDM.

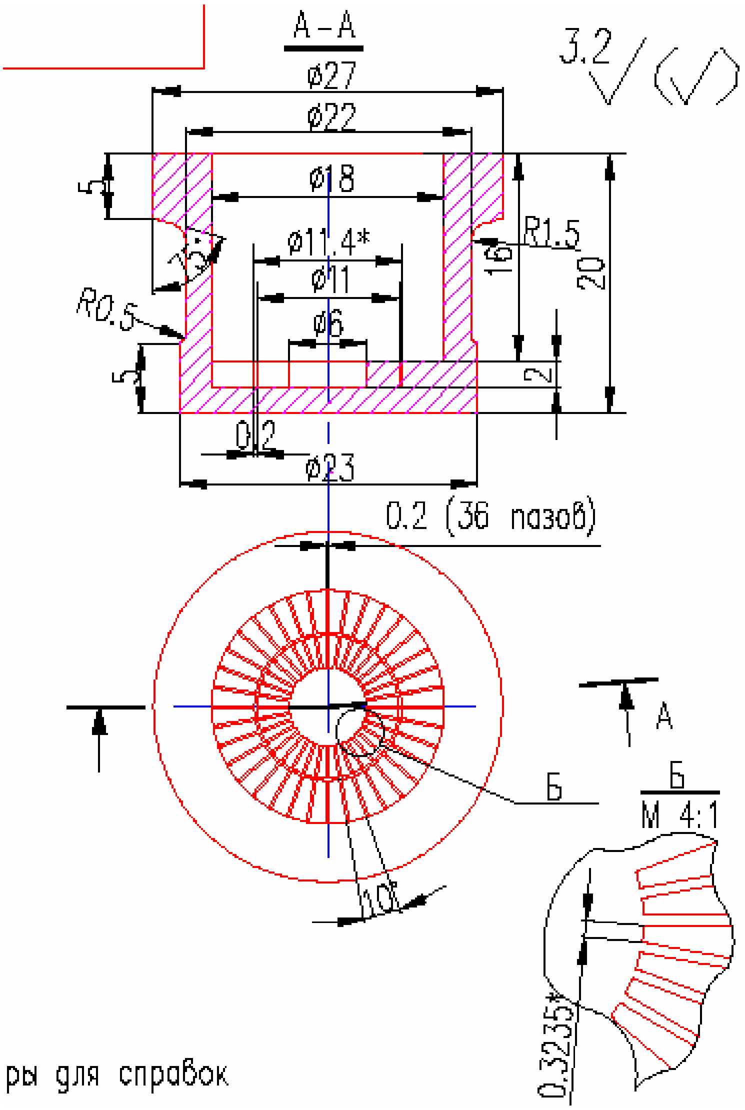

Fig. 4.1-6: Drawing of the thimble with slots.

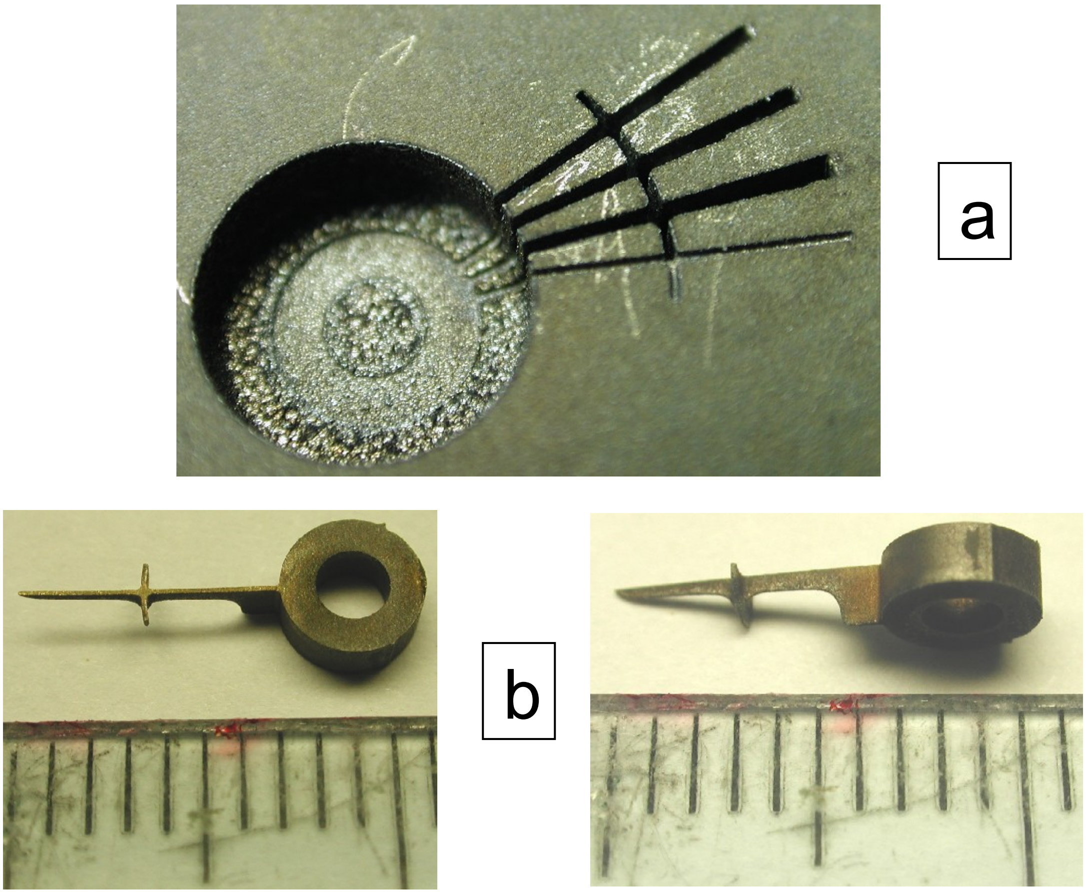

Fig. 4.1-7: EDM tests on tungsten using W electrodes
(a – tungsten sample after EDM, b – W electrode after EDM).

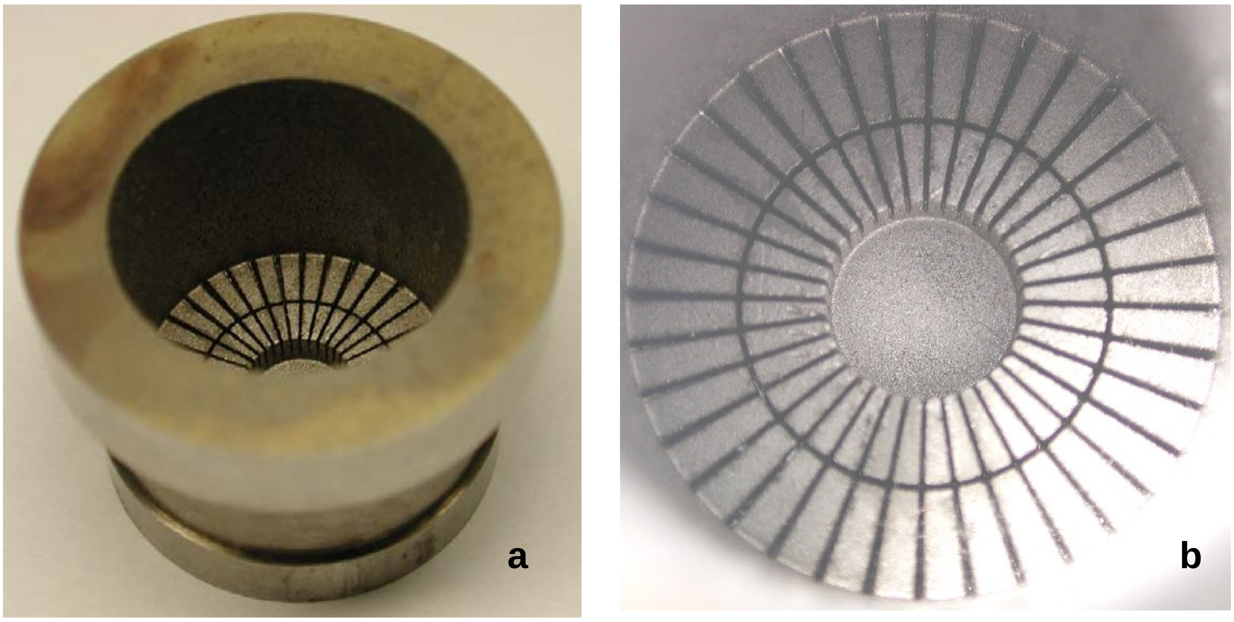

Fig. 4.1-8: Tungsten thimble with slots (Efremov design)
(a – thimble view, b – slots at the bottom).

Fig. 4.1-9: Cracks in the tungsten thimble.

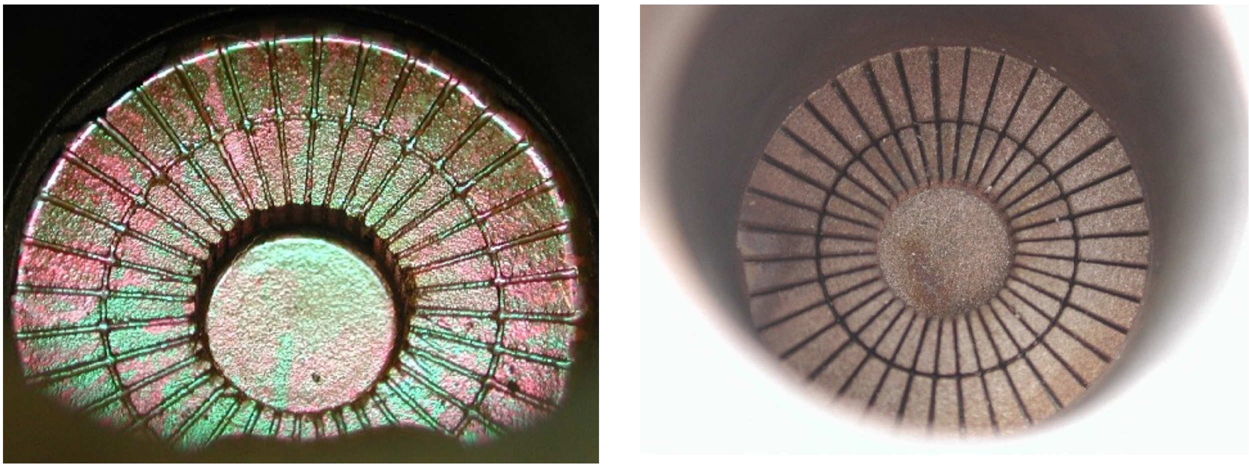

Fig. 4.1-10: Tungsten gaps (a-filled by copper, b- after etching).

Fig. 4.2-1: W sample with 1-mm pin prepared by ECM at Ufa, Russia.

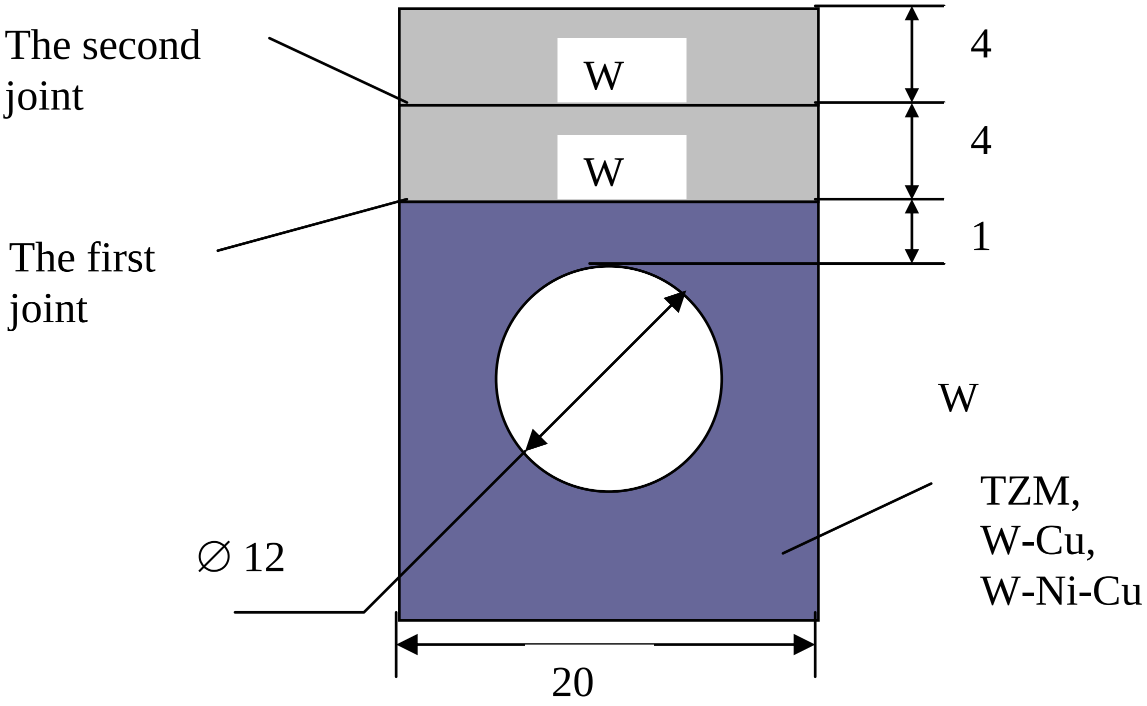

Fig. 4.4-1: Geometry of the mock-up used for the development of the W/W joint.

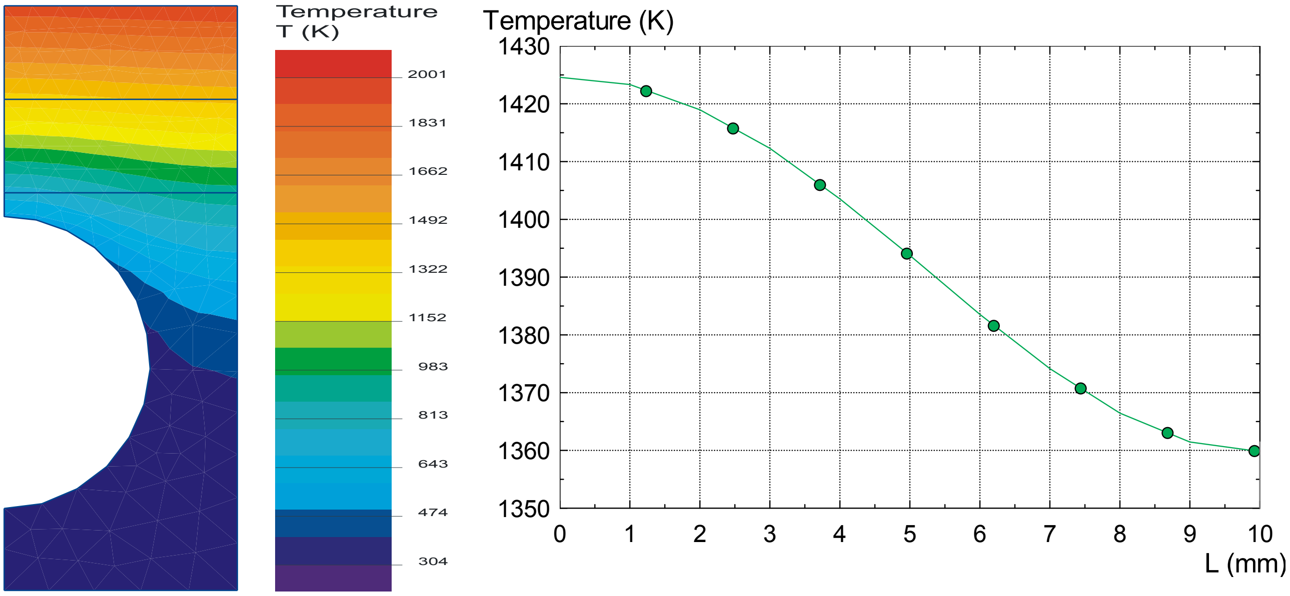

Temperature field of the mock-up at a heat flux of 15 MW/m^2

Temperature at the W/W bonding line

Fig. 4.4-2: Modelling of temperature fields in the mock-up at a heat flux of 15 MW/m^2.

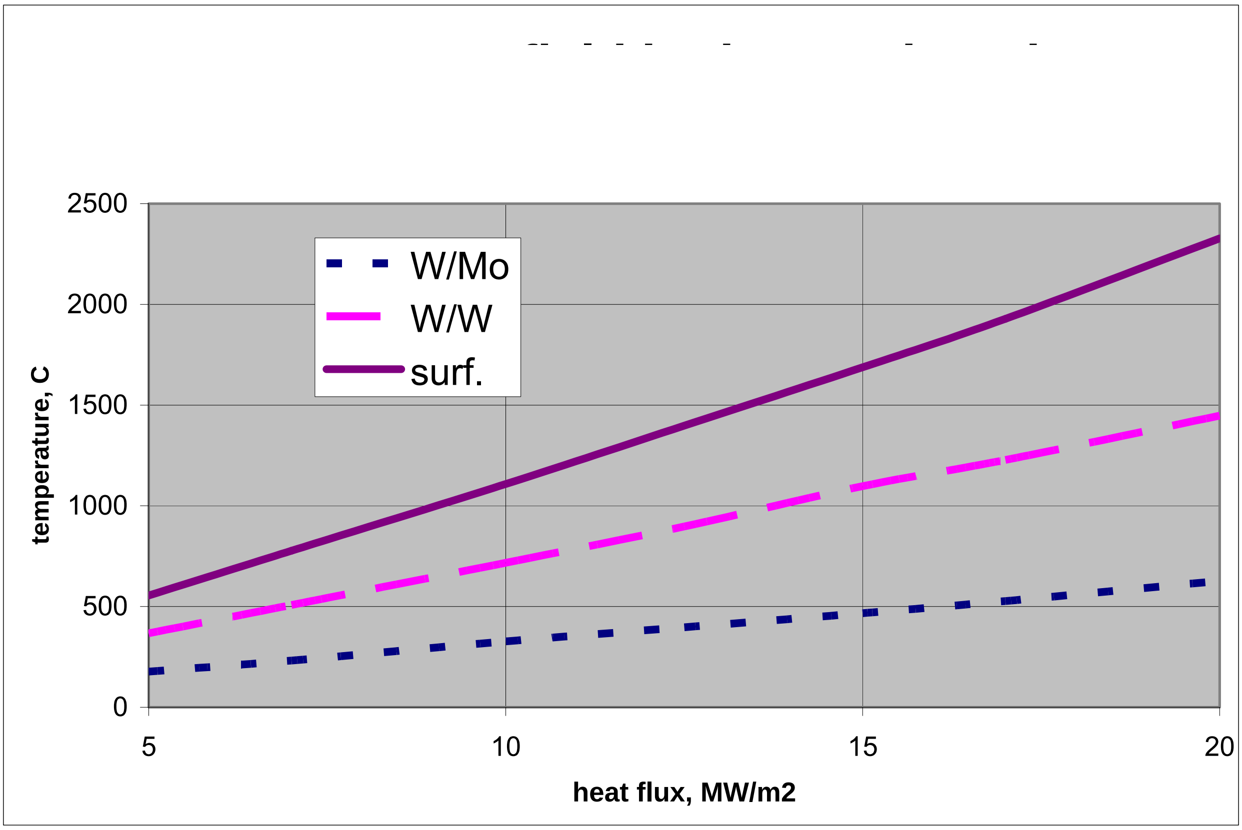

Fig. 4.4-3: Temperature field in the mock-up as a function of the absorbed heat flux.

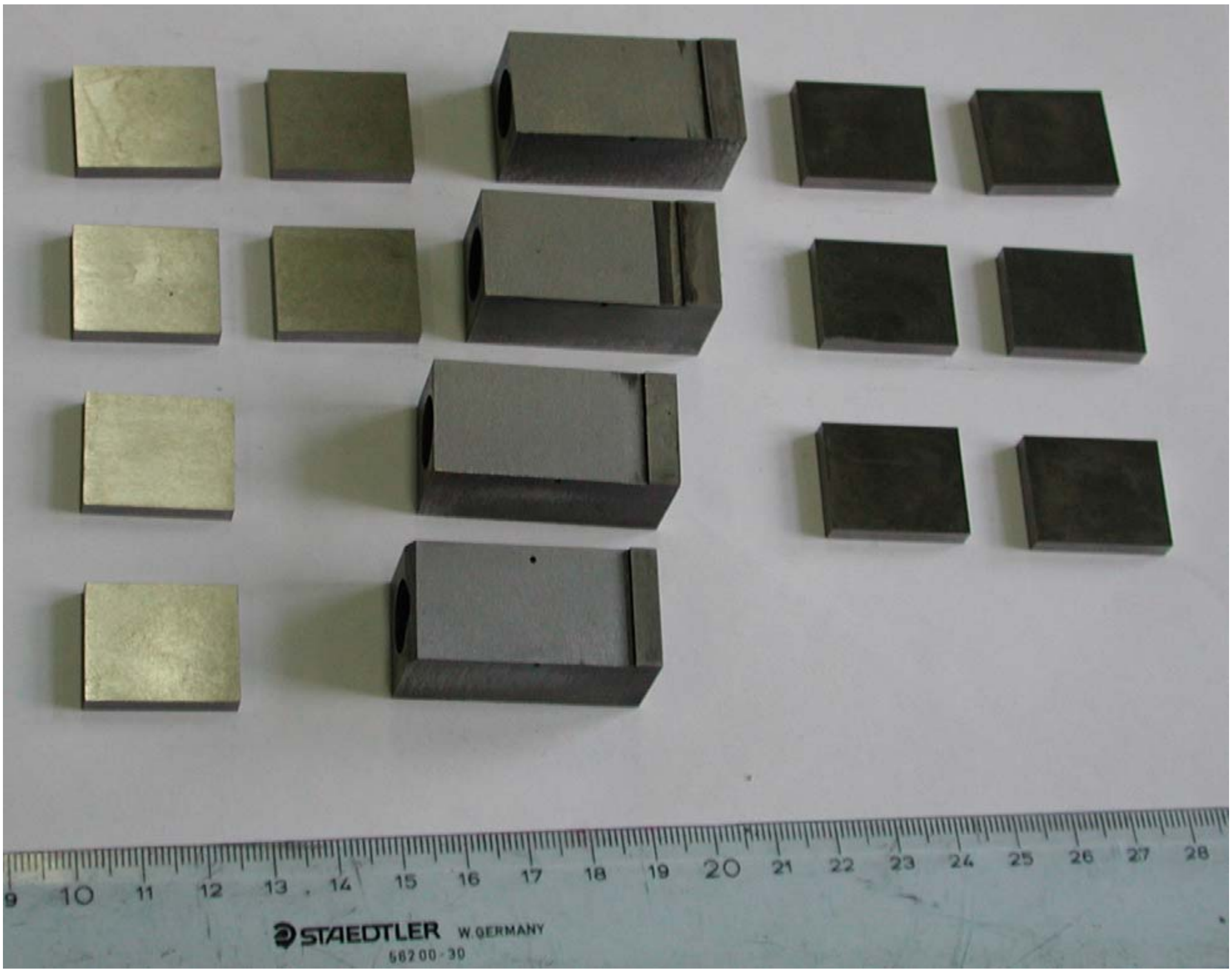

Fig. 4.4-4: Mock-up parts for the development of the W/W joint
(water-cooled heat sink from TZM and W tiles from sintered rolled tungsten).

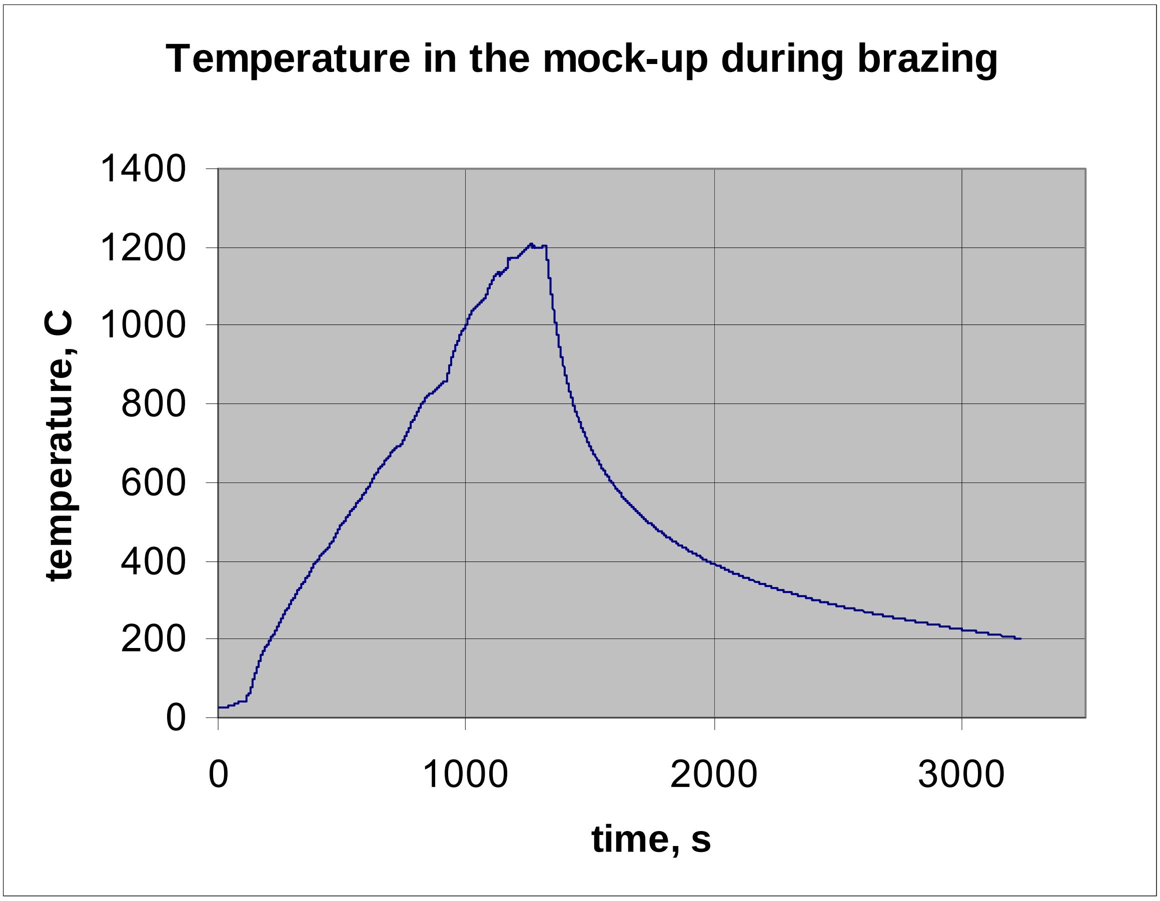

Fig. 4.4-5: Temperature in the mock-up during brazing with 71KHCP filler metal.

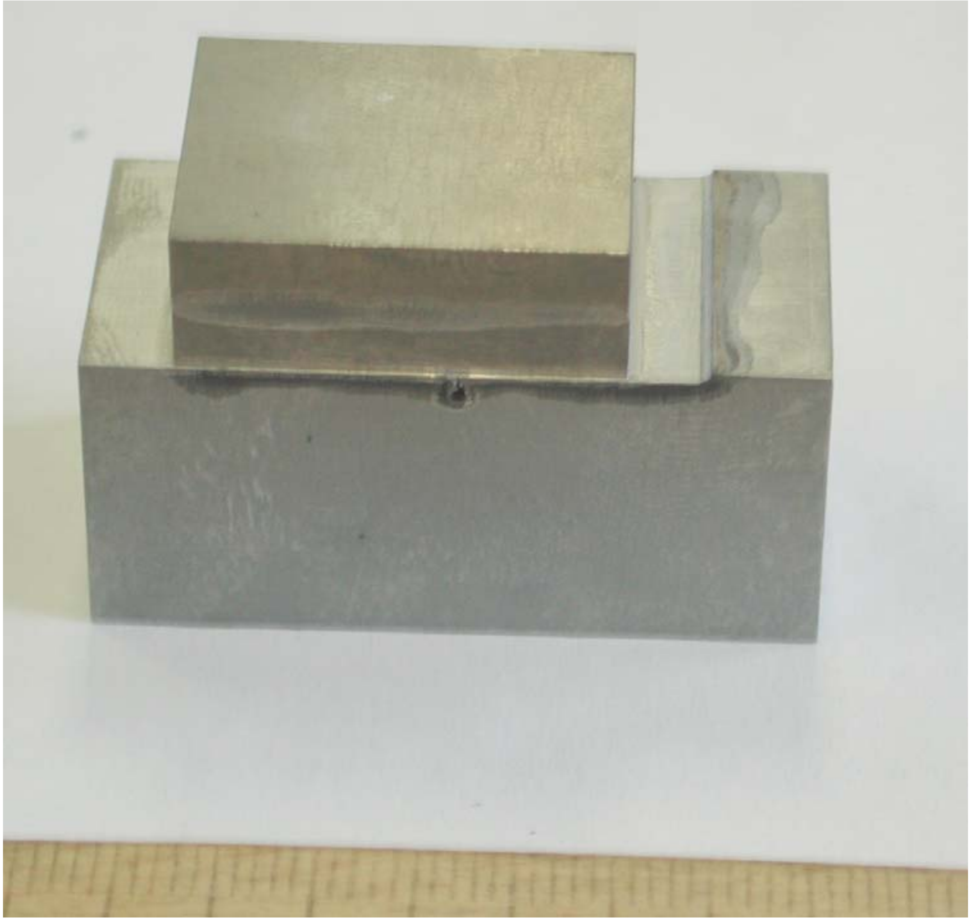

Fig. 4.4-6: Mock-up brazed with 71KHCP filler metal.

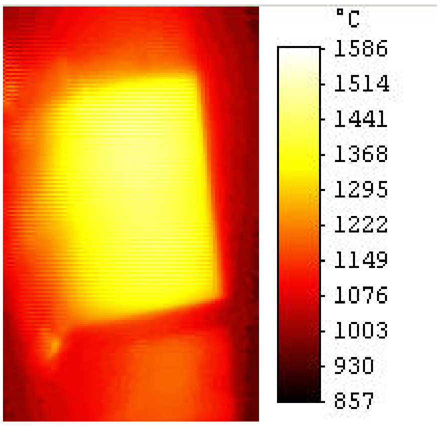

IR of the mock-up at 14 MW/m^2

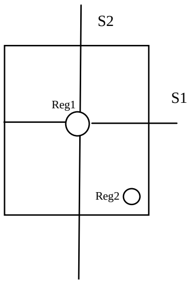

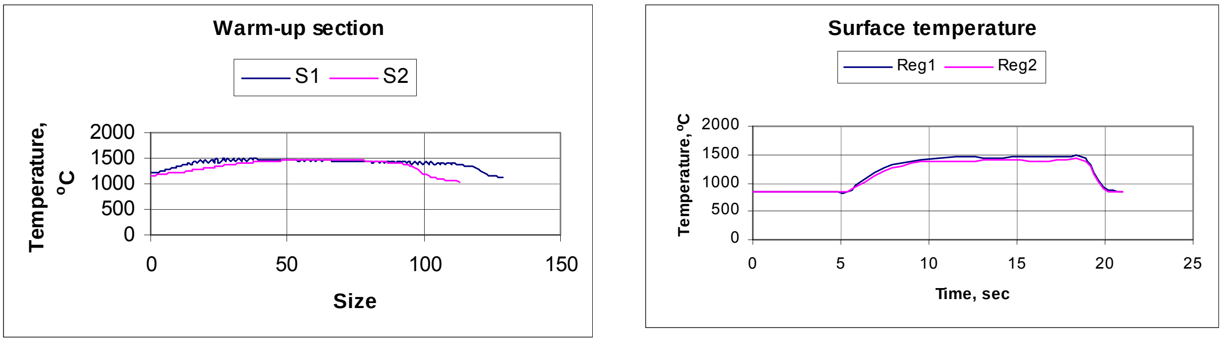

Temperature along the lines S1 and S2

Temperature at points Reg1 and Reg2 versus time

Fig. 4.4-7: Surface temperature of the mock-up at a heat flux of 14 MW/m^2.

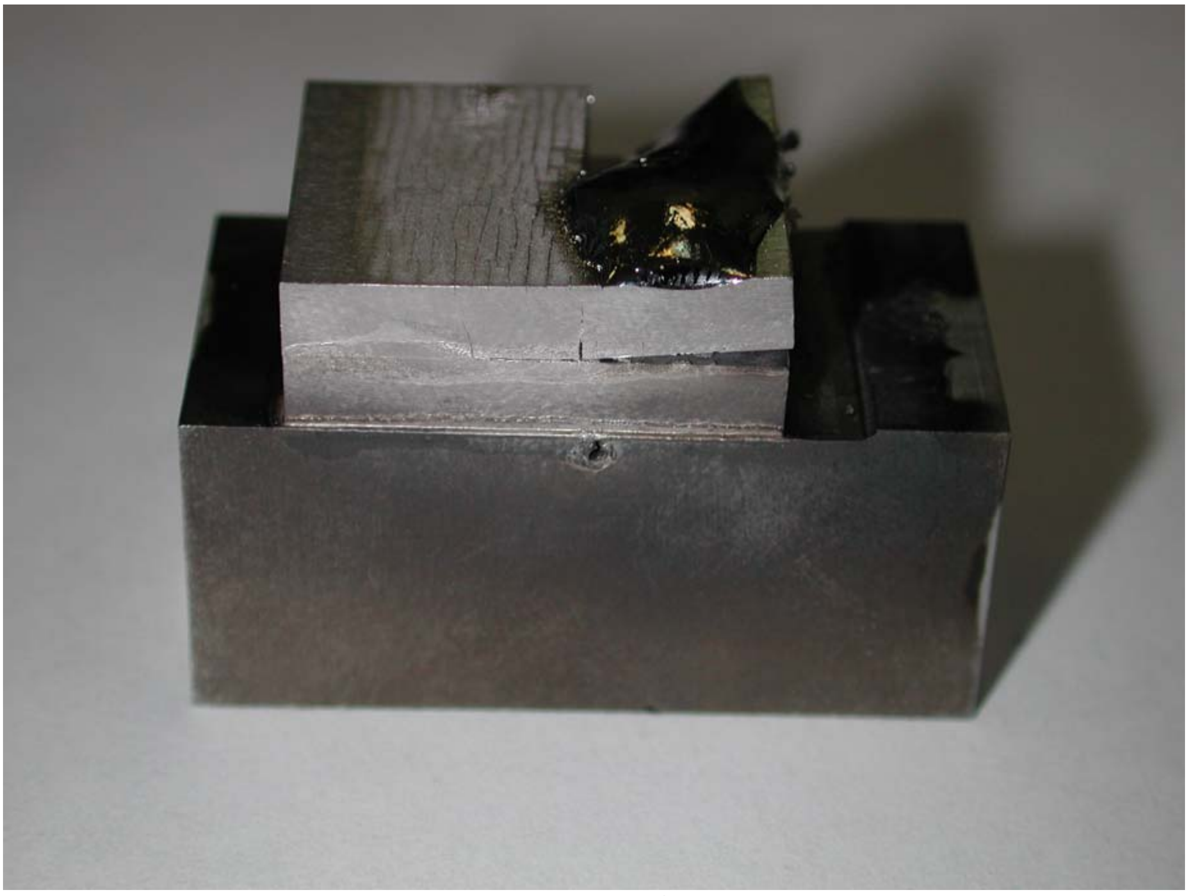

Fig. 4.4-8: Mock-up after the test.

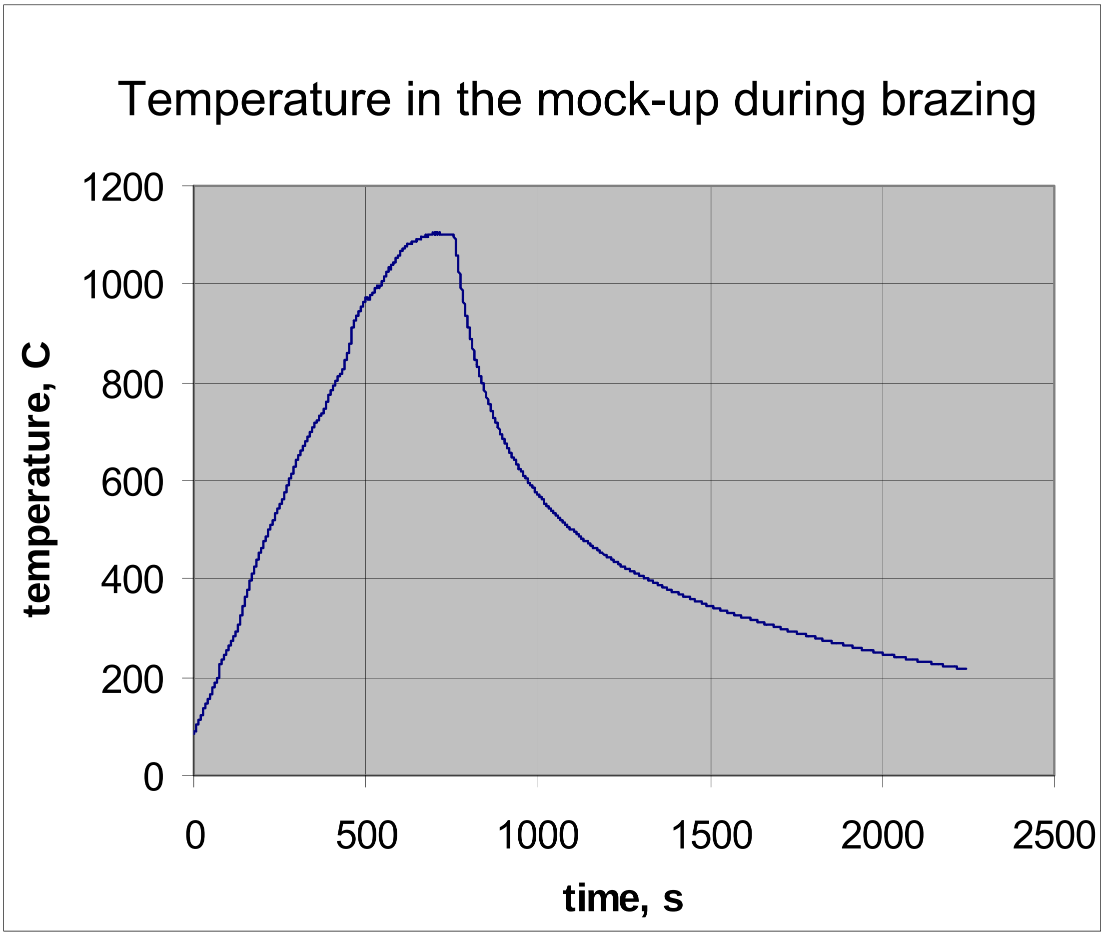

Fig. 4.4-9: Temperature in the mock-up during brazing with STEMET 9 filler metal.

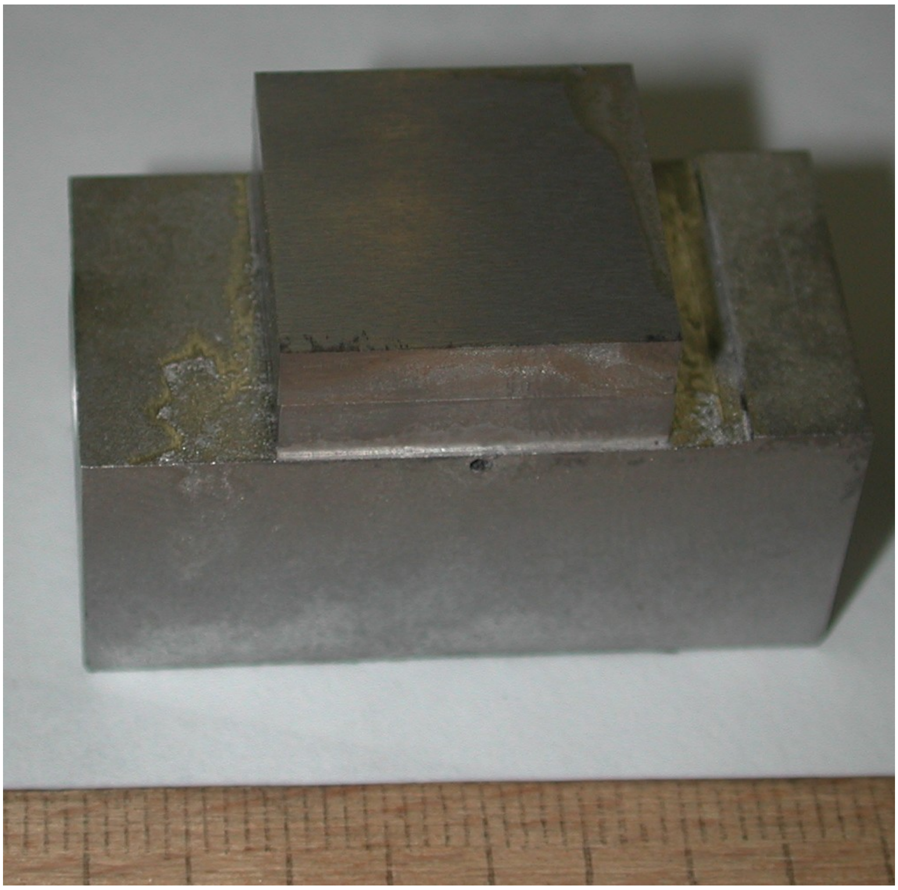

Fig. 4.4-10: Mock-up brazed with STEMET 9 filler metal.

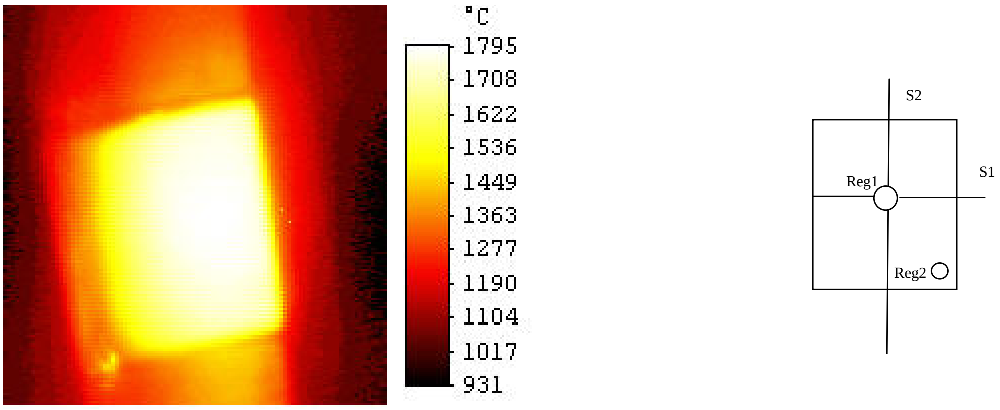

IR of the mock-up at 14 MW/m^2

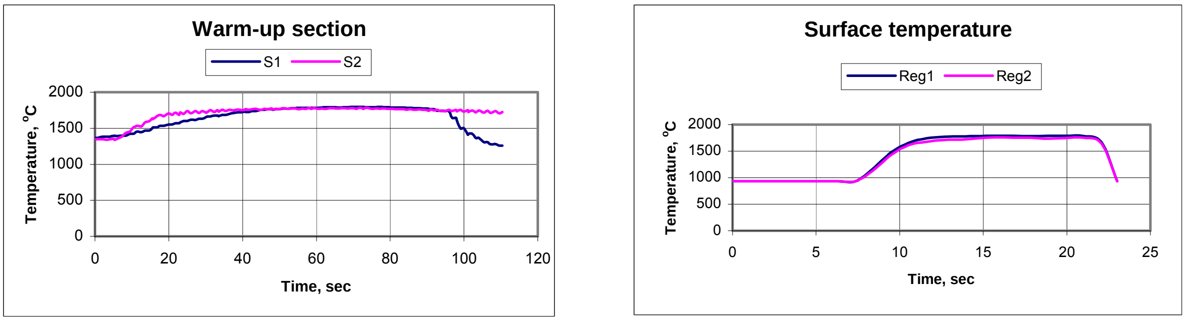

Temperature along the lines S1 and S2

Temperature at points Reg1 and Reg2 versus time

Fig. 4.4-11: Surface temperature of the mock-up at a heat flux of 14 MW/m^2.

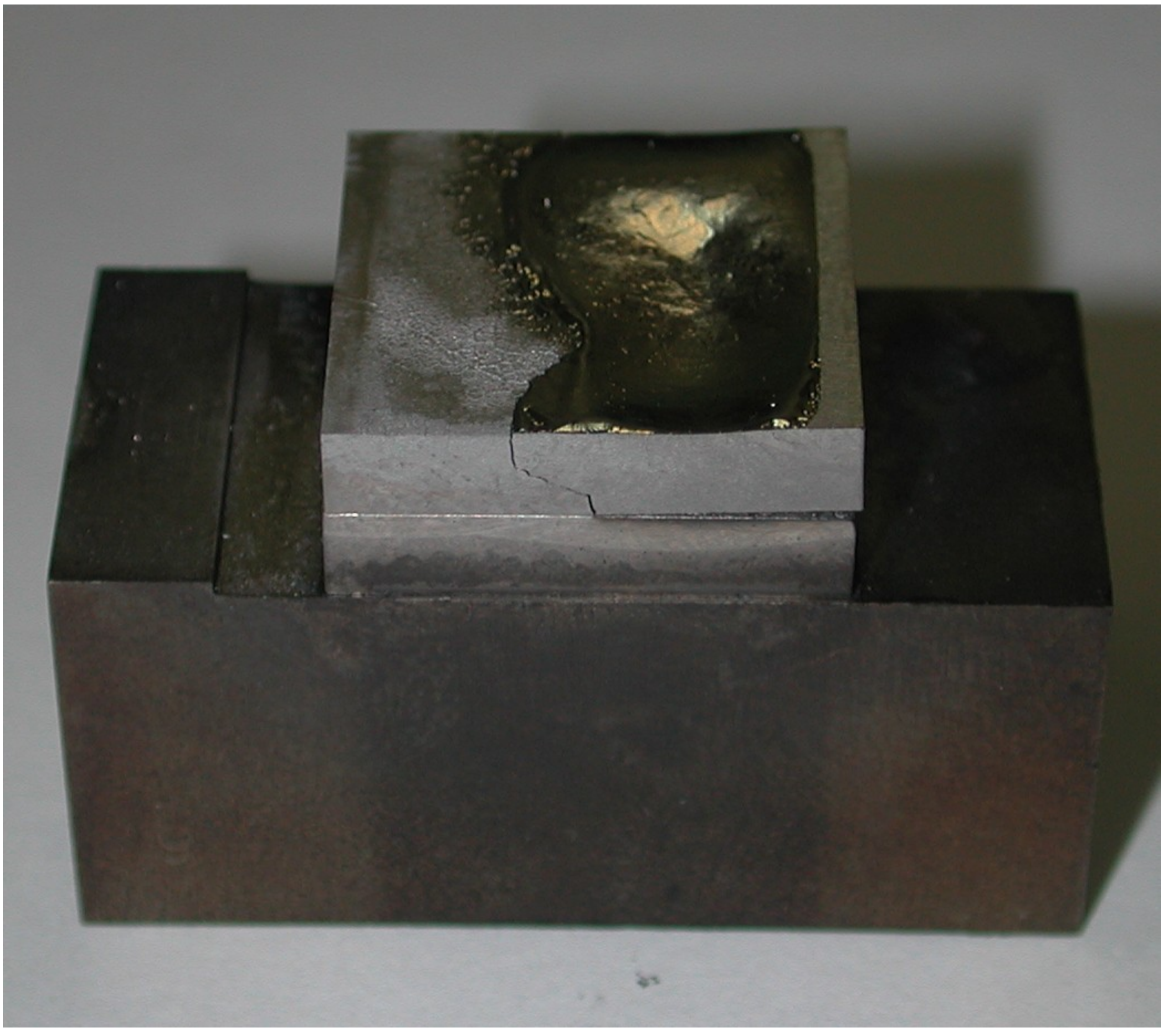

Fig. 4.4-12: Mock-up after the test.

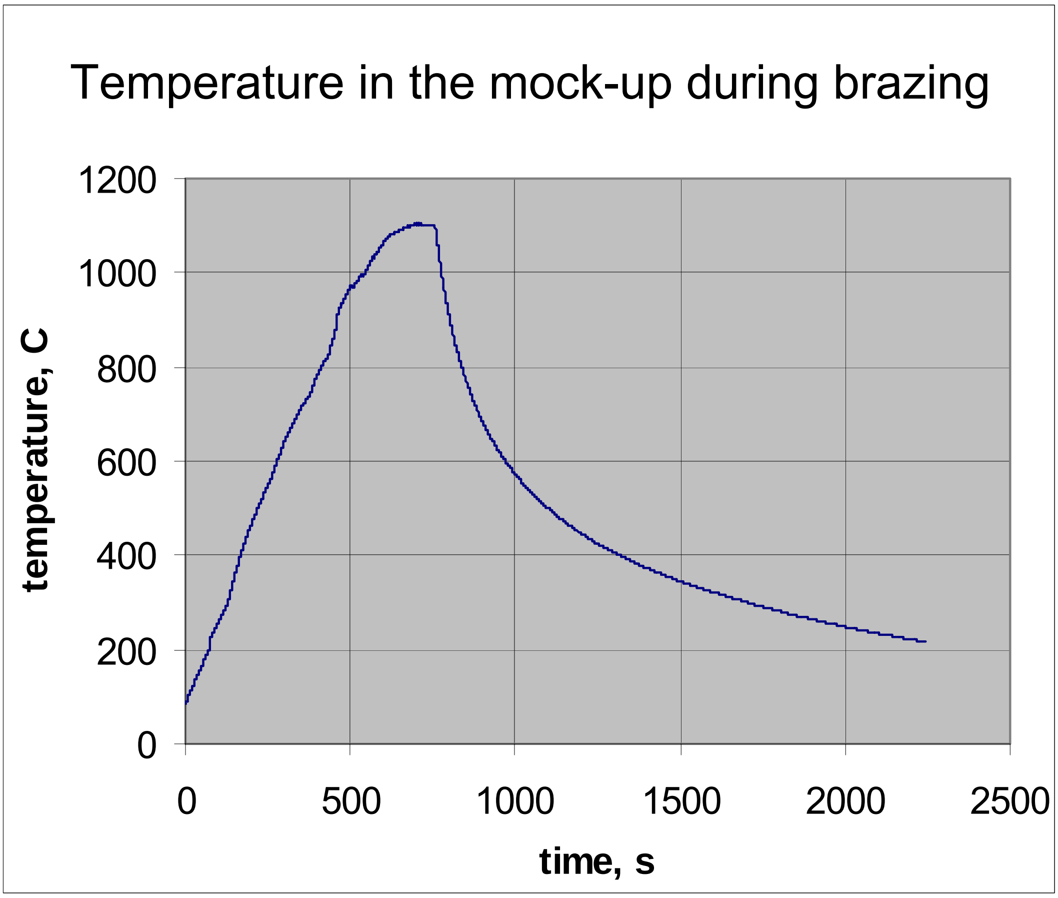

Fig. 4.4-13: Temperature in the mock-up during brazing with STEMET 1311 filler metal.

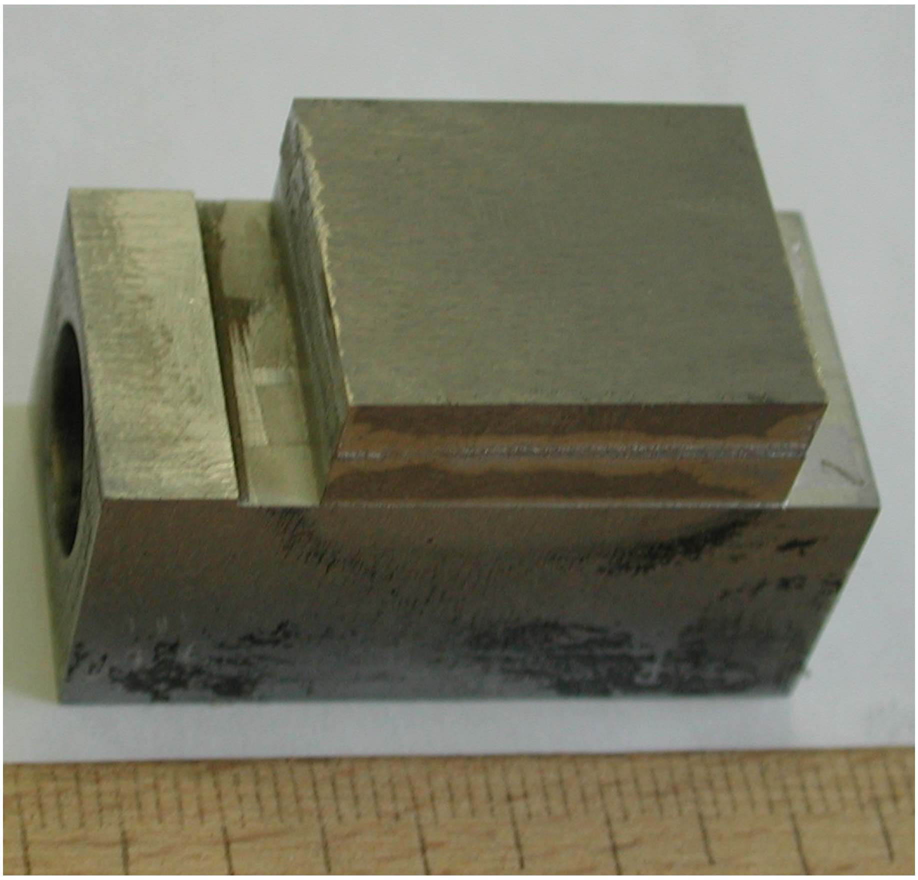

Fig. 4.4-14: Mock-up brazed with STEMET 1311 filler metal.

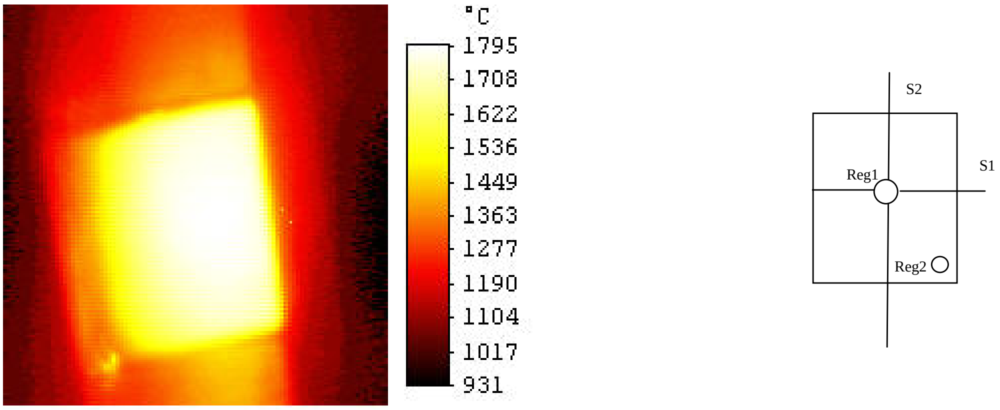

IR of the mock-up at $16\ MW/m^2$

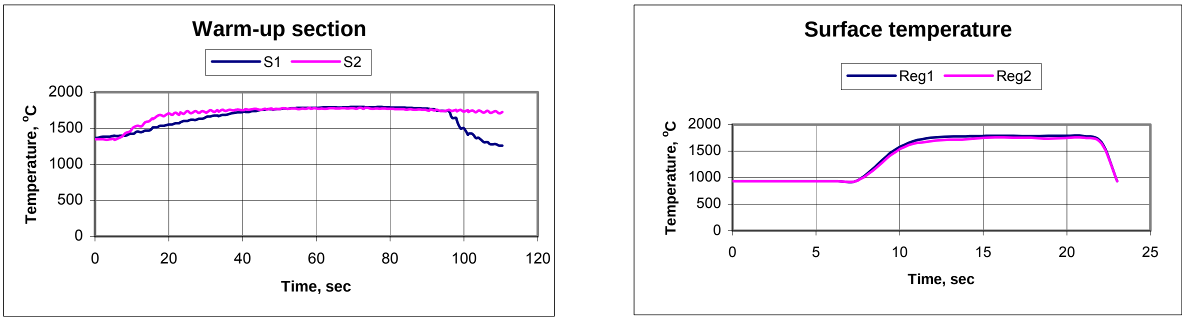

Temperature along the lines S1 and S2

Temperature at points Reg1 and Reg 2 versus time

Fig. 4.4-15: Surface temperature of the mock-up at a heat flux of $16\ MW/m^2$.

Fig. 4.4-16: Mock-up after the test.

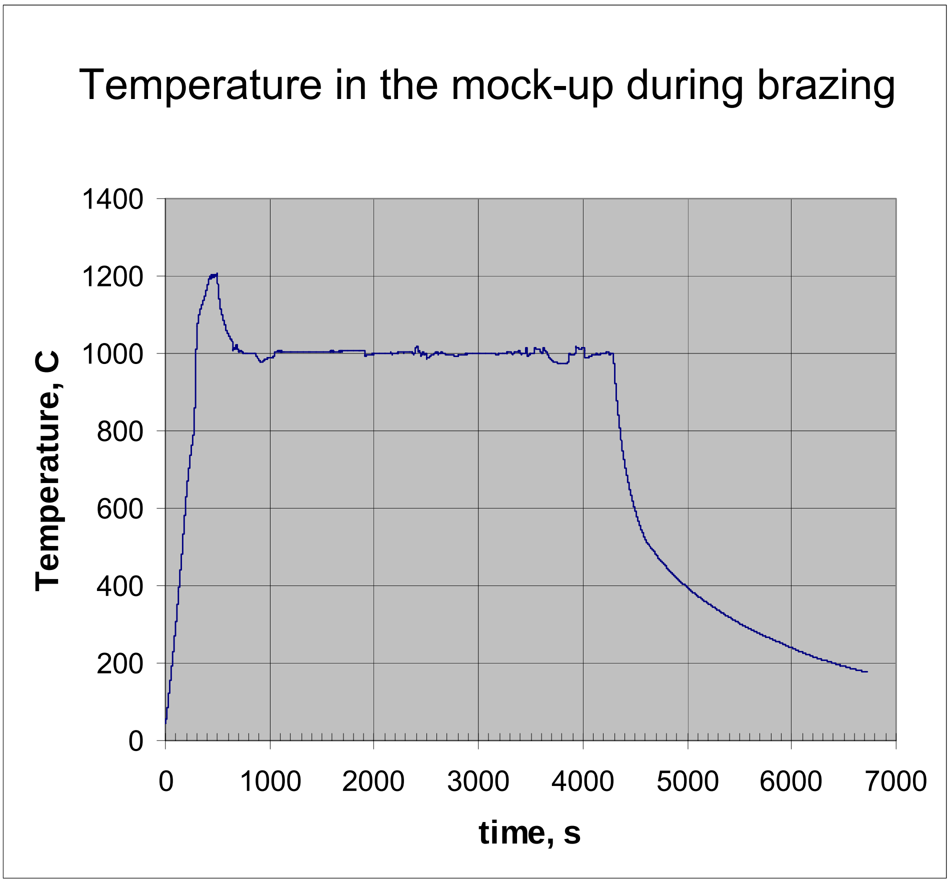

Fig. 4.4-17: Temperature in the mock-up during brazing with STEMET 1311 filler metal.

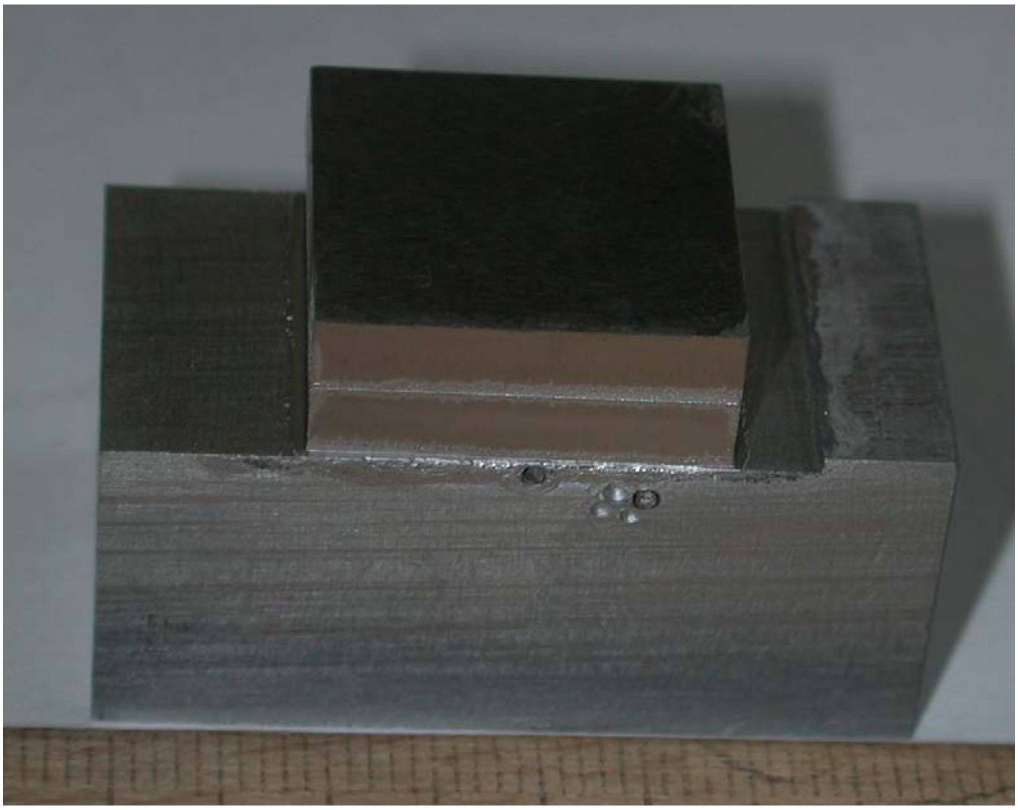

Fig. 4.4-18: Mock-up brazed with STEMET 1311 filler metal.

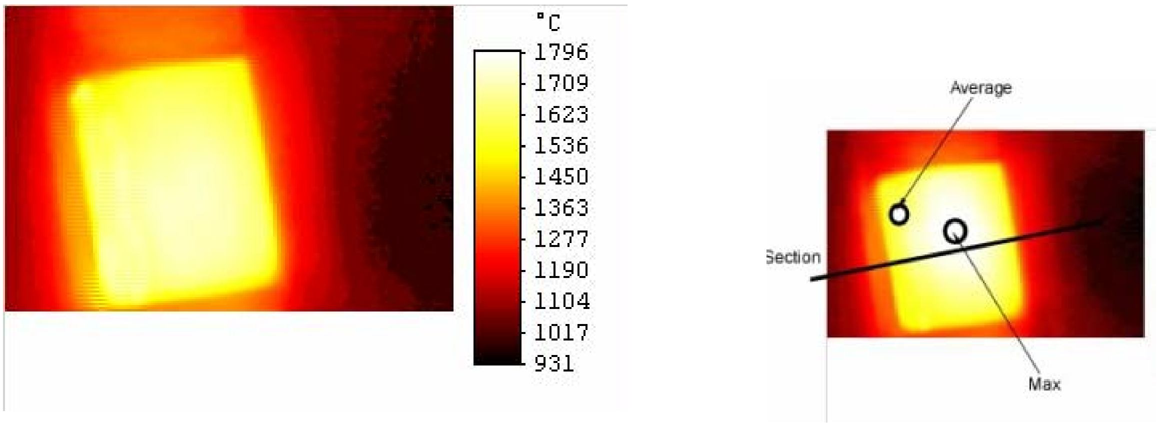

IR of the mock-up at 15 MW/m^2

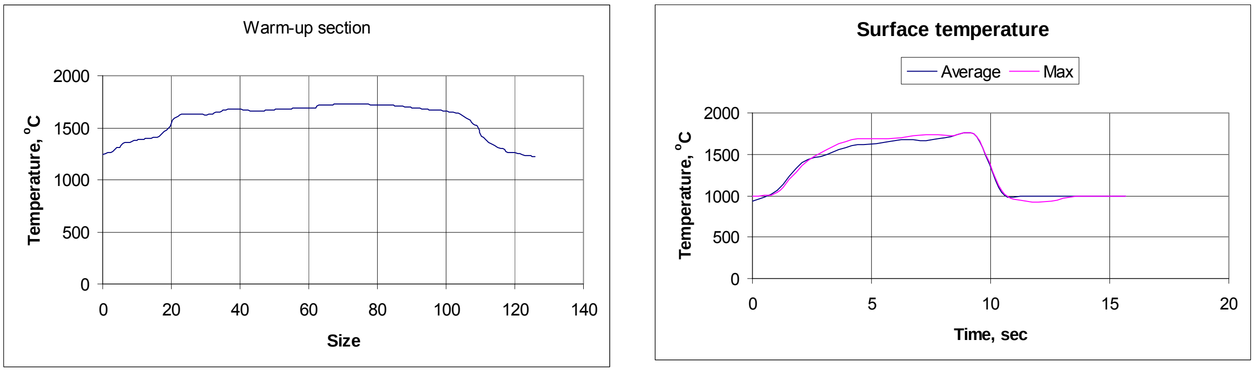

Temperature along line

Surface temperature of the mock-up versus time

Fig. 4.4-19: Surface temperature of the mock-up at a heat flux of 15 MW/m^2.

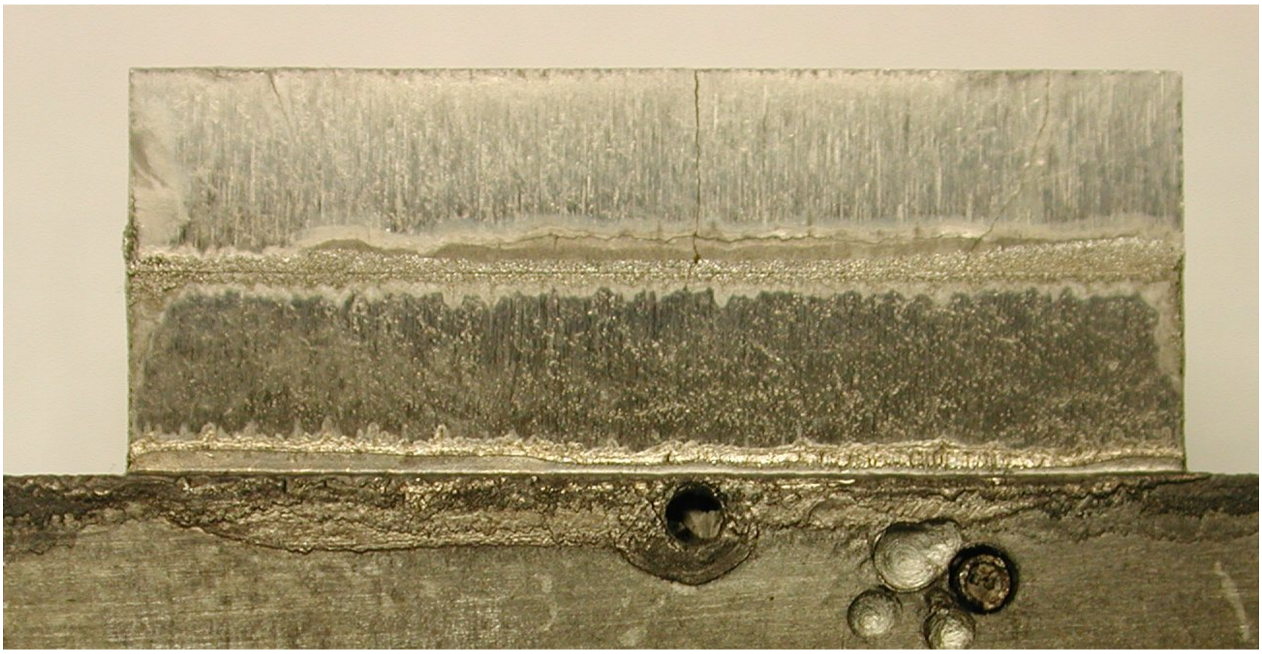

Fig. 4.4-20: Mock-up after the test.

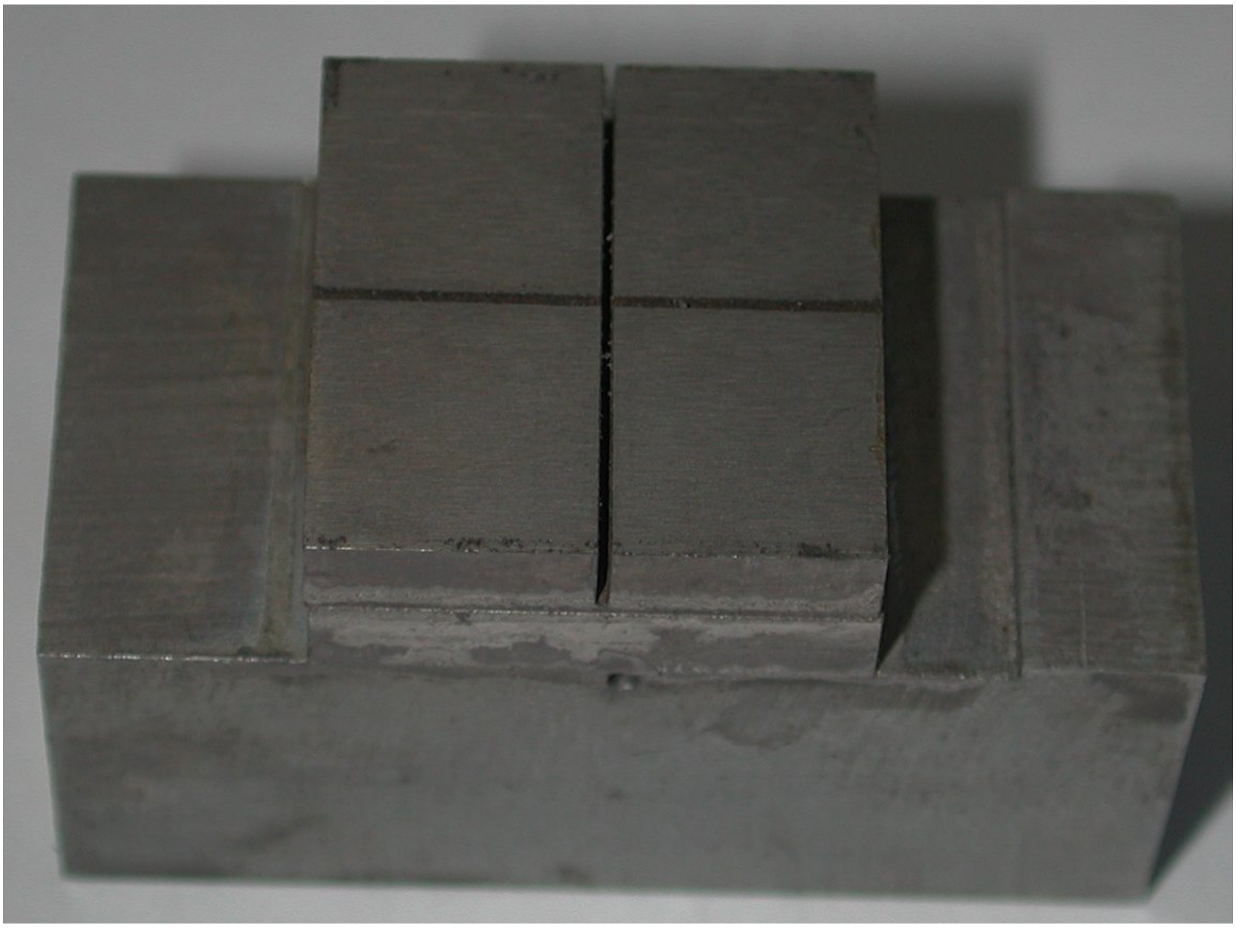

Fig. 4.4-21: Mock-up with castellation brazed with STEMET 1311 filler metal.

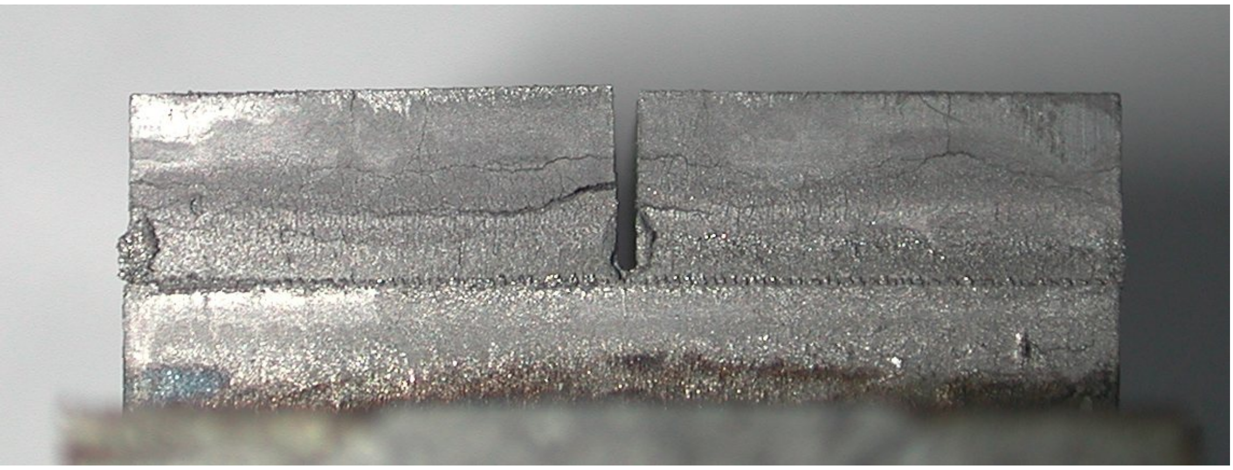

Fig. 4.4-22: Mock-up after the test.

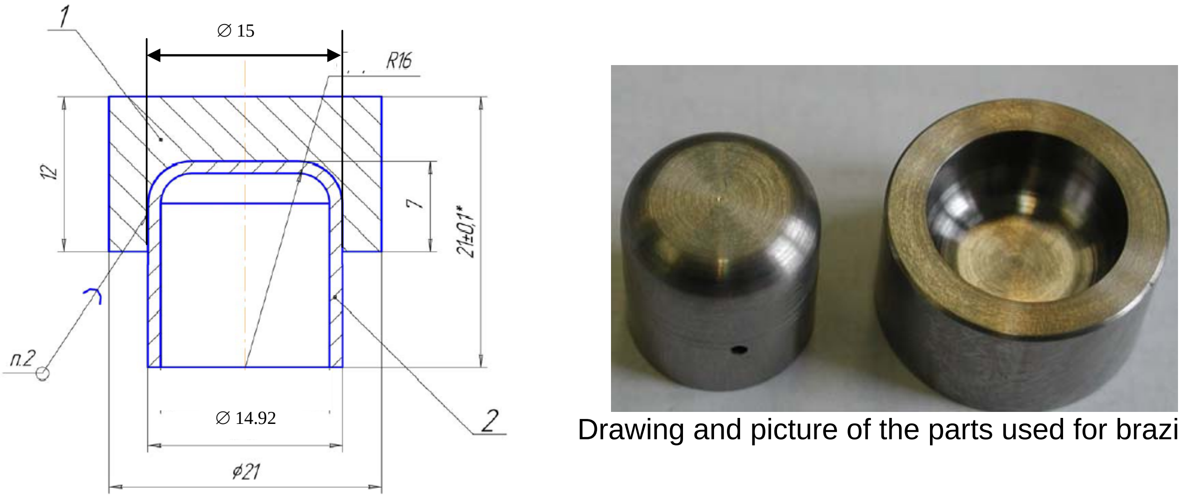

Drawing and picture of the parts used for brazing

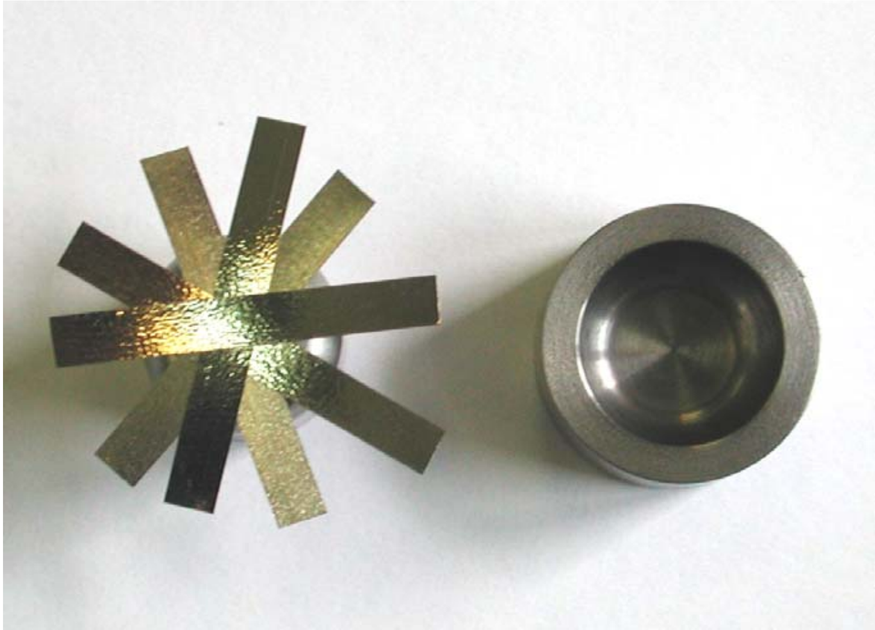

Brazing alloy insertion scheme

Jig used for brazing

Fig. 4.4-23: Brazing of the W real-geometry tile to the thimble.

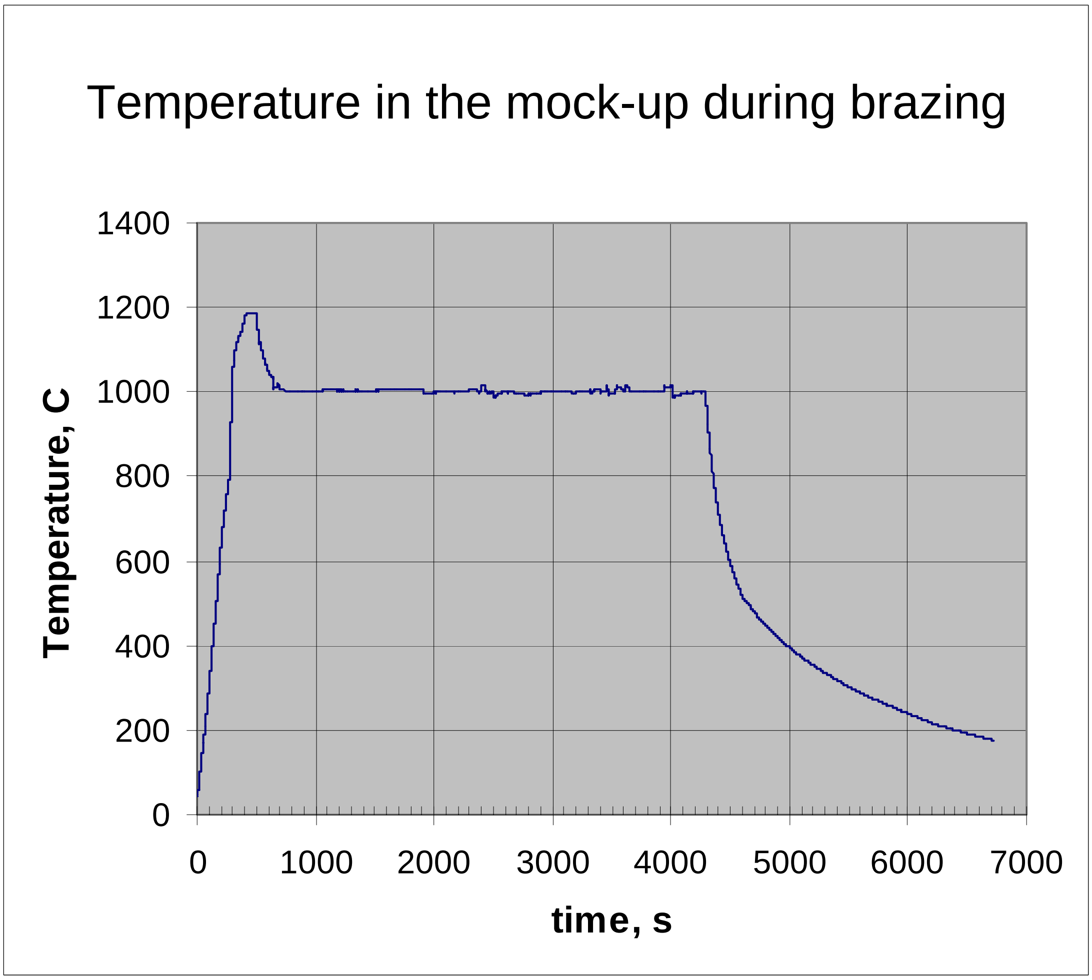

Fig. 4.4-24: Temperature in the mock-up during brazing with STEMET 1311 filler metal.

Fig. 4.4-25: Cross-section of the W/W joint with real geometry.

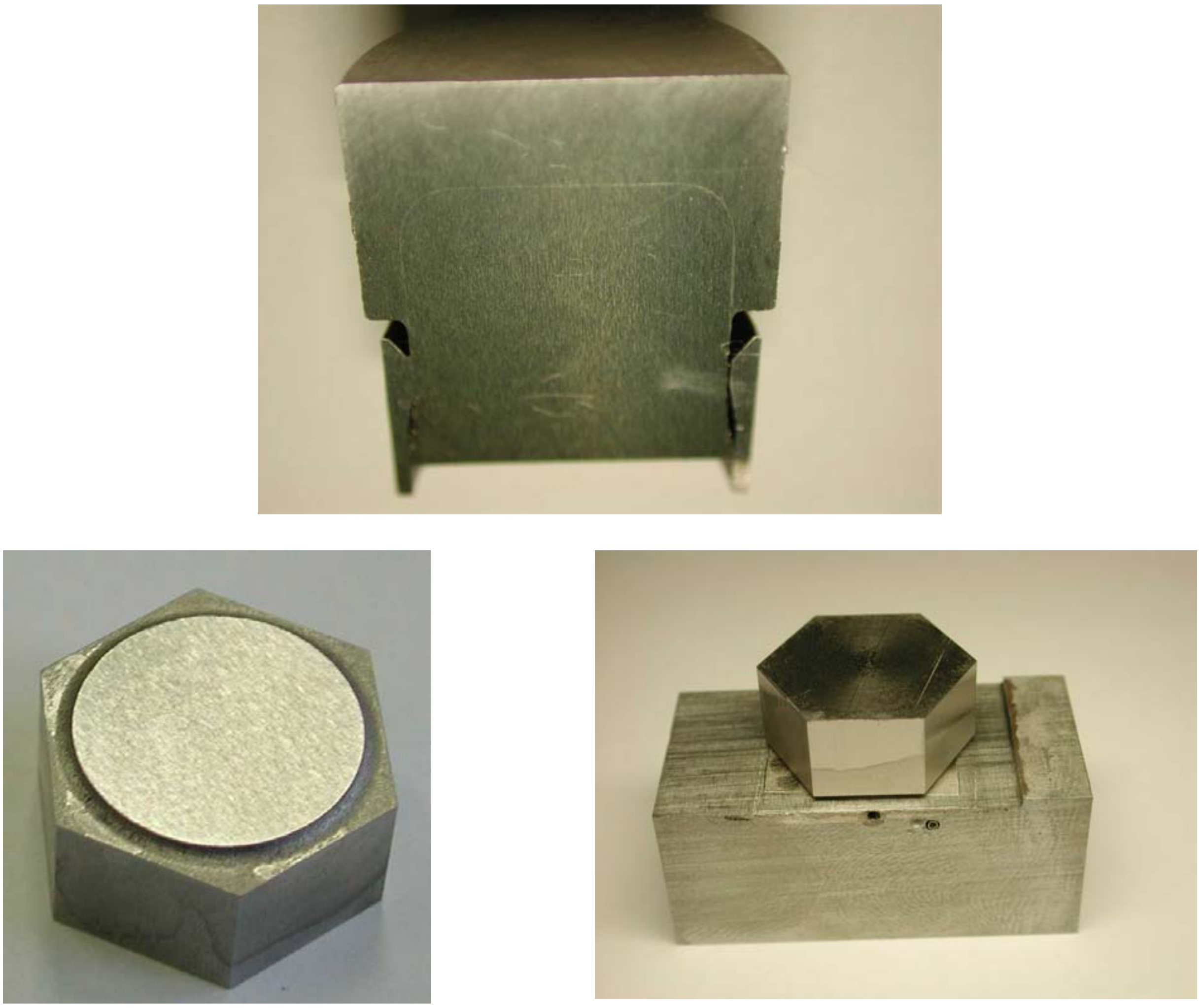

Fig. 4.4-26: Mock-up for HHF testing with curved bonding line after a successful brazing attempt.

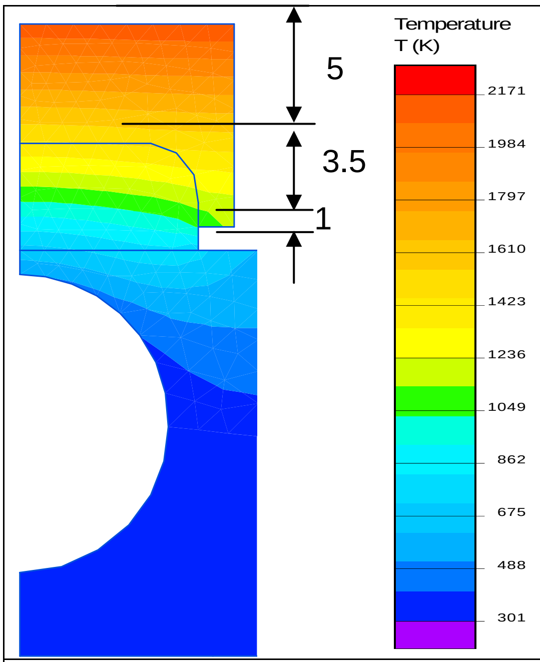	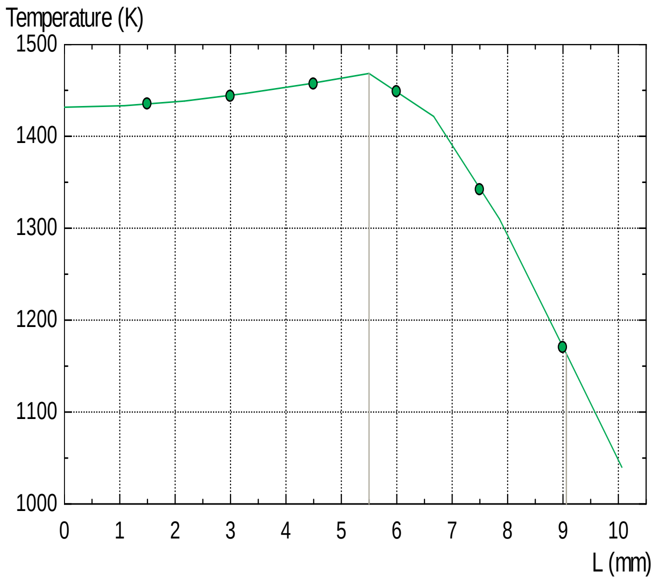
Temperature field in the mock-up at 15 MW/m^2	Temperature along W/W bond line

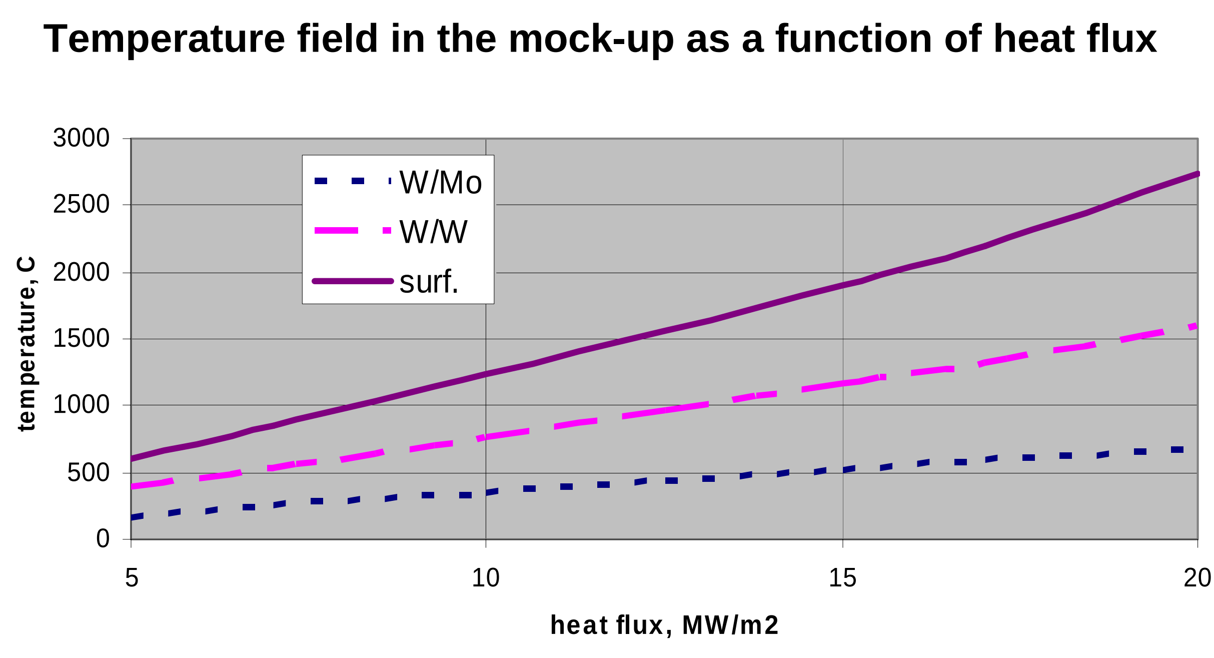

Fig. 4.4-27: FE analysis of temperature fields in the mock up with a curved bonding line.

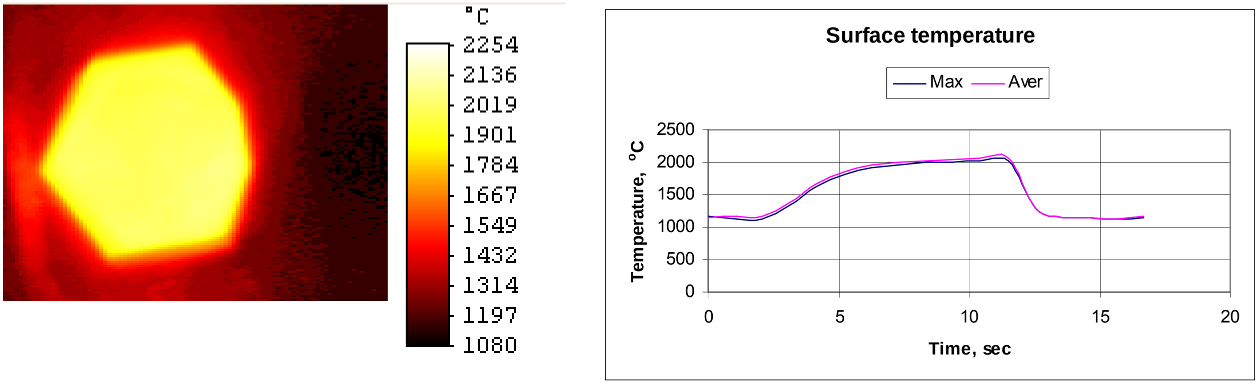

IRTV of the mock-up surface during the first cycle at 15 MW/m^2

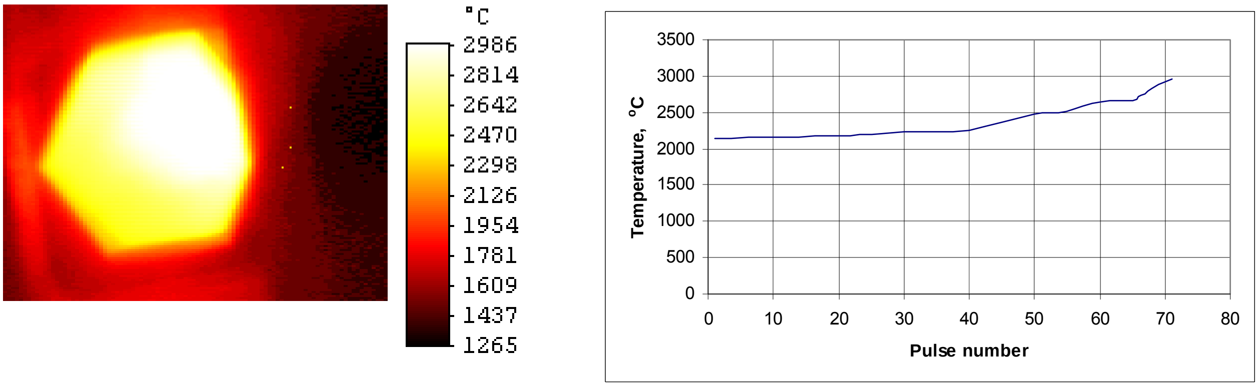

IRTV of the mock-up surface during the 70th cycle at 15 MW/m^2 and surface temperature history as a function of the cycle number

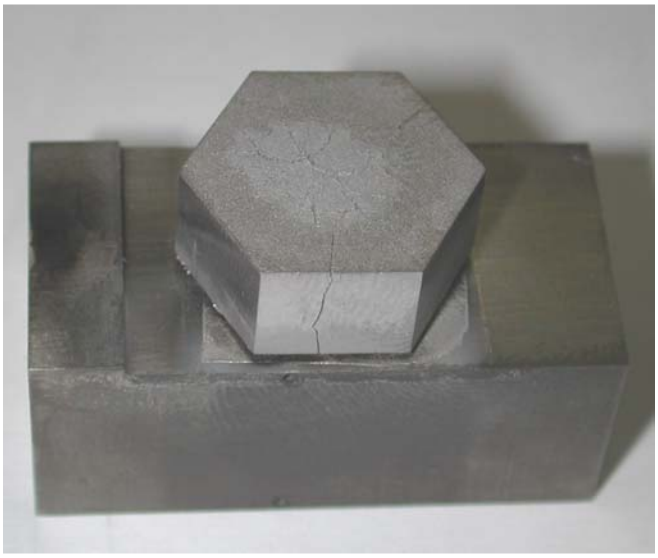

Mock-up after HHF tests

Fig. 4.4-28: HHF testing of the mock-up with the curved bonding line.

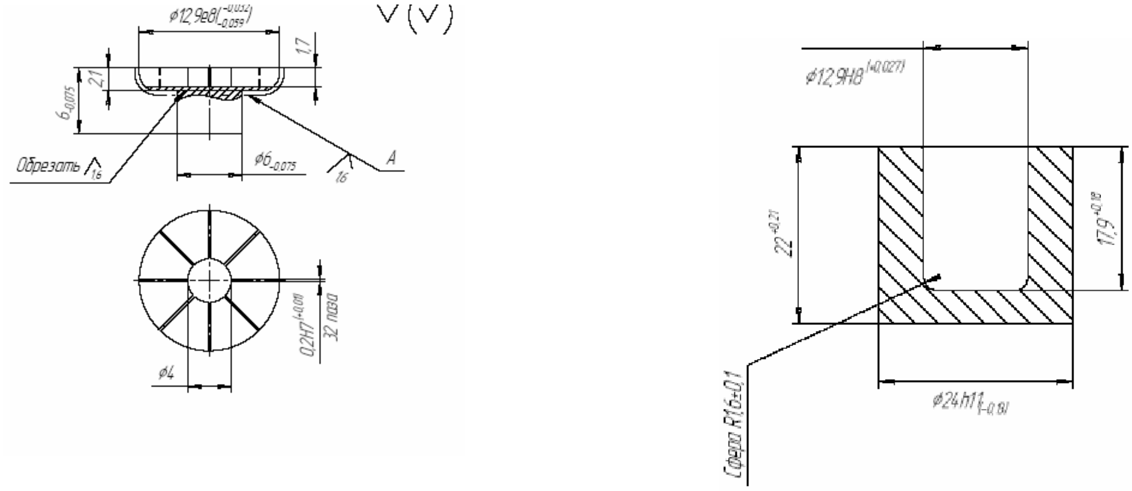

W slot array, 24 slots 0.3 mm width

WL10 thimble

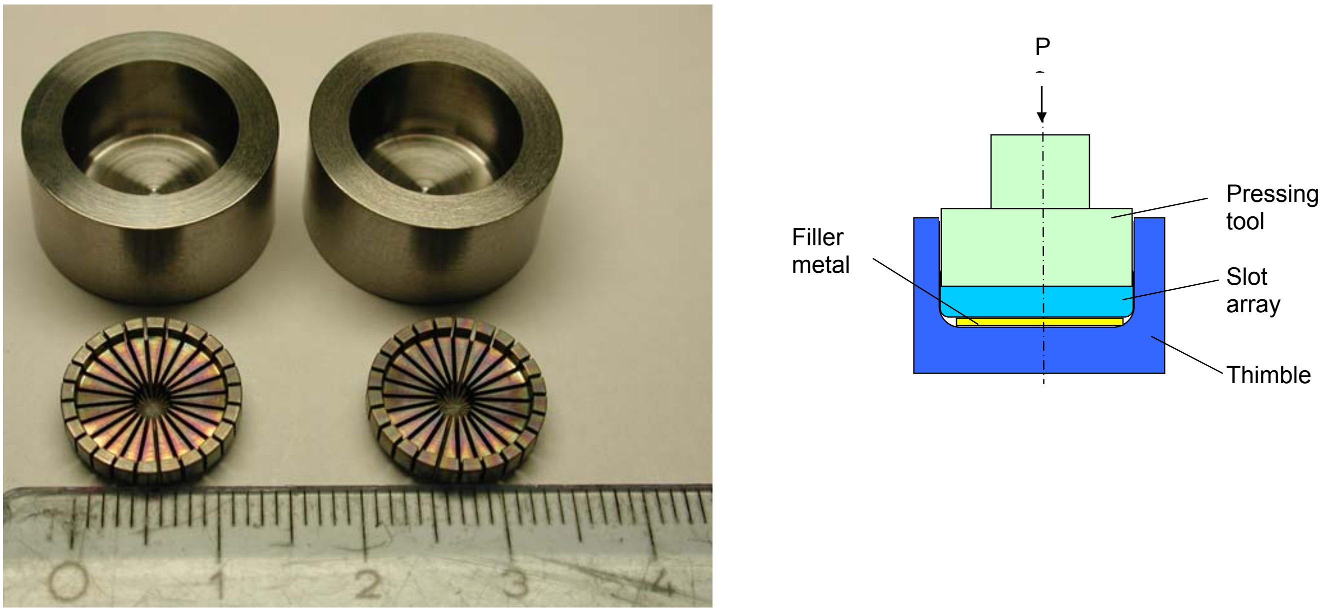

Mock-ups

Scheme of brazing

Fig. 4.4-29: Brazing of the W slot array to the W thimble.

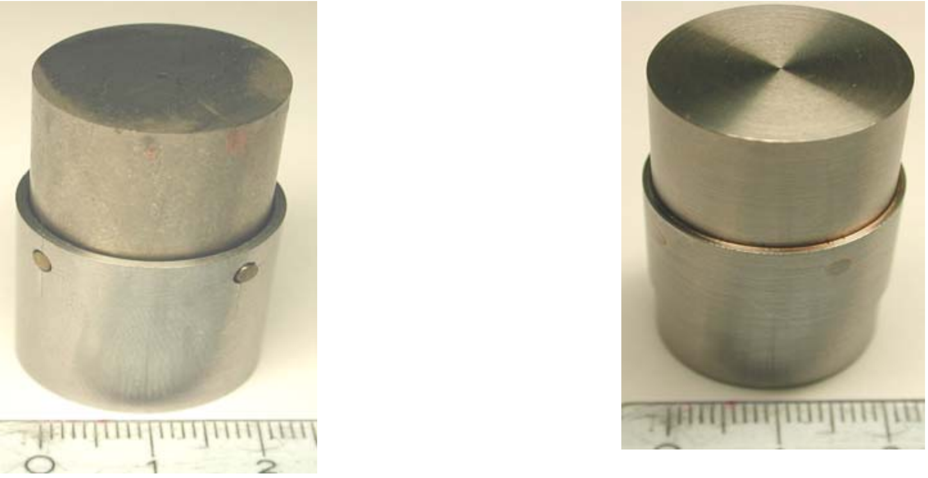

Assembly before (left) and after casting (right)

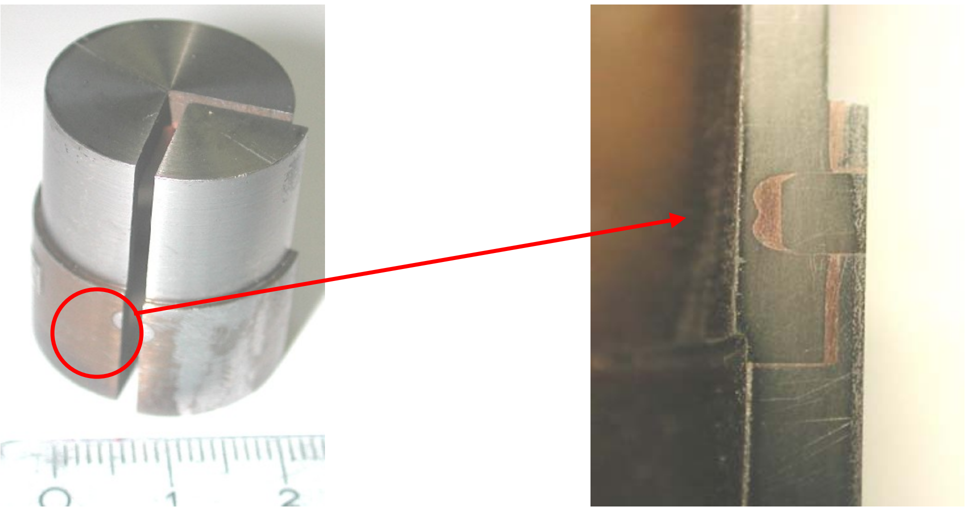

Cross-section of the lock area

Fig. 4.5-1: W-steel joint with pin-type locking.

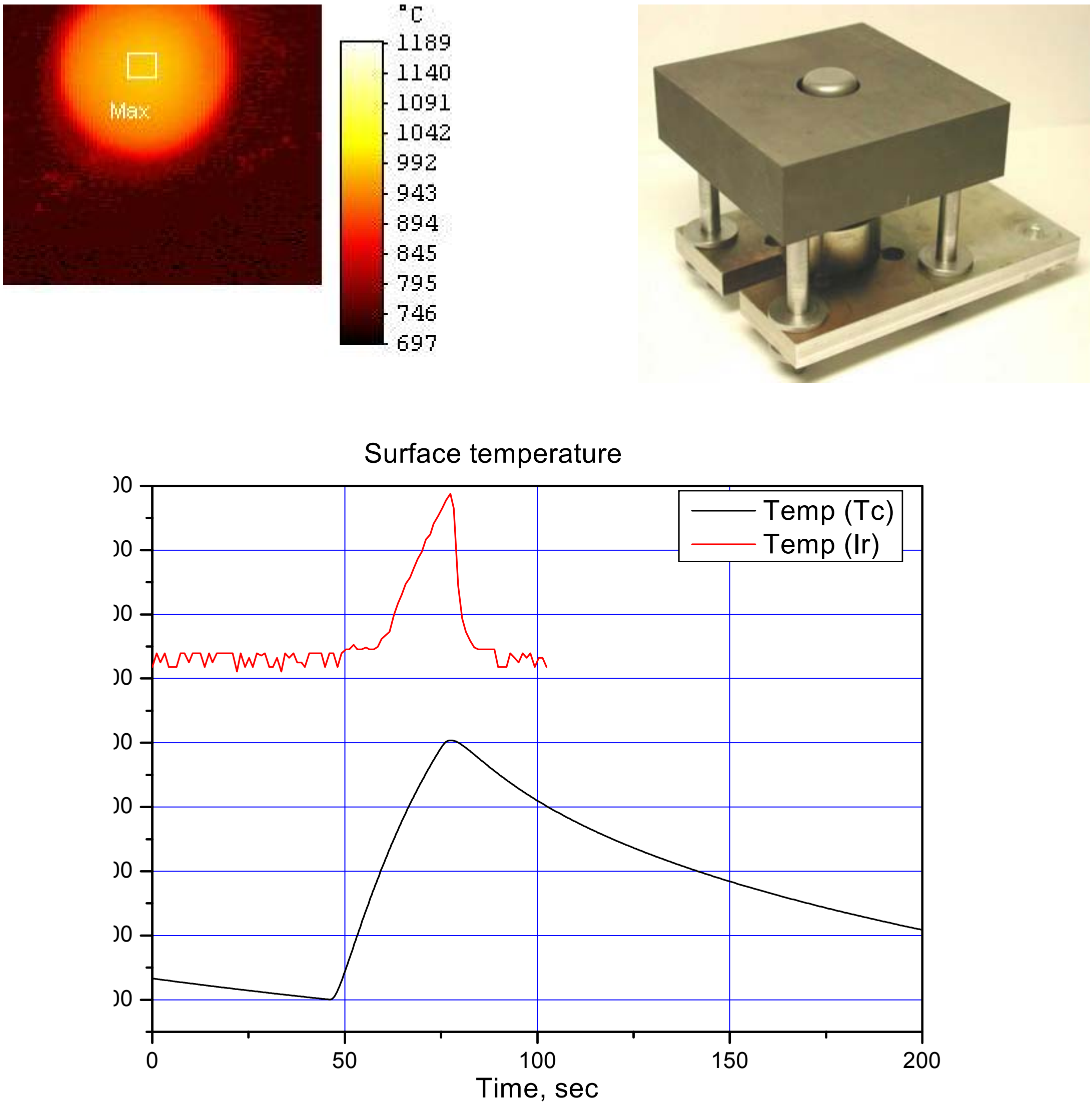

Fig. 4.5-2: Thermocycling experiment on a finger.

Fig. 4.5-3: Main elements for the W-steel joint with a new (conic) lock.

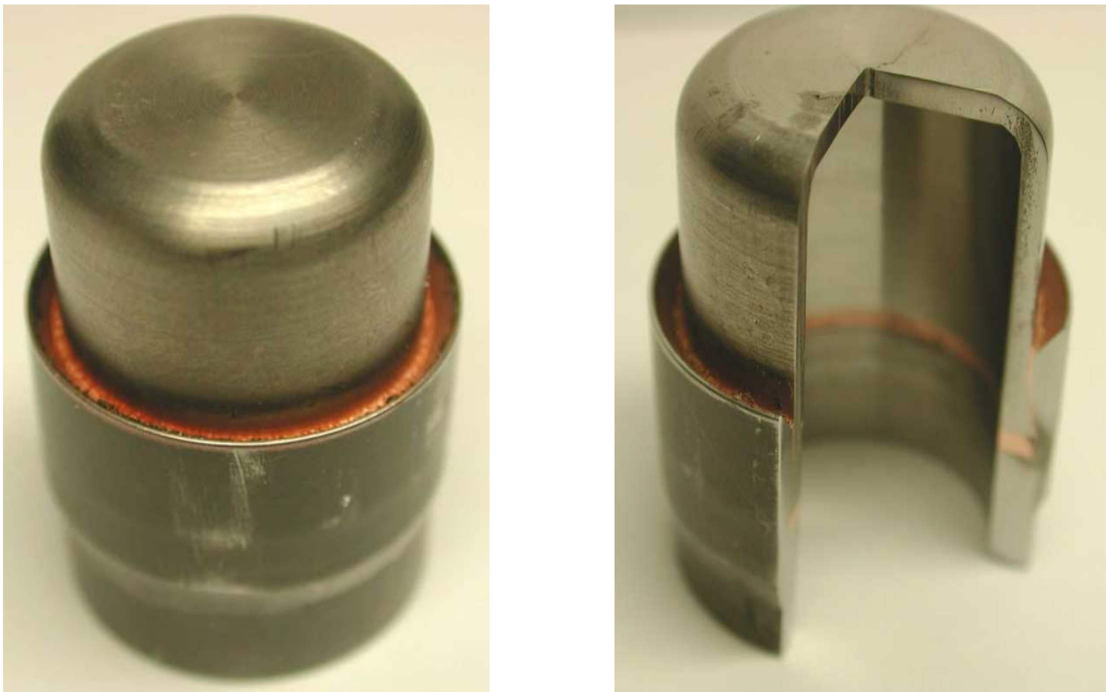

Fig. 4.5-4: Finger mock-up (without armour tile) after casting (left) and after post-testing examination (right).

Fig. 4.5-5: Cracking of the WL-10 thimble after thermocycling.

Fig. 4.5-6: Mock-up with a W-Cu thimble.

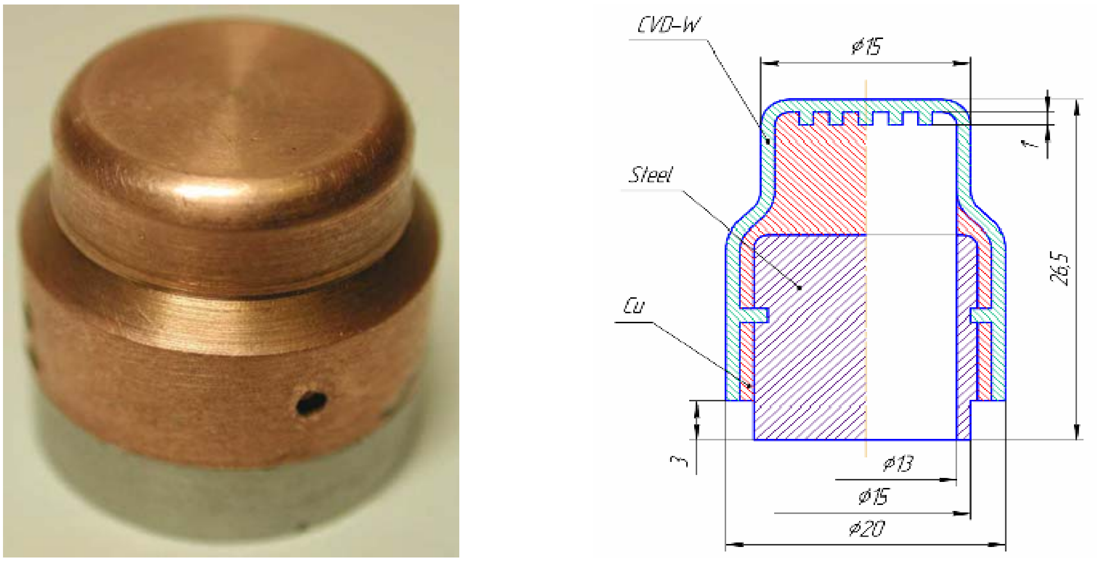

Fig. 4.5-7: Mock-up with CVD tungsten (Cu-steel structure before W-coating deposition).

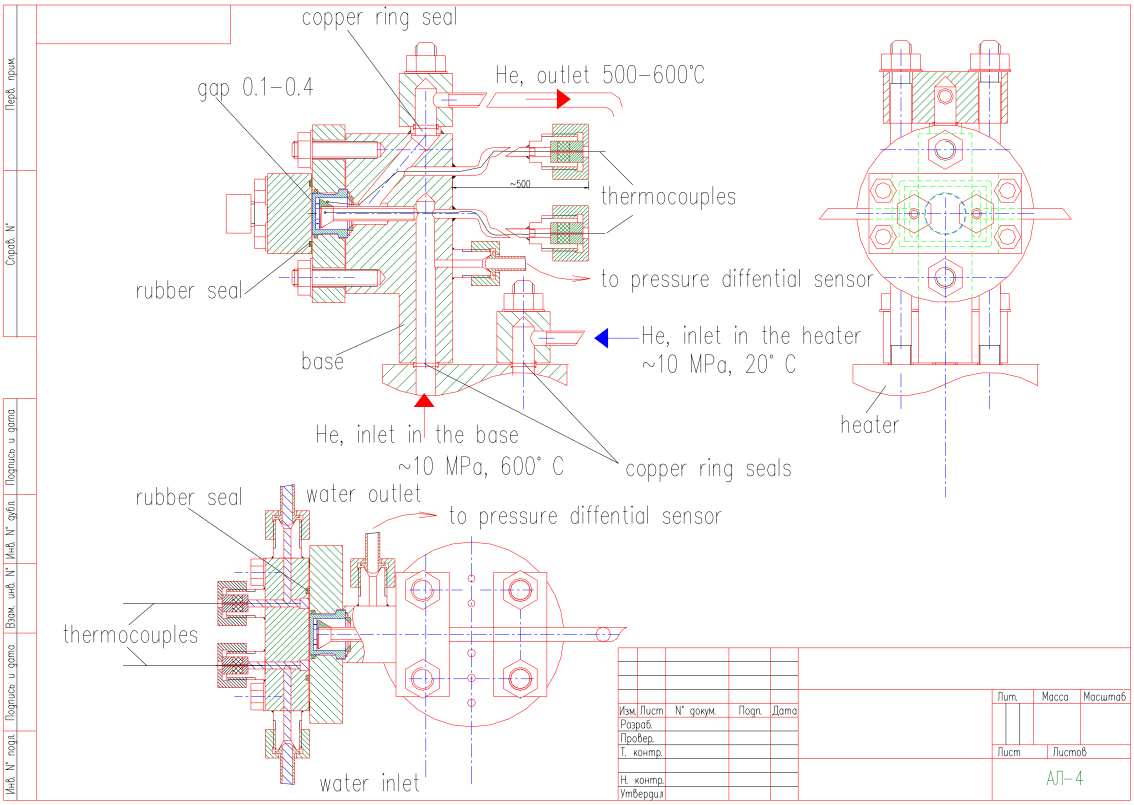

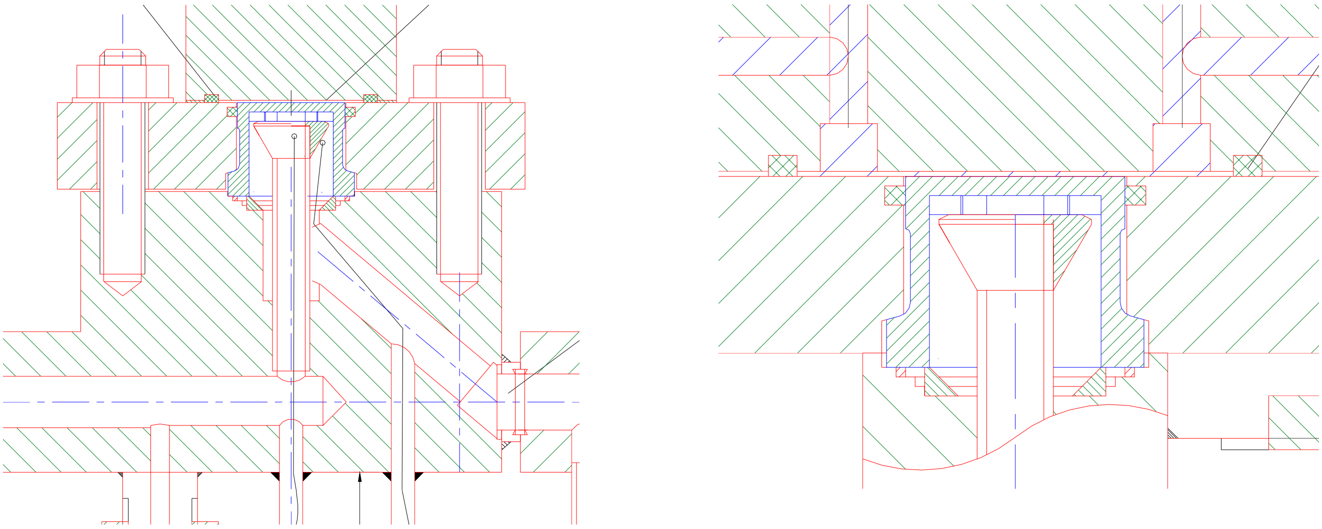

Details: section across (left) and along (right) water flow

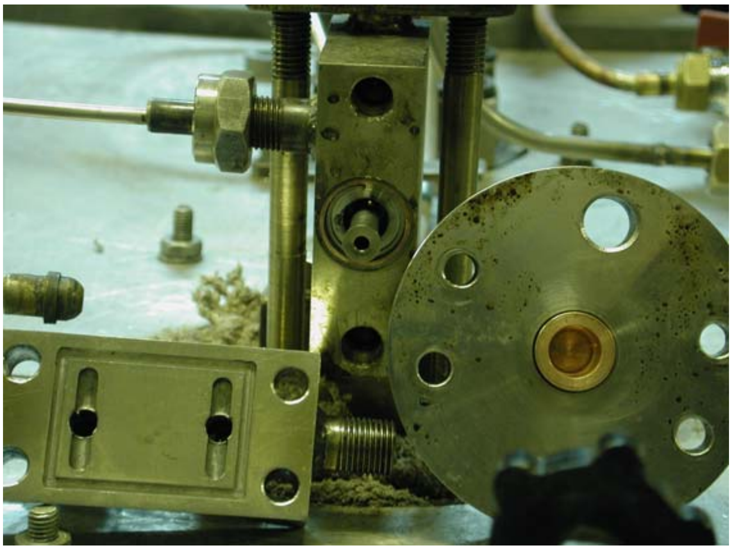

Mock-up unit with helium-to-water interaction area

Fig. 5-1: GPF2 mock-up assembly.

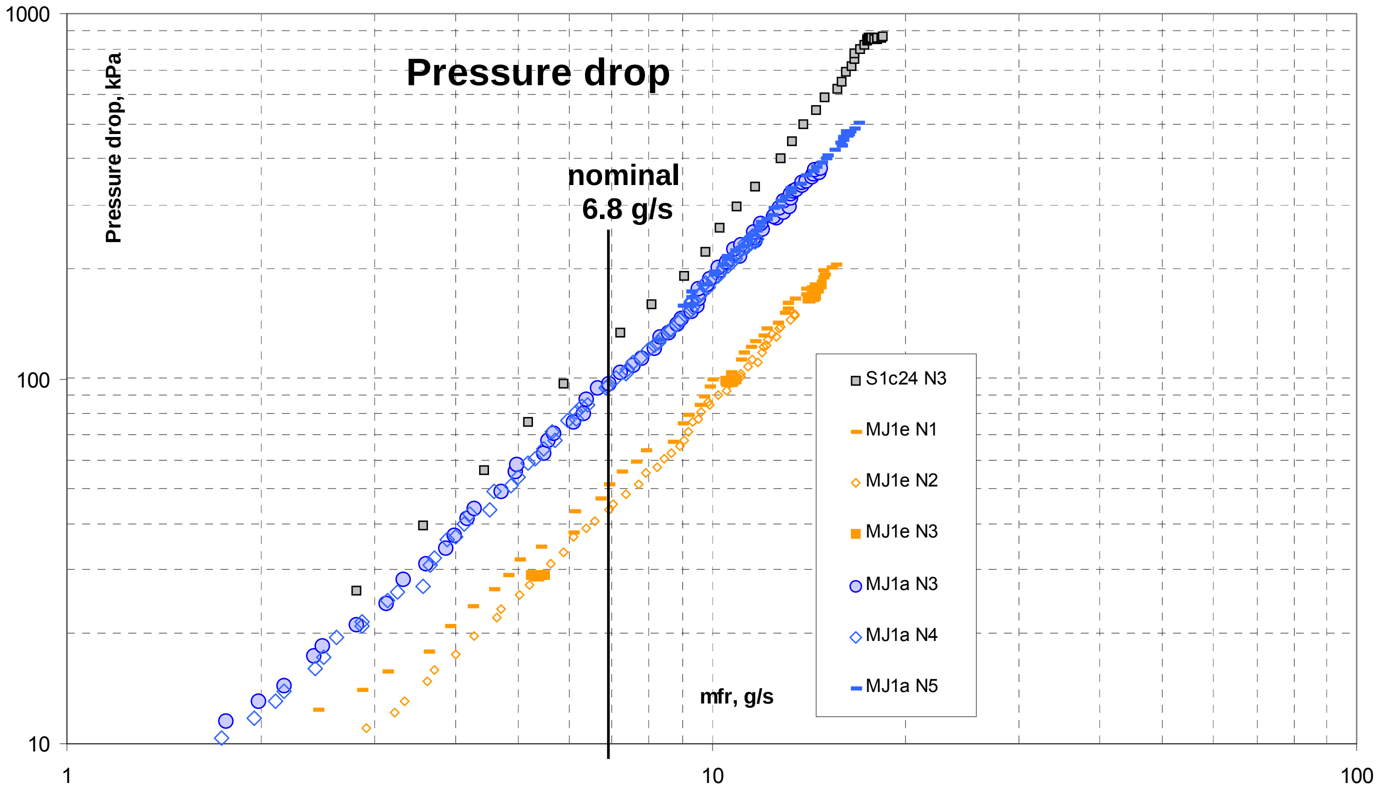

Fig. 5-2: Pressure losses measured in GPF2 for different HEMJ and one slot design variants.

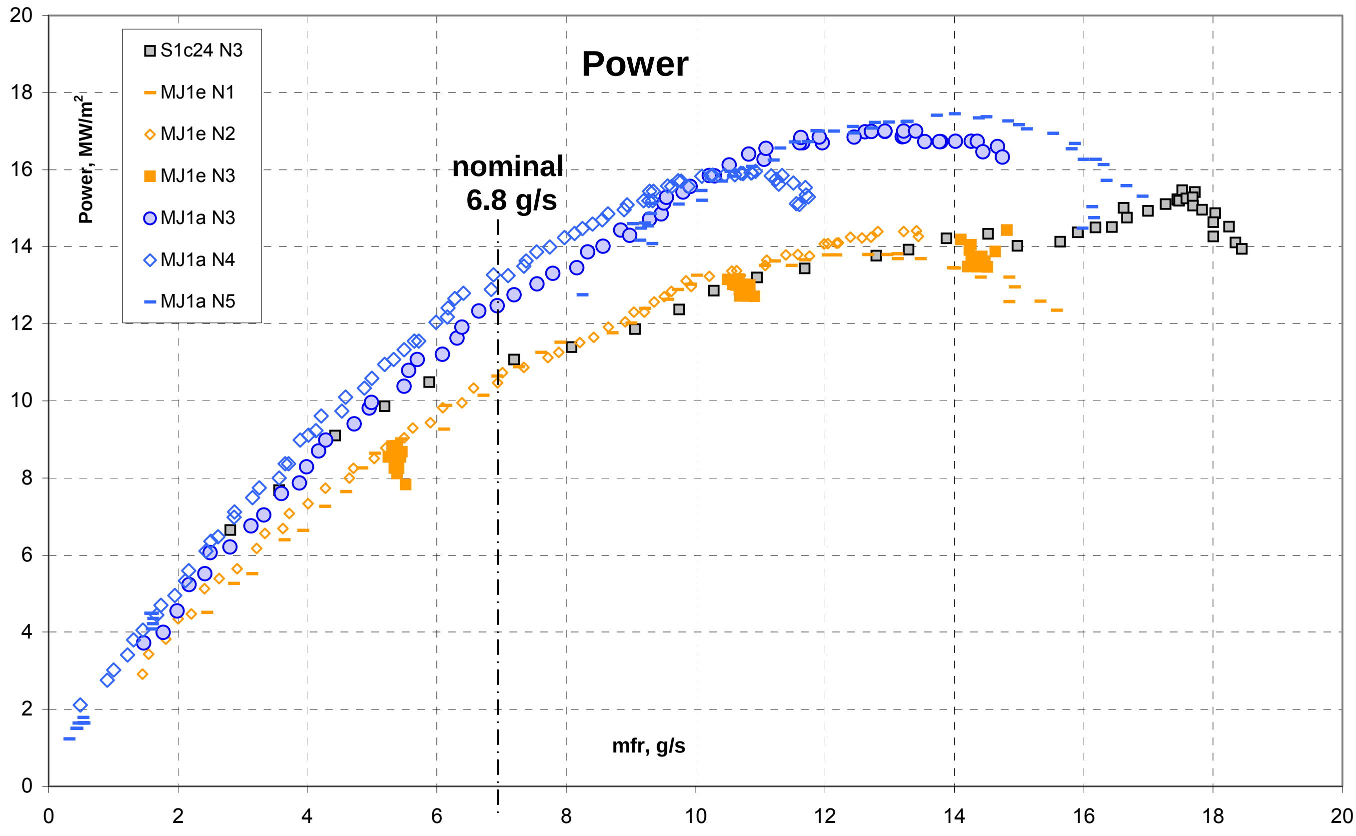

Fig. 5-3: Divertor performance derived from GPF2 measurements for different HEMJ and one slot design variants.

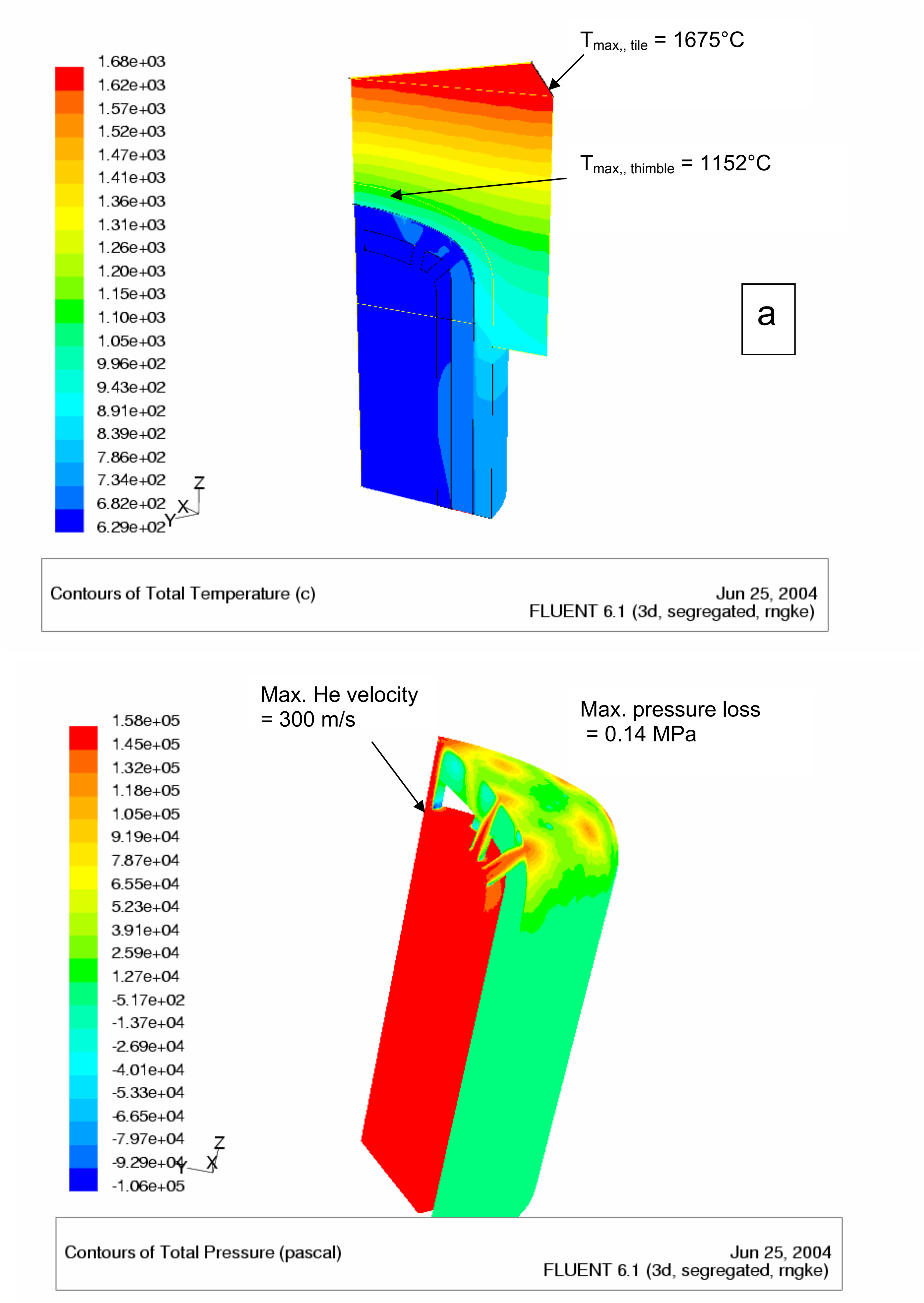

$T_{max,, tile}$ = 1675°C

$T_{max,, thimble}$ = 1152°C

Contours of Total Temperature (c)

Jun 25, 2004
FLUENT 6.1 (3d, segregated, rngke)

Max. He velocity
= 300 m/s

Max. pressure loss
= 0.14 MPa

Contours of Total Pressure (pascal)

Jun 25, 2004
FLUENT 6.1 (3d, segregated, rngke)

Fig. 6.1-1: Temperature distribution and total pressure distribution in geometry J1a. Results obtained with FLUENT.

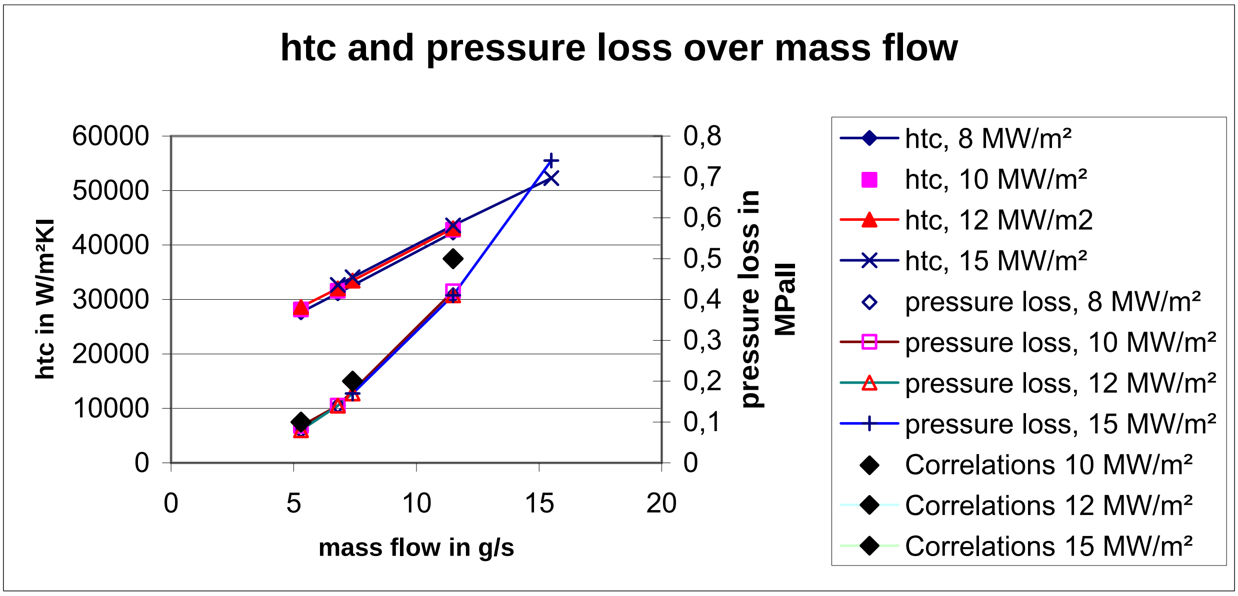

Fig. 6.1-2: htc and pressure loss versus mass flow for geometry J1a. Results obtained with FLUENT.

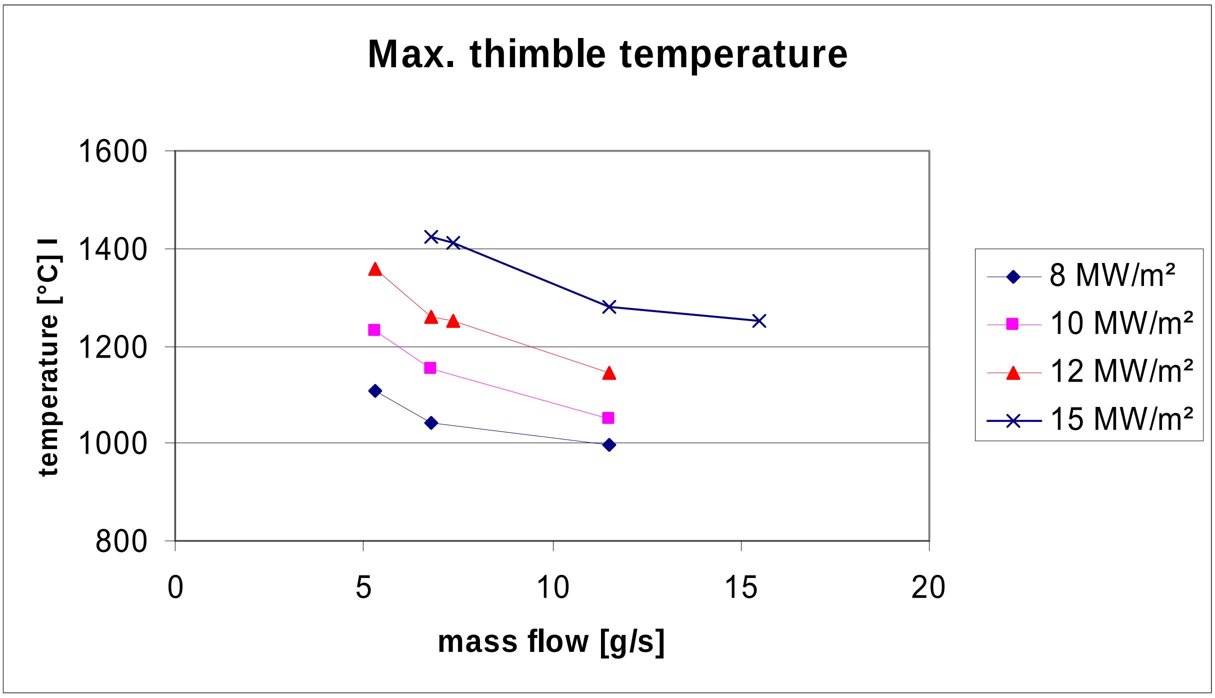

Fig. 6.1-3: Max. temperature of the thimble for different mass flows and heat loads. Results obtained with FLUENT.

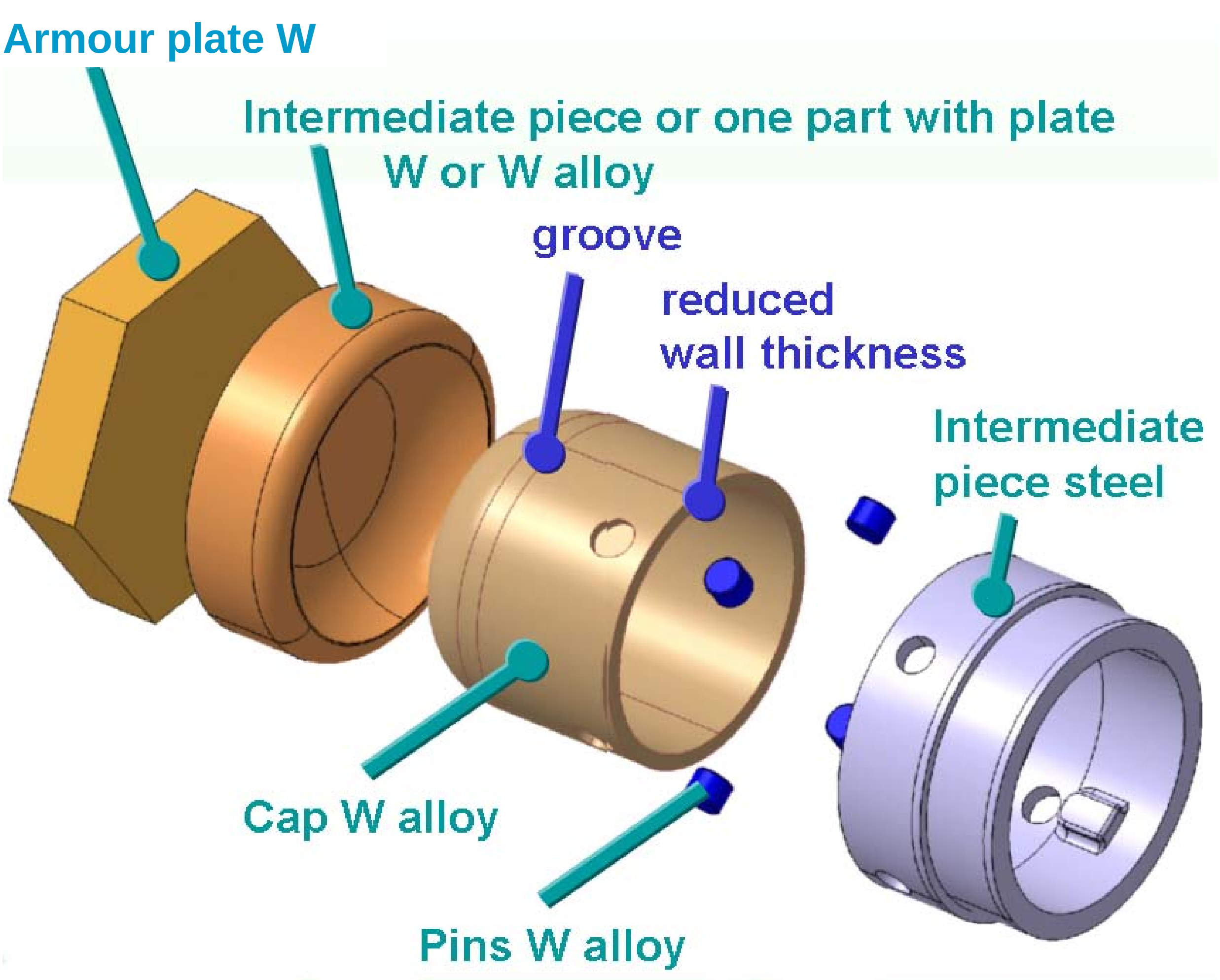

Fig. 6.2.1-1: Parts and sections of the thermal stress-reduced cooling finger (HEMJ).

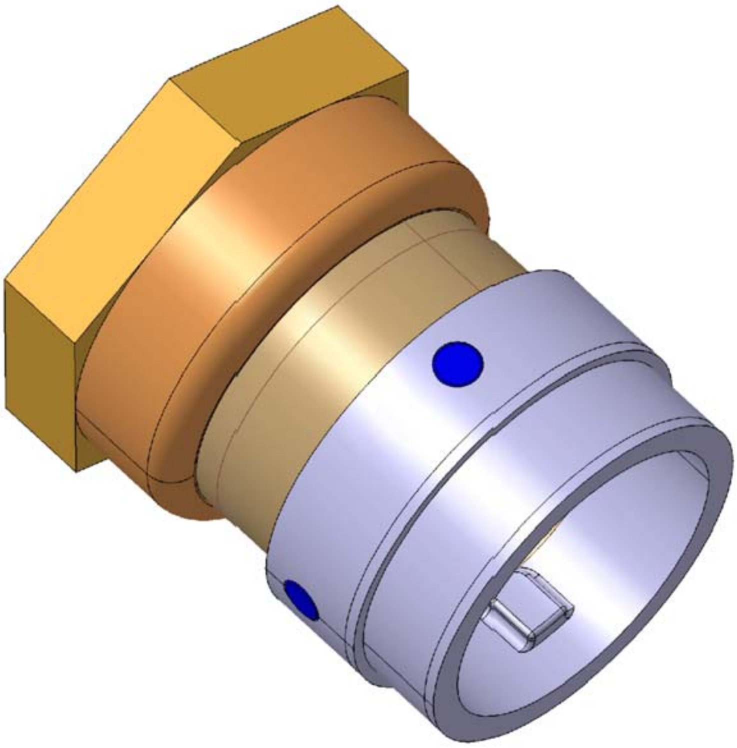

Fig. 6.2.1-2: Stress-reduced cooling finger (HEMJ).

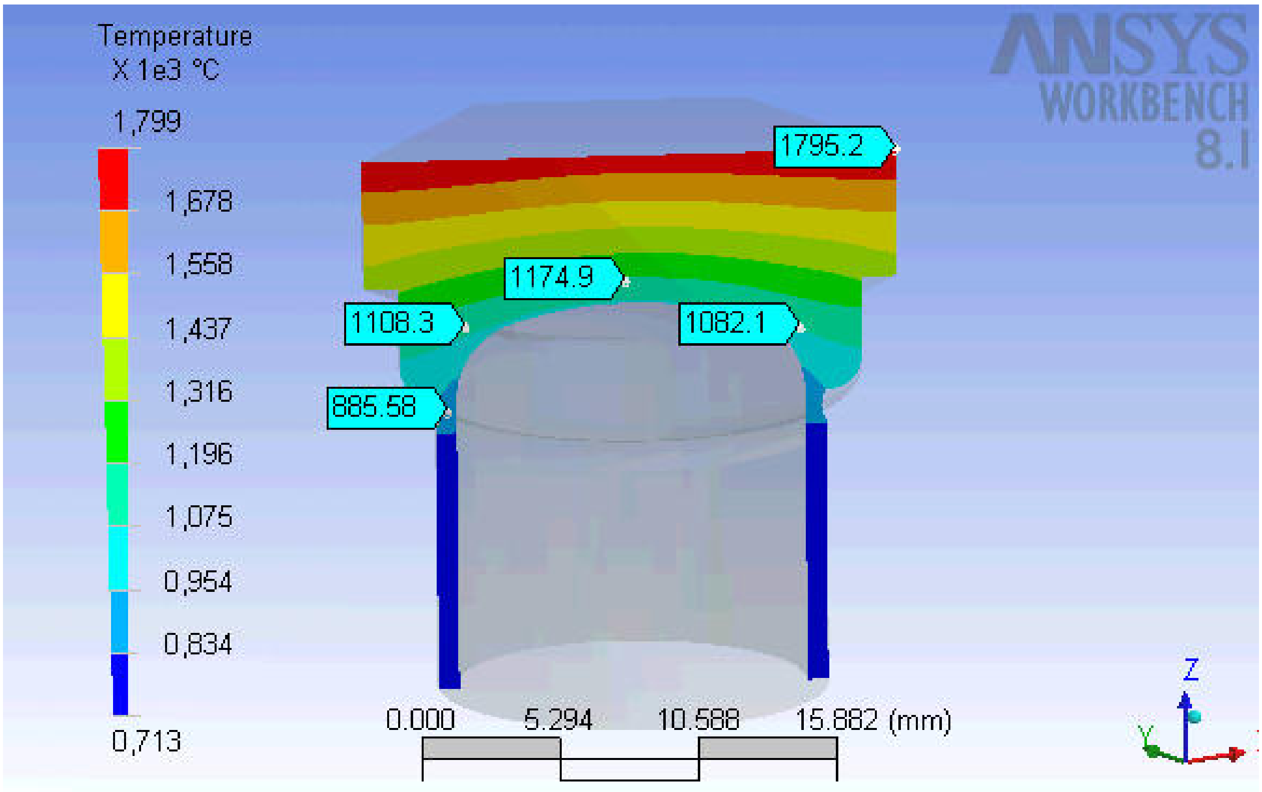

Fig. 6.2.1-3: Temperature distribution of HEMJ, J1a, 6.8 g/s, 10 MW/m².

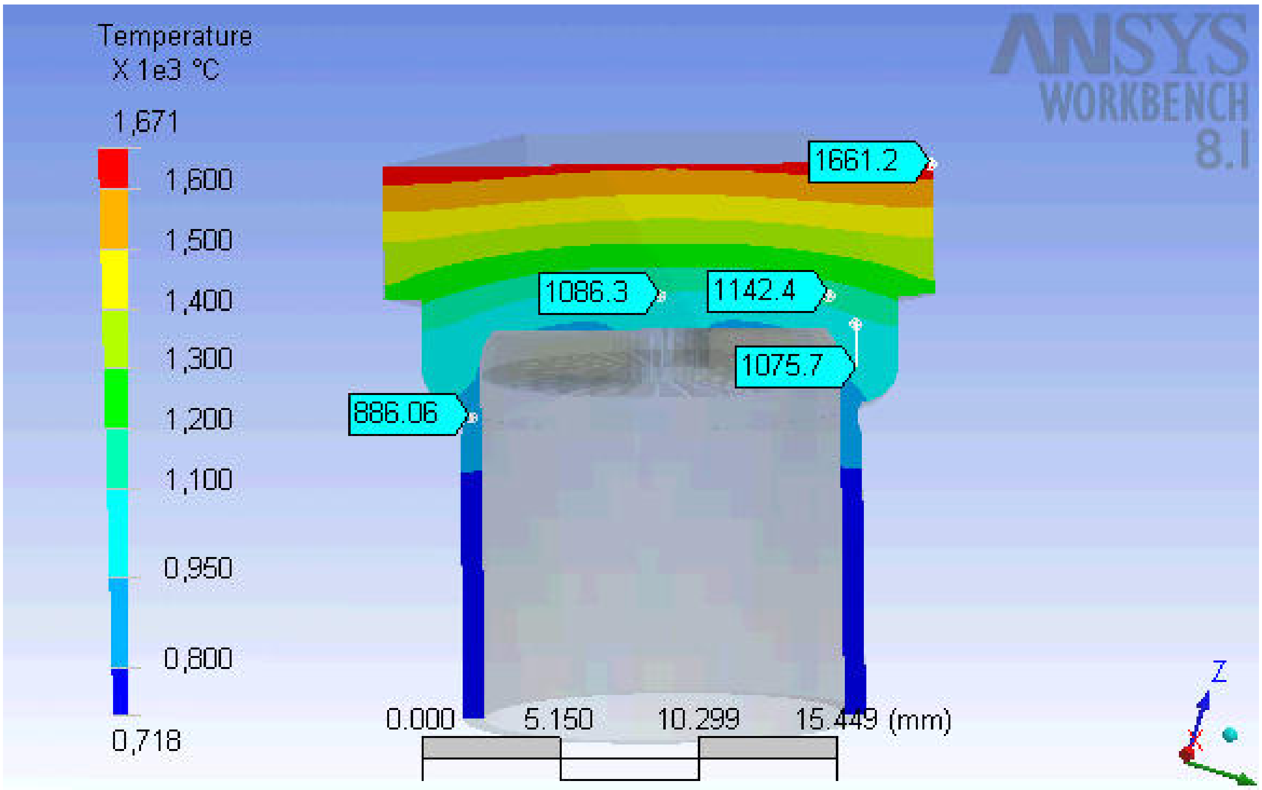

Fig. 6.2.1-4: Temperature distribution of HEMS, S1c, 6.8 g/s, 10 MW/m².

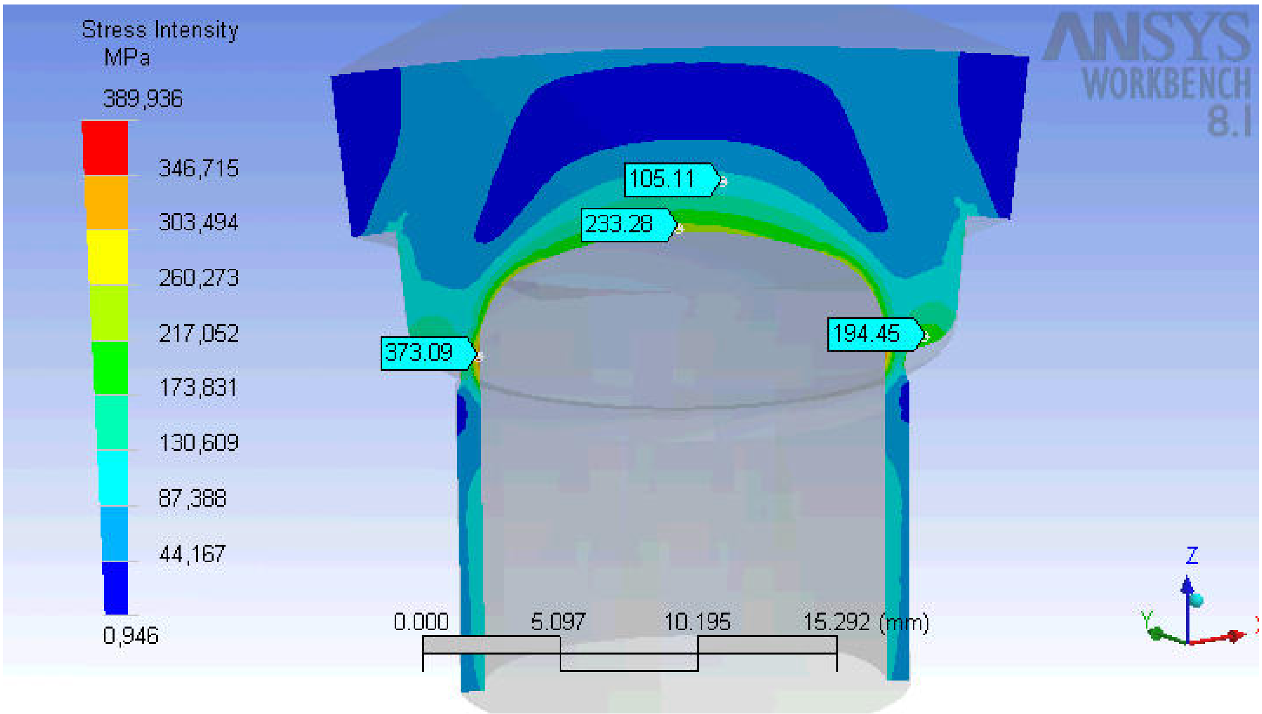

Fig. 6.2.1-5: Stress distribution of HEMJ, J1a, 6.8 g/s, 10 MW/m².

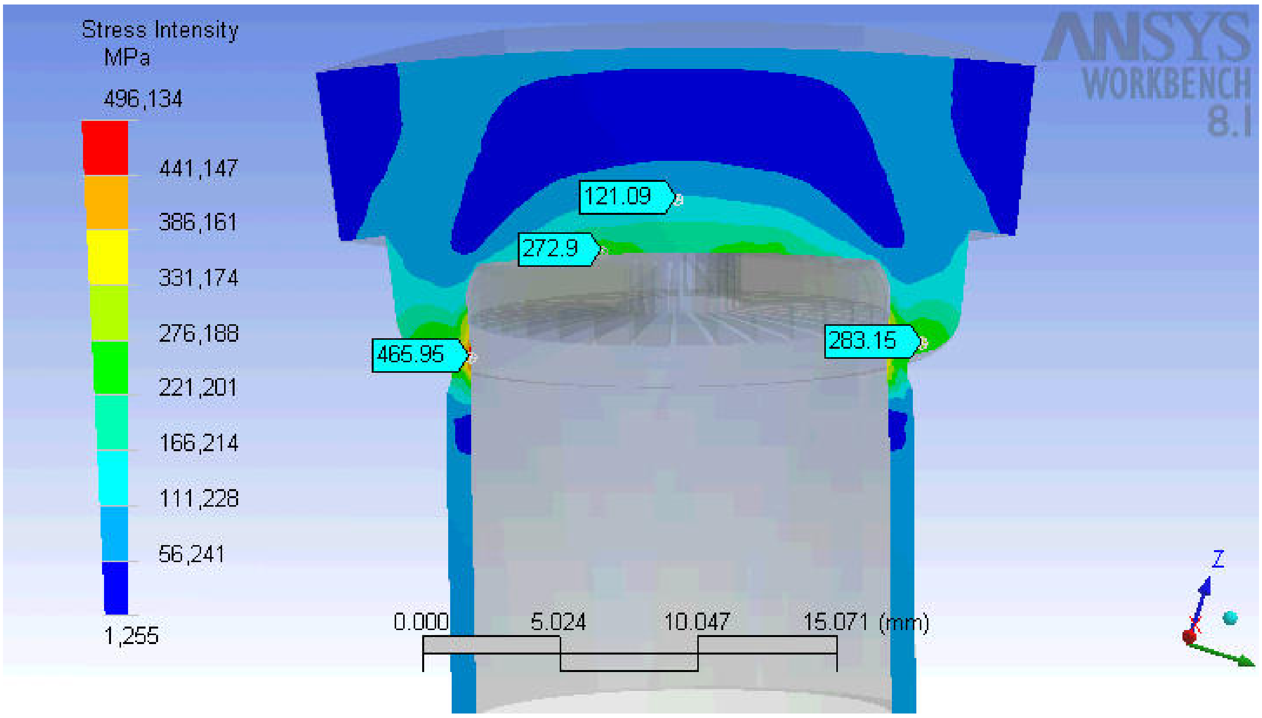

Fig. 6.2.1-6: Stress distribution of HEMS, S1c, 6.8 g/s, 10 MW/m².

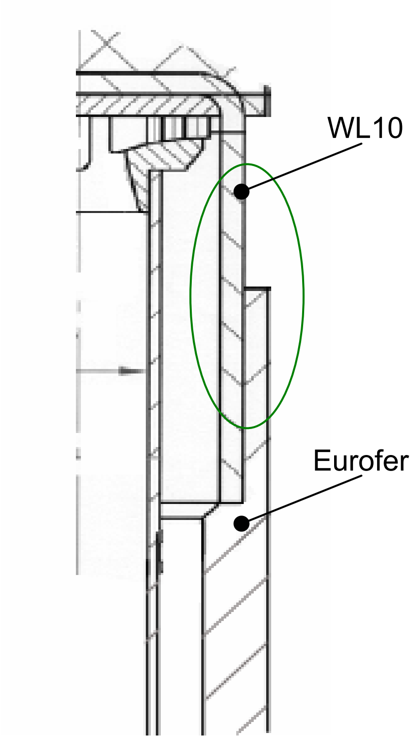

Fig. 6.2.2-1: Transition zone.

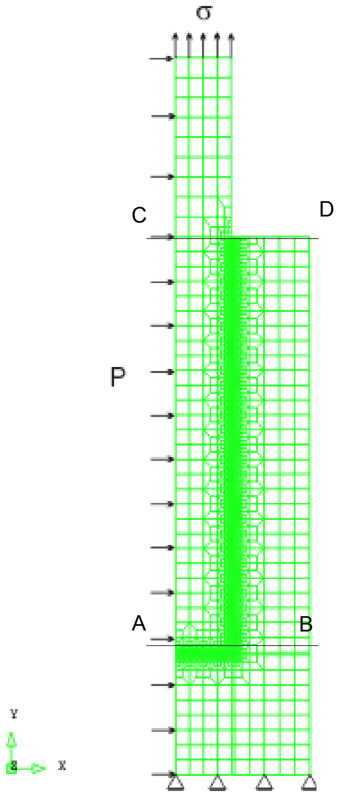

Fig. 6.2.2-2 Model discretisation.

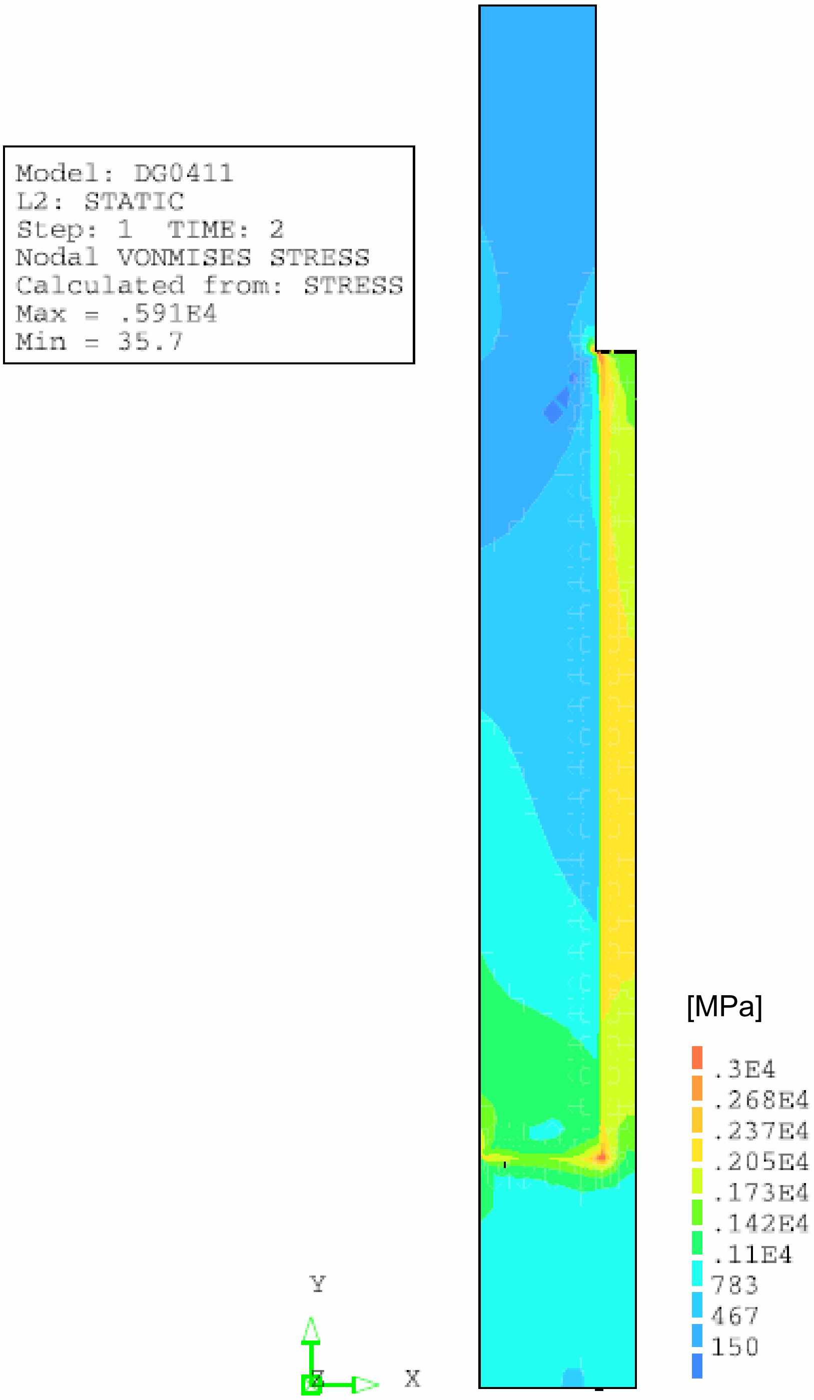

Fig. 6.2.2-3: Von Mises stress distribution.

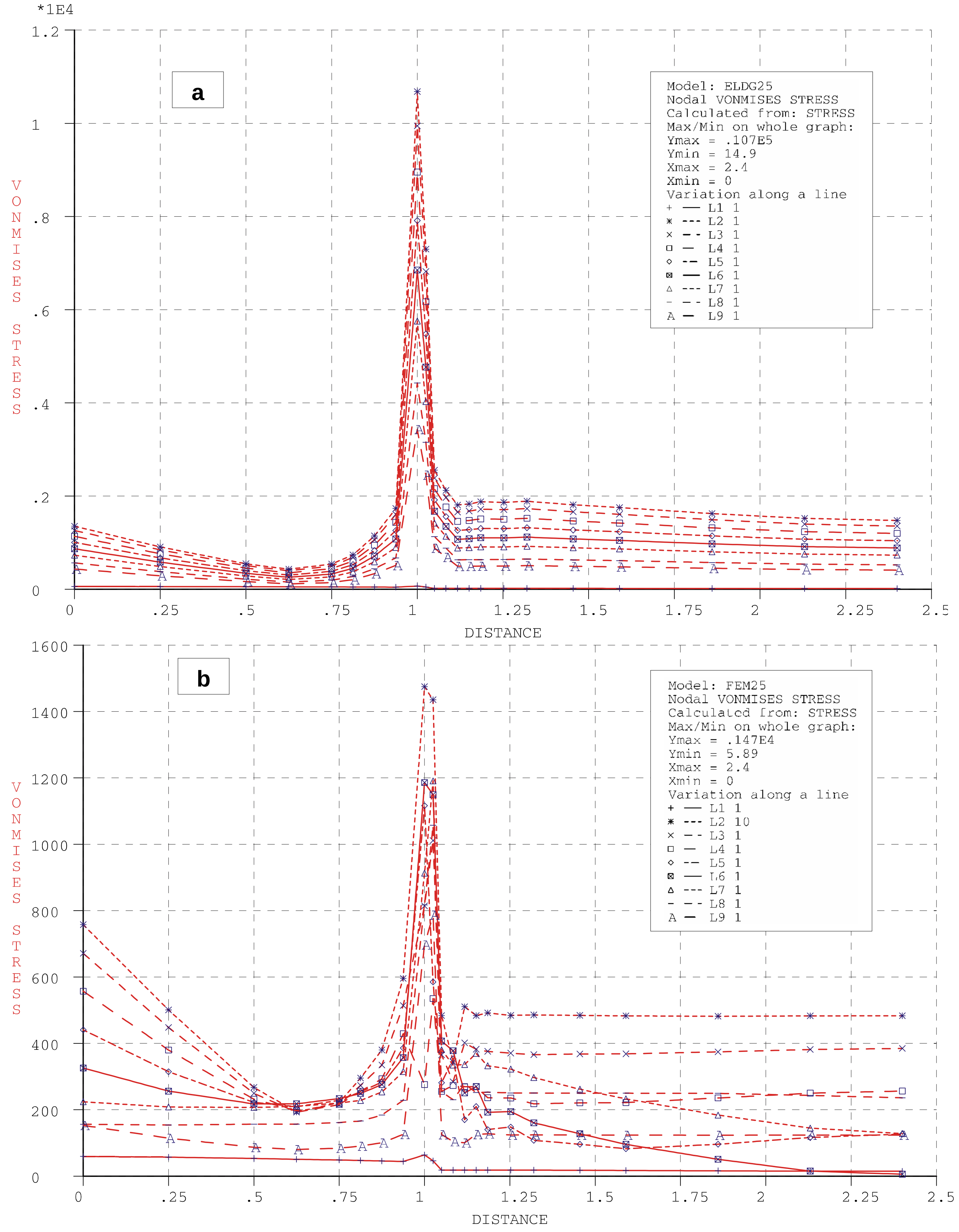

Fig. 6.2.2-4: Von Mises stresses [MPa] along AB: a) consideration of the elastic materials behaviour only, b) externally defined elastic-plastic material behaviour.

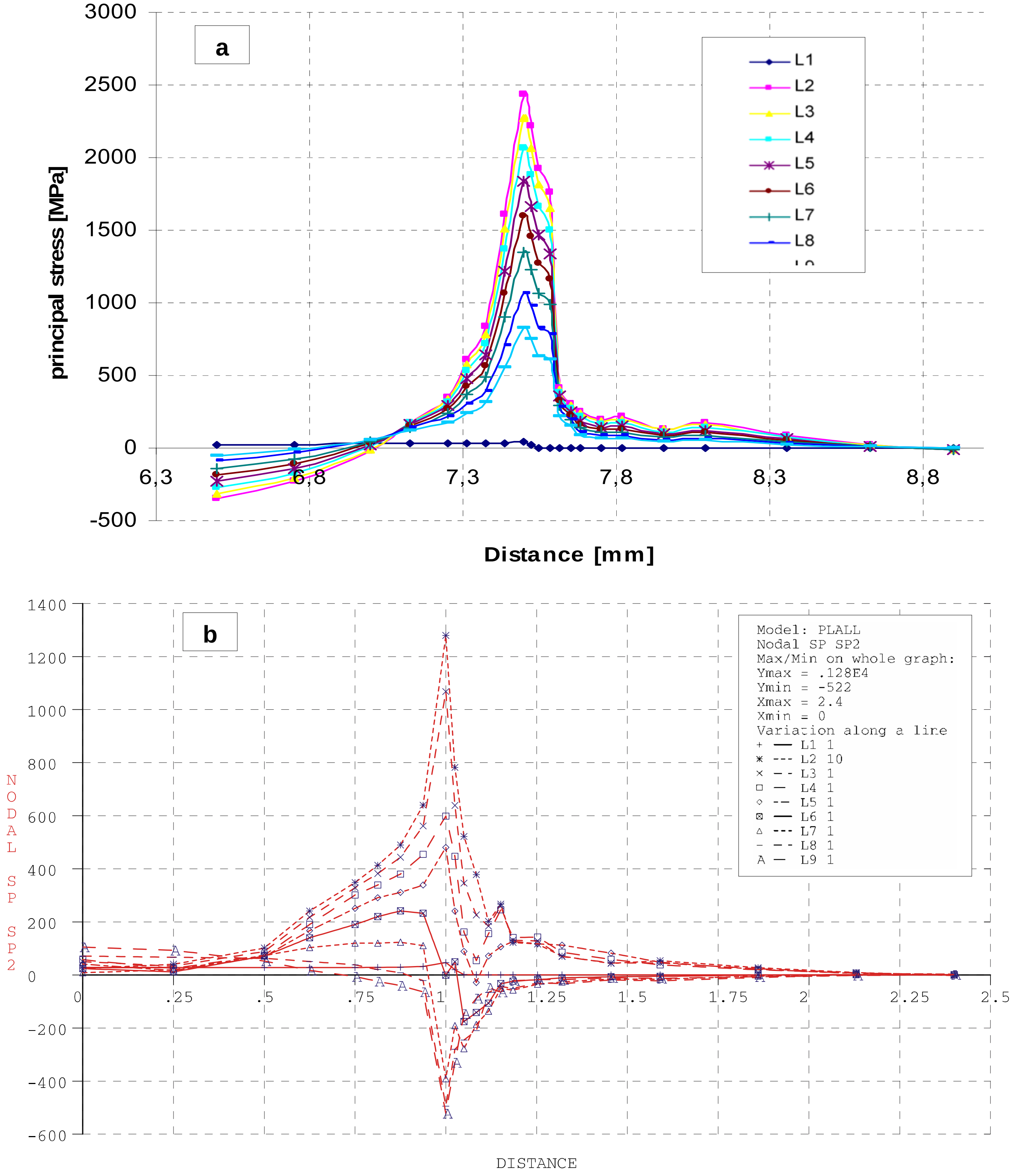

Fig. 6.2.2-5: Principal σII stresses [MPa] along CD: a) consideration of the elastic materials behaviour only, b) externally defined elastic-plastic material behaviour.

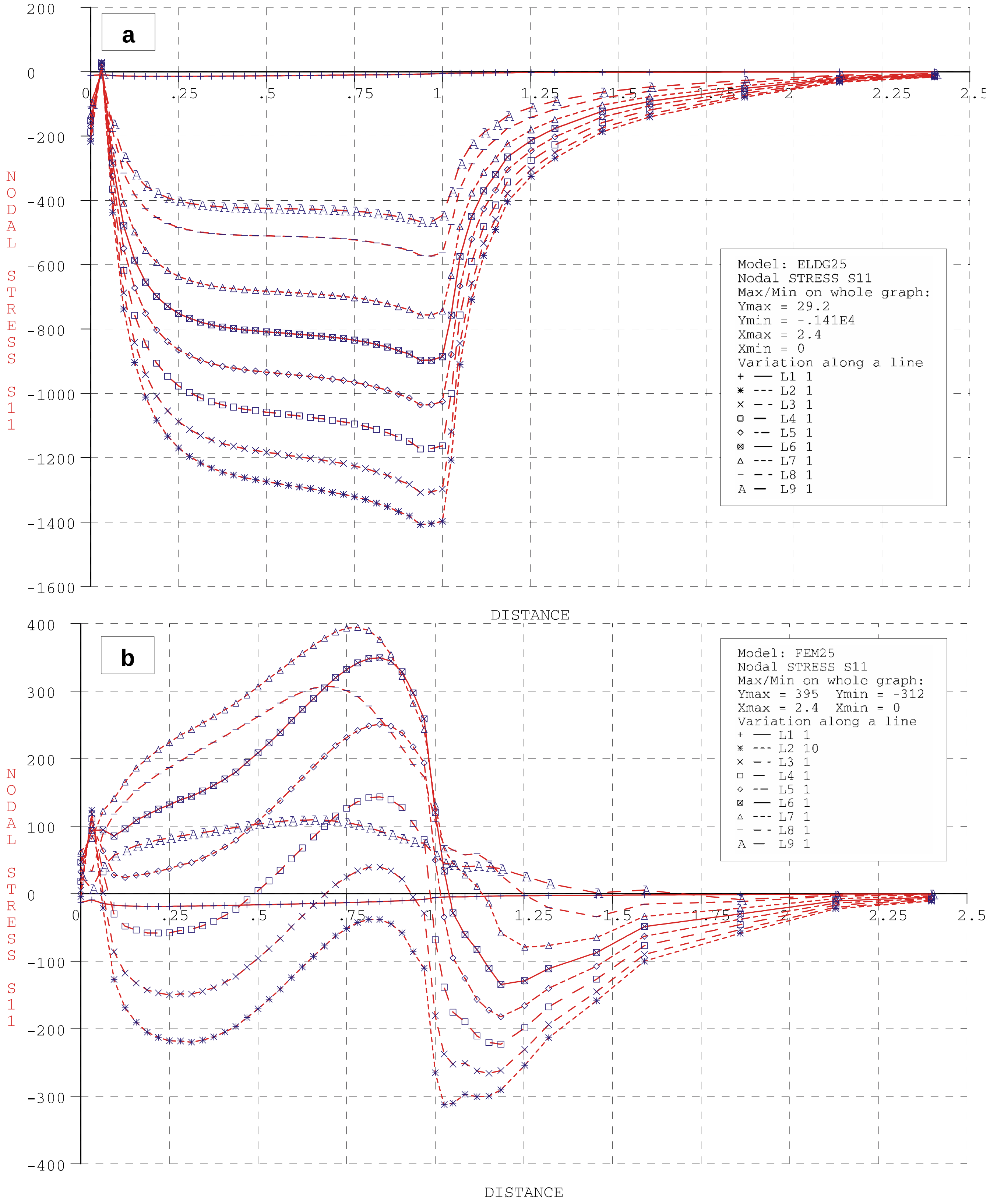

Fig. 6.2.2-6: X-component stresses [MPa] along AB: a) consideration of the elastic materials behaviour only, b) externally defined elastic-plastic material behaviour.

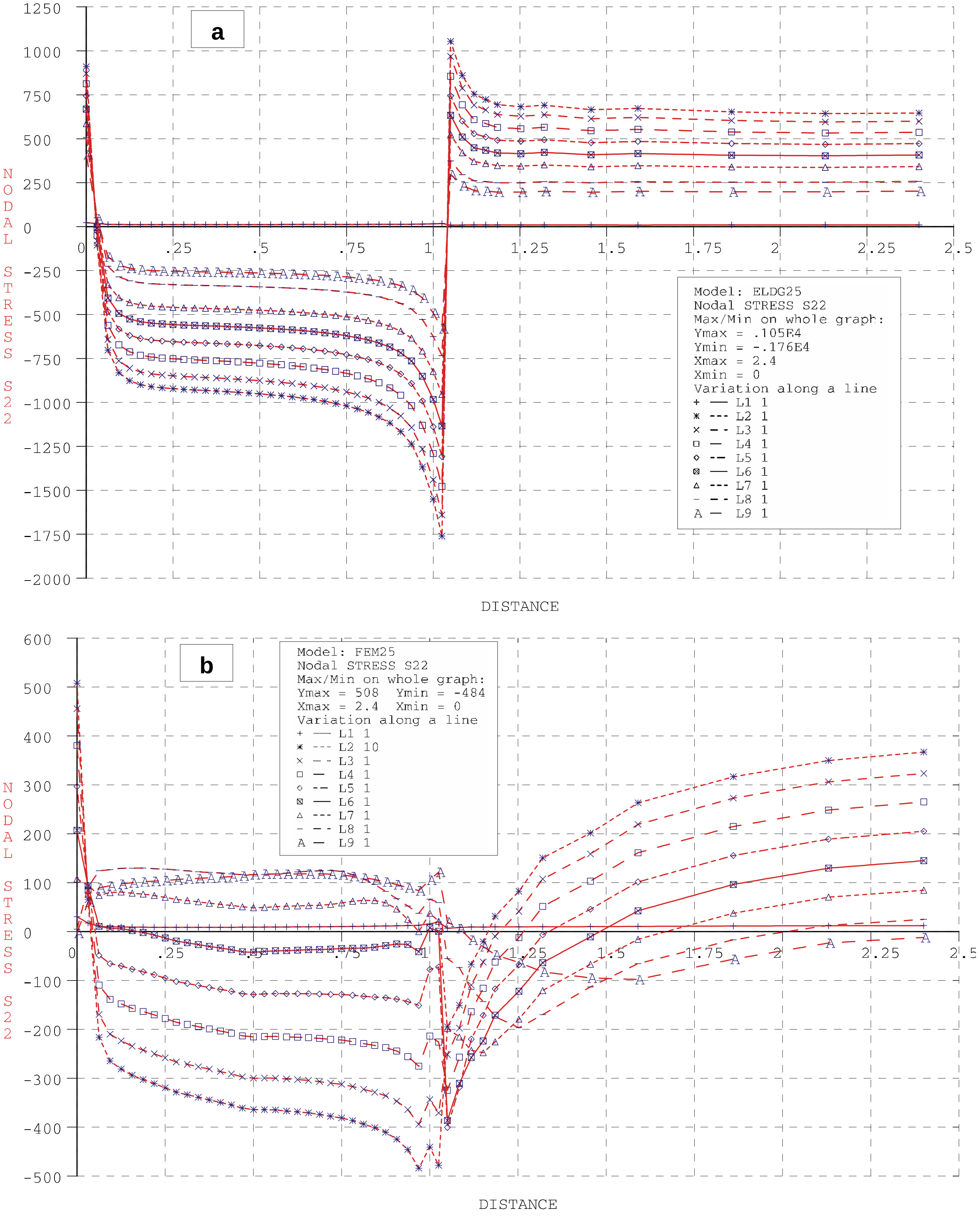

Fig. 6.2.2-7: Y-component stresses [MPa] along AB: a) consideration of the elastic materials behaviour only, b) externally defined elastic-plastic material behaviour.

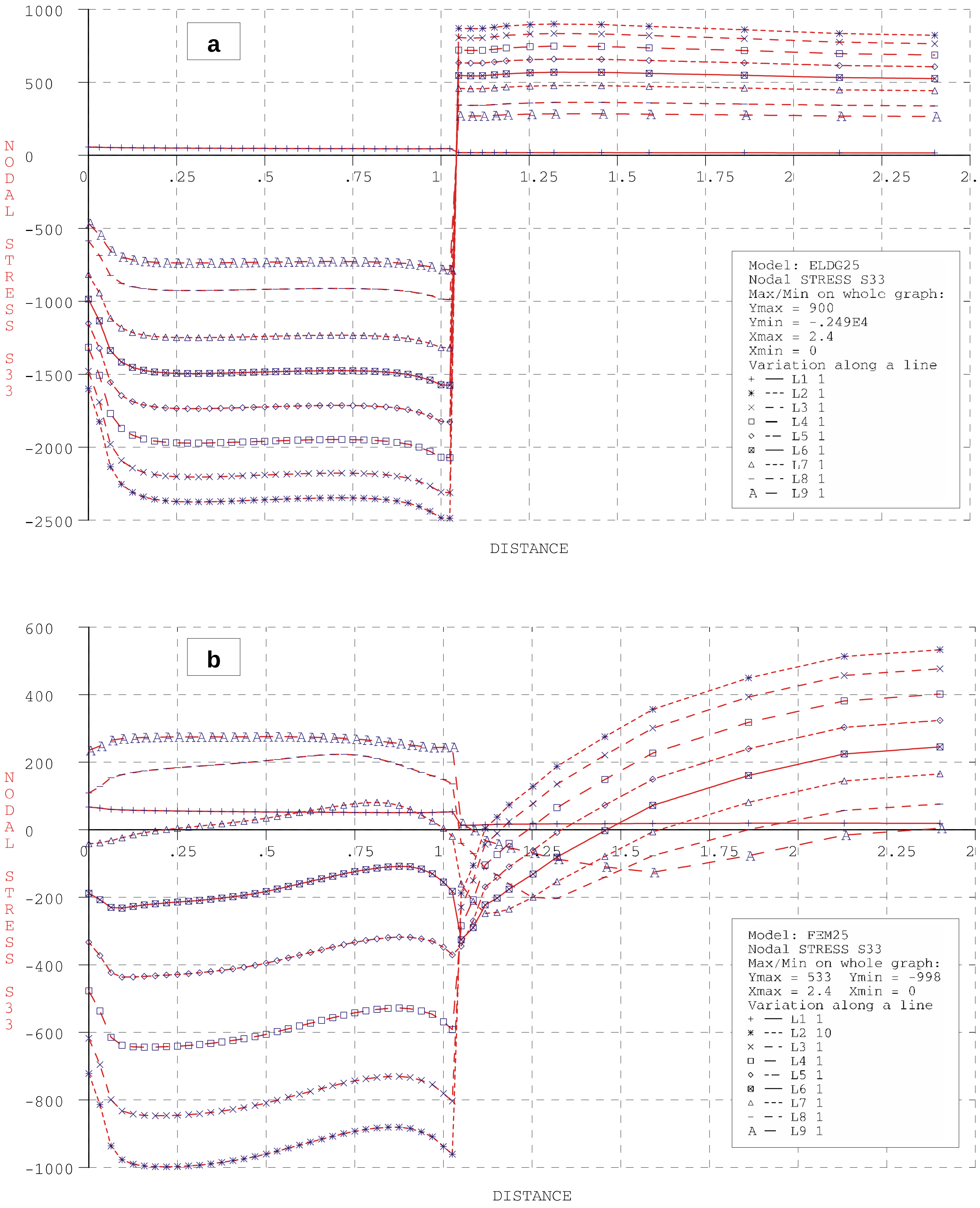

Fig. 6.2.2-8: Z-component stresses [MPa] along AB: a) consideration of the elastic materials behaviour only, b) externally defined elastic-plastic material behaviour.

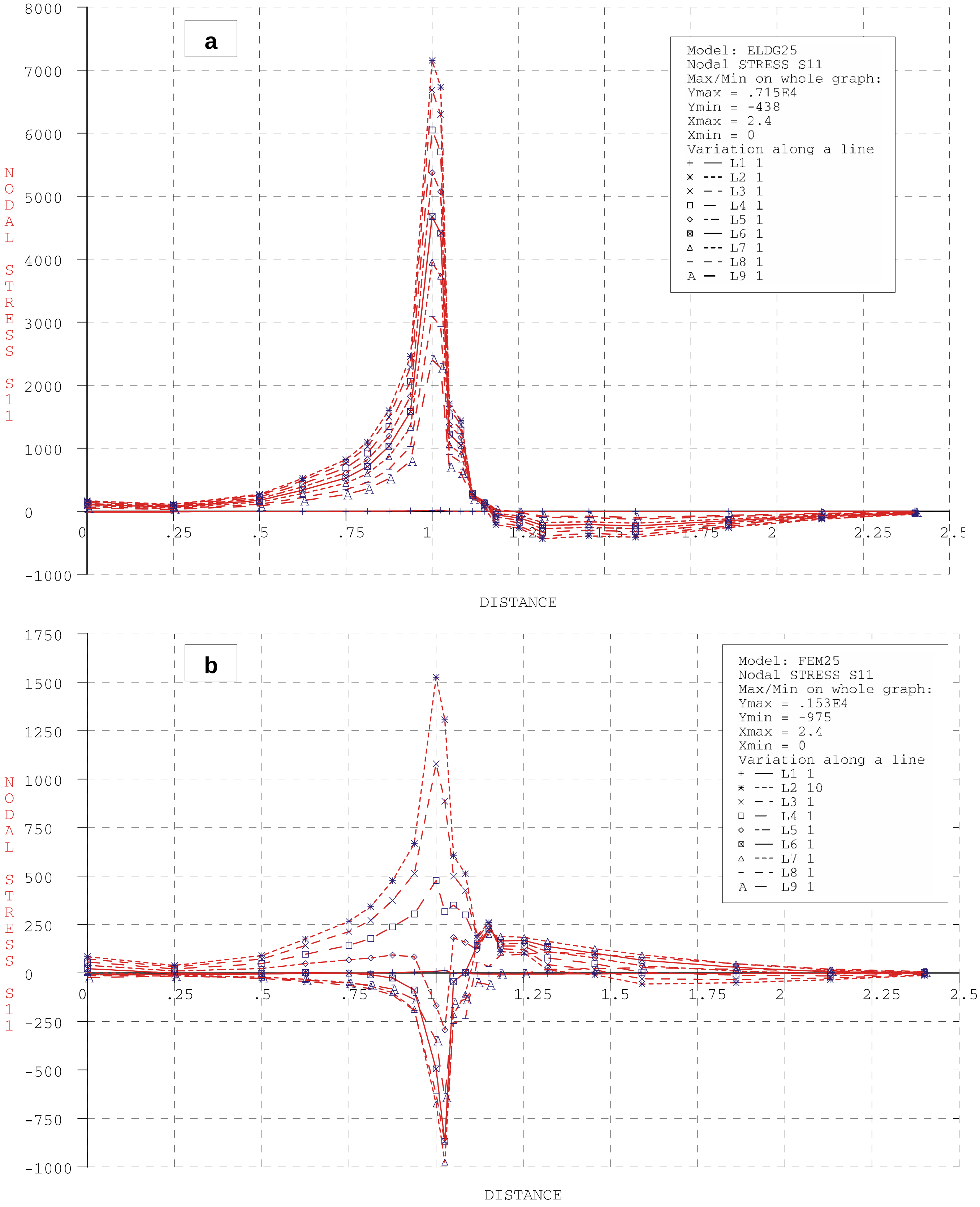

Fig. 6.2.2-9: X-component stresses [MPa] along CD: a) consideration of the elastic materials behaviour only, b) externally defined elastic-plastic material behaviour.

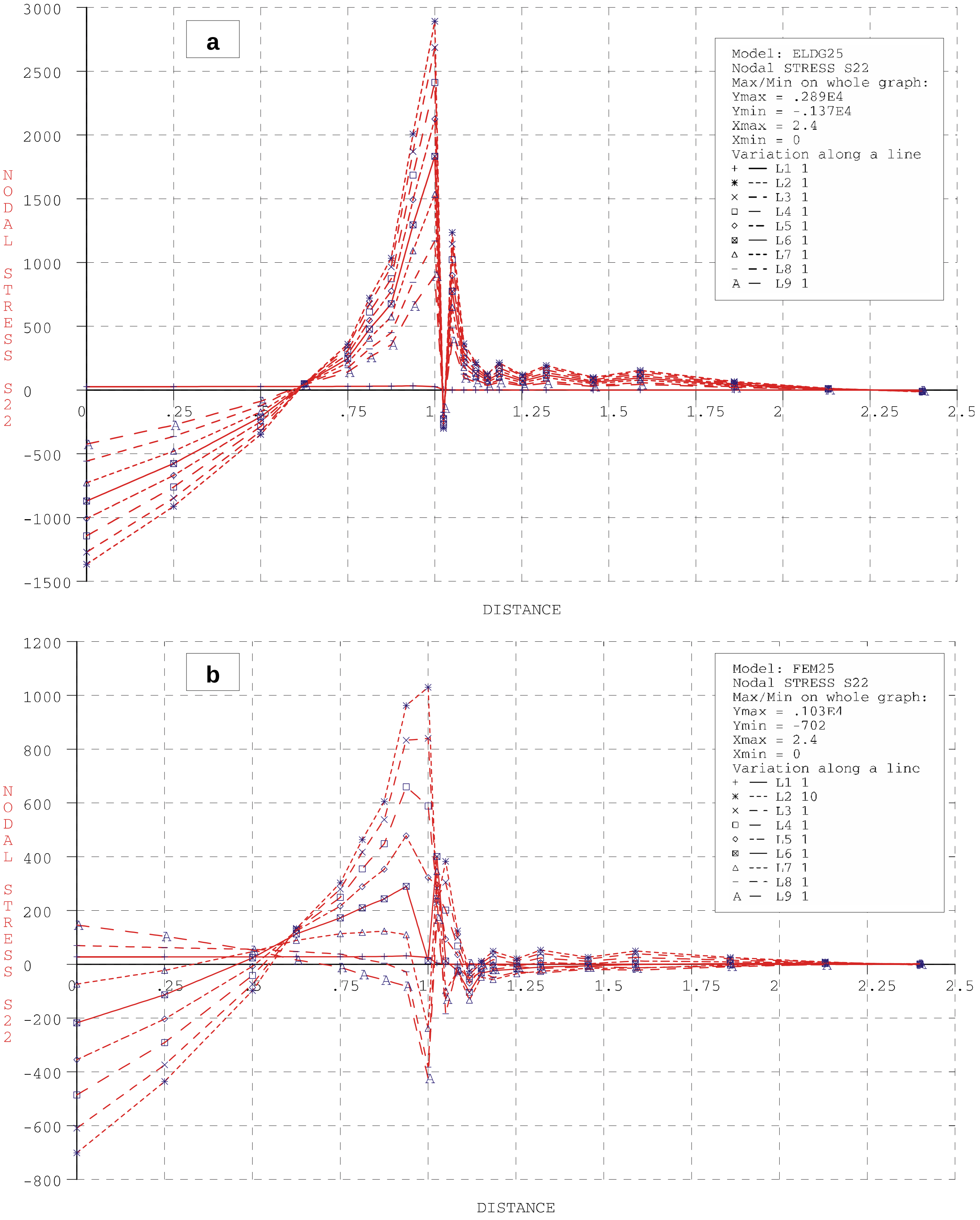

Fig. 6.2.2-10: Y-component stresses [MPa] along CD: a) consideration of the elastic materials behaviour only, b) externally defined elastic-plastic material behaviour.

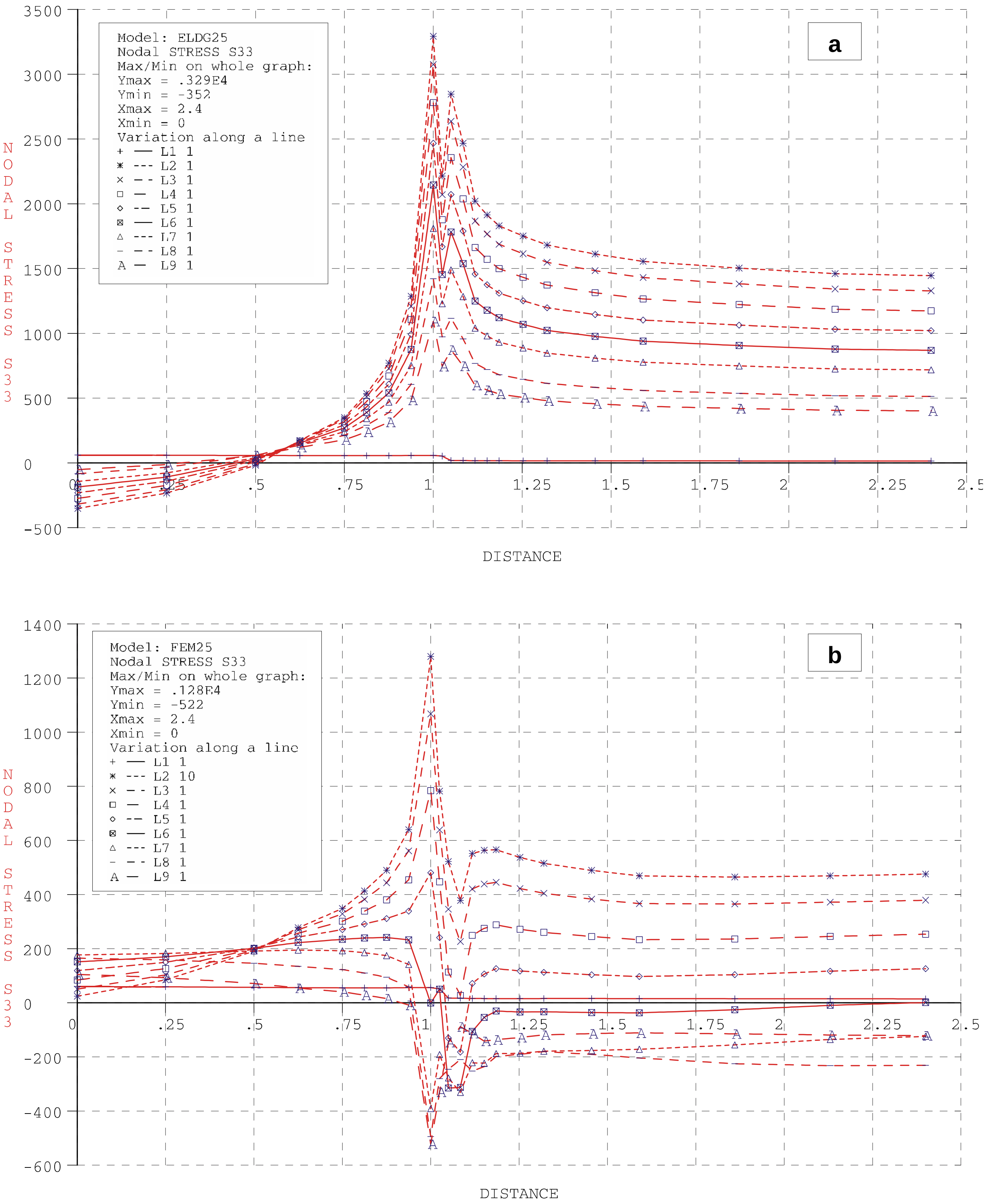

Fig. 6.2.2-11: Z-component stresses [MPa] along CD: a) consideration of the elastic materials behaviour only, b) externally defined elastic-plastic material behaviour.